University of Alberta

COKE AND SULFUR RESISTANT SOLID OXIDE FUEL CELLS:
DEVELOPMENT, TEST AND NOVEL APPLICATIONS

by

NING YAN

A thesis submitted to the Faculty of Graduate Studies and Research
in partial fulfillment of the requirements for the degree of

DOCTOR OF PHILOSOPHY

in

MATERIALS ENGINEERING

DEPARTMENT OF CHEMICAL AND MATERIALS ENGINEERING

©NING YAN
Spring 2014
Edmonton, Alberta

ABSTRACT

Solid oxide fuel cells (SOFC) can be fuelled with external-reformed natural gas or directly with raw natural gas which usually contains significant amount of H_2S to reduce the system complexity. The anode catalyst as well as the current collector employed in those environments must have excellent coke and sulfur resistances in addition to the general requirements. The coke-sulfur tolerant SOFC serving as a reactor could co-generate power and value-added chemical products, which promises to drastically minimize the energy waste and increase the efficiency.

To address the coking issues in fuel cells fed by syngas or pretreated natural gas, Ni-P coated Ni foam is fabricated via electroless plating as the coke resistant current collector. The coated Ni foam with a surface composition of Ni_3P + Ni (P > 6.5 wt%) exhibits excellent coking resistance in syngas at 750 ^oC and essentially identical current collecting capability with Au mesh during fuel cells test. The Ni-S_x catalyst obtained through *in-situ* H_2S passivation shows superior balance between high activity and good carbon resistance during 200 h test in dry syngas.

To deal with the coking and sulfur deactivation issue in SOFC fuelled by sour natural gas with H_2S concentration up to 0.5%, Pd-CeO_2/$La_{0.3}Sr_{0.7}O_{3-\delta}$ composite anode catalyst has been studied and is applied to the fuel cells via infiltration method. Maximum power densities of 642 mW cm^{-2} and 274 mW cm^{-2} have been achieved in H_2 and in 0.5% H_2S + CH_4 at 850 ^oC, respectively. Pd particles in the

catalyst are proven to be thermodynamically stable, whereas CeO_2 promotes their thermal stability on the electrolyte matrix.

In the application of coke/sulfur tolerant fuel cells for the co-generation of electricity and CO from syngas, the developed proton-conduction SOFC is able to reach a maximum power density of 812 mW cm^{-2} at 750 ^{o}C and up to 23.4 % H_2 is removed in the stream without oxidizing CO. Novel H_2 electrocatalytic selective oxidation in syngas using O^{-2}-conducting SOFC is also studied. The Ni-S anode catalyst shows up to 92% H_2 selectivity through selective surface diffusion mechanism in 10% H_2 + CO.

ACKNOWLEDGEMENTS

CONTENTS

List of Tables

List of Figures

List of Abbreviations

AFC	Alkaline fuel cell
BZCY	Ba $Zr_{0.1}Ce_{0.7}Y_{0.2}O_{3-\delta}$
BPC	$Ba_{0.5}Pr_{0.5}CoO_{3-\delta}$ or $BaPrCo_2O_{6-\delta}$
BV	Butler-Volmer
CCR	Conventional catalytic reaction
CTE	Coefficient of thermal expansion
ECR	Electrocatalytic reaction
EDS	Energy dispersive X-ray spectrometer
EIA	Energy Information Administration
EIS	Electrochemical impedance spectroscopy
FCC	Face-centered cubic
FT	Fischer-Tropsch
GC	Gas chromatography
HSO	H_2 selective oxidation
IR	Infrared
I-V	Current-Voltage (polarization) curve
LSF	$La_{0.8}Sr_{0.2}FeO_{3-\delta}$
LSM	$La_{0.8}Sr_{0.2}MnO_{3-\delta}$
LST	$La_{0.3}Sr_{0.7}TiO_{3+\delta}$
MCFC	Molten carbonate fuel cell
MEA	Membrane electrode assembly
MPD	Maximum power density
MS	mass spectrometer
OC-SOFC	Oxygen ion conducting solid oxide fuel cell
OCV	Open circuit voltage
PAFC	Phosphoric acid fuel cell
PC-SOFC	Proton-conducting solid oxide fuel cell

PEMFC	Pronto exchange membrane fuel cell
SDA	Surface diffusion area
SEM	Scanning electron microscope
SOEC	Solid oxide electrolyzer cell
SOFC	Solid oxide fuel cell
TPB	Triple-phase boundary
WGS	Water gas shift reaction
XPS	X-ray photoelectron spectroscopy
XRD	X-ray diffraction
YSZ	Yttria stabilized zirconia

Chapter 1 Introduction

1.1 Fossil Fuels and Electricity

1.1.1 Electricity generation from fossil fuels

Energy sources are important in advancing industrial development and technology innovations. For thousands of years, heat from the combustion of natural organic compounds including woods and fossil fuels was the only source of energy for human beings. Since the massive utilization of electrical power in 20th century, electricity not only enlightened the world, but also catalyzed numerous inventions, most of which we have already taken for granted such as computers and cellphones. Without electricity, our modern society would not be what it is today and our dependence upon various energy sources has never been more evident.

At the present time, besides a couple of other resources for electricity generations including solar energy, nuclear energy and hydropower, the combustion of fossil fuels still plays an indispensable role in the production of electrical power worldwide [1]. In 2009, the amounts of electricity generated from natural gas, coal and oil accounted for 21%, 42% and 5% of the total, respectively, whereas non-fossil fuels contributed only 32 % to the total power produced

(Fig.1-1). It should be emphasized that between 1971 and 2010, world electricity generation rose at an average annual rate of 3.7%. From 2010 to 2030, it was estimated that the world electricity generation would increase at an average annual rate of 2.5%. To meet the increasing demand for energy, diversification of how the electricity is generated becomes necessary.
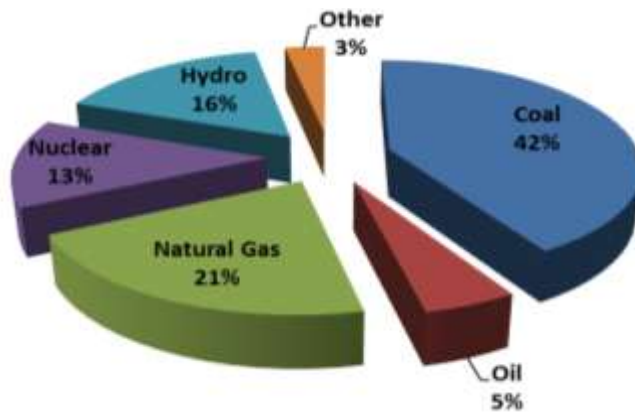
Figure1-1 World electricity generation from different resources [1].
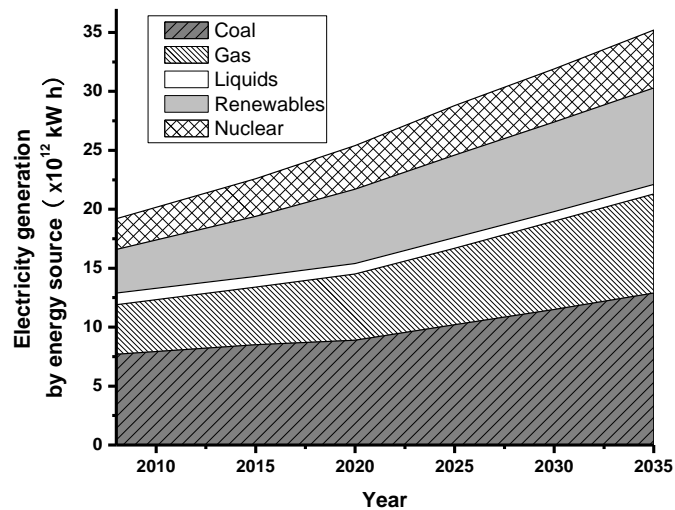
Figure 1-2 Outlook of electricity generation by energy sources [2].

2

Nuclear reactor appears to be a good candidate for future power source, but its high risk of operation, possible catastrophic consequences and questionable acceptance by local communities may limit its development of large scale. The 2011 Fukushima nuclear power plant accident triggered by tsunami in Japan was one of bad examples. Thus, nuclear reactor's larger contribution to the electricity generation is not expected after 2020 [2]. Other promising alternatives are renewable energies, such as solar, wind and geothermal energies, biofuels and bio-wastes since they are re-generable and more environmentally friendly. However, these energy resources are of limited importance, e.g., in 2009, they accounted for only 3.0% of total world electricity production. It is anticipated that starting from around 2020, the trend of using renewable energy for generating electricity will slow down and its share will only account for less than 9 % by 2030.

Fossil fuels for power generation, on the other hand, still face little challenge. Since 2010, there has been a continuous increase in fossil fuel consumption for electricity and it is expected that by 2030, more than 60 % of the power will be from fossil fuel. Among all types of fossil fuels, natural gas and coal are the two most important ones for future electricity generation since petroleum, another major type of fossil fuel, has already been heavily demanded by vehicles consumption and petrochemical industry [2]. According to the statistics [3], the proven coal reserves should last another 155 years while this number is 65 for natural gas. The petroleum reserves, however, will only last about 40 years.

Meanwhile, massive production of natural gas from shale has been industrialized recently; this technology has expanded the extractable reserves of natural gas considerably [4]. Under this situation, natural gas and coal are considered as a transitional energy source while moving from fossil fuel based economic system to the future system powered by renewable energy [5].

As there is a strong positive correlation between electricity consumption and economic development/scientific progress, a new round of energy crisis can break out in the near future. At the same time, the rapid growth of world population escalates the consumption of energy, which will lead to a worldwide surge in energy demand [6]. While this historical trend may be inevitable, the more efficient utilization of currently available fuels becomes equally important as the ever intensive search for more alternative energy resources.

1.1.2 Efficient usage of fossil fuels in power plant

Using natural gas as fuels for power plant is one way to increase the thermal efficiency and reduce environmental impact. In the 1970s and 1980s, the choices for most electric generators were largely based on coal or nuclear [7]. However, due to environmental considerations and technological progress, natural gas has become the fuel of choice for new power plants built since 1990s, especially in North America according to the Energy Information Administration (EIA) [2]. Natural gas exists in gaseous state, this allows natural gas-fired power plant to use combined-cycle technology which offers significantly higher thermal efficiency.

Figure 1-3 shows the operation principle of this method. This electricity generating facility includes both gas turbine and steam turbine. The gas turbine operates at a higher temperature, using the hot gases released from burning natural gas. Then it will drive the generator to produce electricity. The waste heat from the gas-turbine process is directed towards generating steam and then reused by steam turbine to generate extra electricity. Therefore, the combined steam and gas turbine can increase the total thermal efficiency up to 50 to 60 percent [8]. Meanwhile, natural gas fuelled power plants play an increasingly important role in lessening environmental damage. Usually, natural gas burns more completely than other fossil fuels and the emission of CO_2, NO_x, SO_2 and particulates from the combustion is considerably lower than that from burning coal or petroleum for an equivalent amount of heat [9].

In those counties with limited natural gas reserves, such as China or India, their booming economies are primarily dependent upon coal based energy and coal gasification becomes an excellent technical route for the efficient usage of coal in power plant. Rather than burning coal directly, gasification decomposes coal to generate syngas, a combination of CO and H_2, and other basic chemical constituents which will be further utilized in multiple ways. The benefit of gasification is that the solid coal is converted into gaseous syngas, making it possible to use combined-cycle technology for electricity generation. Its basic principles are the same as those used in natural gas power plant as discussed in Fig. 1-3. In conventional coal fired power plant, it is common that only one third

of the energy value of coal is converted into electricity [10]. In contrast, syngas fueled plant can potentially increase the efficiency to more than 50 %.

Using gasified coal is also beneficial to the environment. For example, sulfur in coal can be converted into hydrogen sulfide which can be removed by subsequent chemical processes. The mercury in coal is very difficult to be completely removed, particularly the elemental mercury vapor which can not be effectively captured in typical air-pollution control devices [11]. However, in controlled gasification process, various absorbents can be applied to achieve an effective mercury adsorption. It should be noted that coal-to-syngas process normally generates a large amount of solid wastes which should be dealt with seriously [12].
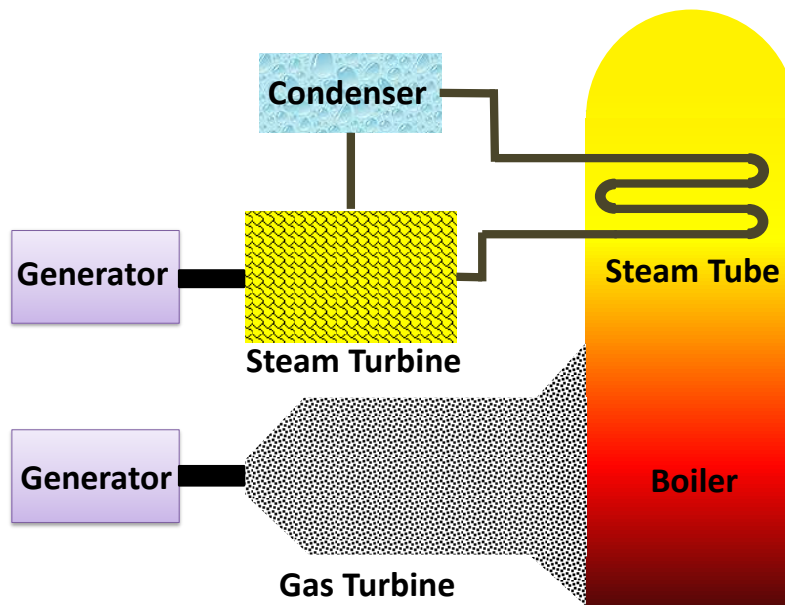
Figure 1-3 Operation principles of combined-cycle technology.

1.1.3 Syngas and its applications

Syngas has been produced commercially for more than 100 years [13]. Nowadays, coal, natural gas or biomass can be used for the gasification reaction [14]. In addition to the application in power plant, gasification is a very efficient way of fossil fuel utilization, offering one of the most versatile and clean ways to convert hydrocarbons into hydrogen and other valuable energy products [15]. The reactions below describe the origin of syngas from natural gas and coal, respectively:

$$CH_4 + H_2O \rightarrow CO + 3H_2 \tag{1-1}$$

$$C + H_2O \rightarrow CO + H_2 \tag{1-2}$$

The major commercial applications of syngas can be summarized into five categories [16]:

(1) Production of hydrogen H_2. Syngas is the major source of commercially manufactured H_2. When syngas is treated with excess water in the presence of catalysts, the CO can react with steam to yield more H_2 via the water-gas shift (WGS) reaction shown by the reaction (1-3)

$$CO + H_2O \rightarrow CO_2 + H_2 \tag{1-3}$$

(2) Production of methanol. Almost all the methanol worldwide is synthesized from syngas containing certain amount of CO_2. Two catalytic reactions are responsible for its synthesis

$$CO + 2H_2 \rightarrow CH_3OH \tag{1-4}$$

$$CO + 3H_2 \rightarrow CH_3OH + H_2O \qquad\qquad\qquad (1\text{-}5)$$

(3) Fischer-Tropsch reactions. The Fischer-Tropsch (FT) process was discovered by Fischer and Tropsch in 1923 [17], which firstly enabled the conversion of syngas to liquid fuels on a large scale. The FT reaction yields a wide spectrum of hydrocarbons and oxygenated products which can be utilized as gasoline, diesel fuel or feedstock source for chemical productions. Three major reactions are listed below:

$$\textit{Paraffins} \quad (2n+1)H_2 + nCO \rightarrow C_nH_{2n+2} + nH_2O \qquad\qquad (1\text{-}6)$$

$$\textit{Olefins} \quad 2nH_2 + nCO \rightarrow C_nH_{2n} + nH_2O \qquad\qquad\qquad (1\text{-}7)$$

$$\textit{Alcohols} \quad (2n+1)H_2 + nCO \rightarrow C_nH_{2n+1}OH + (n\text{-}1)H_2O \qquad (1\text{-}8)$$
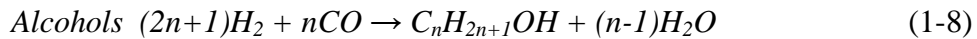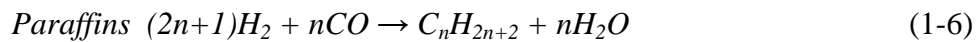
(4) Other chemicals synthesis. It involves miscellaneous reactions between syngas and other chemicals. An example of these reactions is hydroformylation (oxo) reaction consisting of the interaction of olefin and syngas to yield aldehydes or alcohols with one more carbon on the original carbon chain.

(5) Heat and power generations

1.2 Fuel Cells Technology and Alternative Applications

Although combined-cycle technology increased the thermal efficiency significantly in the power plant, scientists and researchers are continuously trying

to figure out new technical routes which would make the most efficient uses of the limited fossil fuels. This part will introduce a new and promising way for efficiency enhancement using solid oxide fuel cells (SOFC). In addition, the general alternative applications of SOFC technology for energy storage and chemicals production will also be reviewed.

1.2.1 Power generation using fuel cells

The efficiency of conventional thermal engine is limited by the basic laws of thermodynamics. The Carnot's cycle generalizes the theoretical maximum efficiency η which is defined as below,

$$\eta = 1 - \frac{T_C}{T_H} \tag{1-9}$$

where

T_C is the absolute temperature of the cold reservoir, and

T_H is the absolute temperature of the hot reservoir.

A fuel cell is an energy conversion device that generates electricity directly from a gaseous fuel via electrochemical catalytic reaction. It has drawn increasing attentions recently as one of the most promising power sources. Usually, a fuel cell is consisted of three major components: a cathode, an anode and an electrolyte; no mechanical parts are included in the system. Therefore, its efficiency is not governed by equation 1-9 and promises much higher theoretical

efficiency. In general, there are five types of fuel cells summarized below in Table 1-1.

Table 1-1. Summary of major types of fuel cells [18]

	Polymer Electrolyte (PEMFC)	Alkaline (AFC)	Phosphoric Acid (PAFC)	Molten Carbonate (MCFC)	SOFC
Electrolyte	Proton Exchange Membrane	Hydroxide	Phosphoric Acid	Molten Carbonate	Solid Ceramics
Operating Temperature	~ 350 K	330 K~ 600 K	~ 480 K	873 K ~ 1173 K	873 K ~ 1173 K
Compatible Fuels	H_2	H_2	H_2	H_2 and Hydrocarbons	H_2 and Hydrocarbons
Noble Metals Requirement	Yes	Yes	Yes	No	No
Sensitivity to Poisons	High	High	High	Depending on Catalysts	Depending on Catalysts

PEMFC is the predominant type of low temperature fuel cells which need noble metals to catalyze the electrochemical reactions. On the other hand, since the electrolyte is a protonic conductor, only H_2 can be fed as the fuel and the anode catalyst is very sensitive to CO poisoning even at ppm level [19]. Similar disadvantages have also been found in AFC and PAFC. Although MCFC can be fed by hydrocarbons, the molten carbonate electrolyte is highly corrosive and the cost of fuel cell manufacturing is high [18].

1.2.2 SOFC
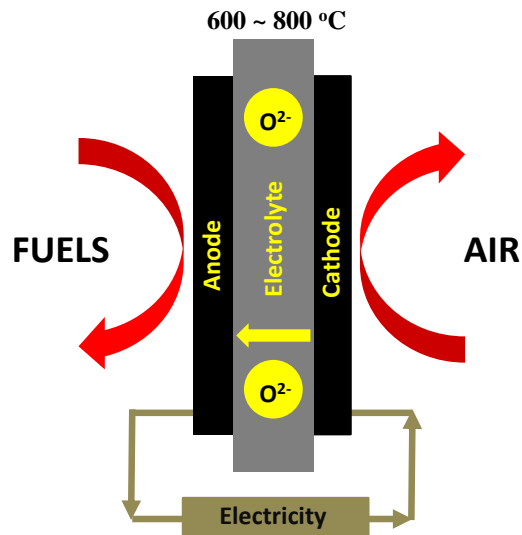
Figure1-4 A schematic of SOFC operation principles.

Fig.1-4 illustrates the working principles of solid oxide fuel cell. SOFC has a ceramic electrolyte that is a non-porous metal oxide, usually Y_2O_3-stablilized

ZrO$_2$ (YSZ). Due to different oxygen partial pressure at each site of the electrolyte, the oxygen ions in the dense ceramic will be driven to move from cathode to anode and react with the readily activated fuels at the anode site. Since the electrolyte is primarily an ionic conductor with negligible electronic conductivity, the electrons released will move through the external circuit, and power is thus generated. Conventionally, a typical anode material is Ni-YSZ composite whereas the cathode material is a perovskite oxide such as Sr doped LaMnO$_3$ [20, 21].

Compared with low temperature fuel cells, SOFC has various promising advantages, e.g., greater fuel diversity, higher thermal efficiency and relatively lower manufacturing cost. Hence, it has been intensively studied over the last two decades and several generations of SOFC have been developed [20, 21]. Like any new product or invention, the commercialization of SOFC is the key to symbolize its ultimate success. A number of corporations have been focusing on this which include but not limited to Bloom Energy, Versa Powers, and Ceramic Fuel Cells Limited. The power output of the developed SOFC stack can now reach as high as 200 kW with satisfactory durability [22]. Nevertheless, if the high price of commercial SOFC is not subsidized by the government, its marketing would be facing much tougher challenge [23].

1.2.3 Alternative applications of SOFC technology

In addition to being applied as the power generator, SOFC technology can also be used for chemical production and reversibly for energy storage. These

12

alternative applications provide new routes or solutions for particular industrial processes and great efforts have been devoted to their development recently.
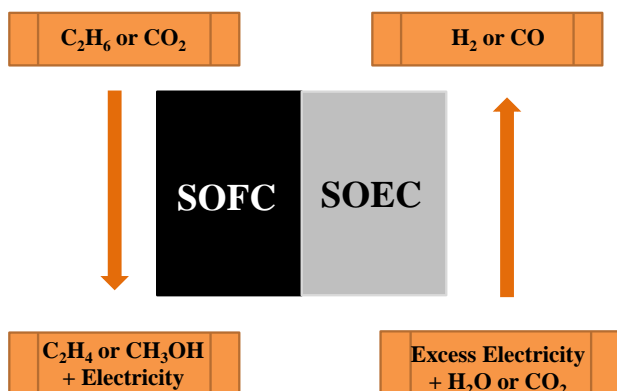
Figure 1-5 principles of SOFC alternative applications.

In its application for chemical production, SOFC is able to cogenerate electricity and value-added chemicals without any or with less power input. For instance, in the proton-conducting SOFC, ethane dehydrogenation and H_2 electro-oxidation can proceed simultaneously, resulting in the co-production of both ethylene and electricity [24]. Another example is CO_2 hydrogenation, in which H_2 can come from the anode and reduce CO_2 into CO and CH_3OH at the cathode side. The research has showed that the reaction rate in SOFC is apparently faster than that of a conventional reactor [25].

Besides electricity generation and chemicals production, SOFC can also be utilized reversibly as a solid oxide electrolyzer cell (SOEC) for energy storage. In

this process, electricity is used to electrolyze water and/or carbon dioxide to produce fuels which will then be consumed during peak hours. The required electricity can stem from a renewable source, such as wind or solar energy, or excess grid electricity during off-peak hours [26]. Another concept in fuel cell energy storage is that the fuel cell could be coupled to an external charge storing device such as a battery. Recently, new progresses have been published that the fuel cell itself can act as a battery. The energy stored in the anode material will be released once the fuel supply is cut off, and the fuel cell can still work for a reasonable period of time [27].

1.3 Challenges

The current large-scale (MW-level) SOFC stacks are only able to use high purity methane, syngas or H_2 as the fuels with trace amount of H_2S which is a major impurity in the raw feedstock [28]. Upon exposure of higher concentration of H_2S, the commonly used anode catalysts such as Ni will be irreversibly poisoned and SOFC will suffer severe performance degradation. Therefore, extensive efforts have been devoted to understanding the interaction between H_2S ($H_2S/H_2 < 100$ ppm) and Ni [29-33]. After H_2S was introduced to an operating SOFC, the first sharp current drop was ascribed to the readily adsorbed S which blocked active sites on Ni [32, 33]. Unfortunately, no consensus has been achieved in explaining the second stage long-term continuous cell degradation without reaching saturation in Ni based SOFC. Some researchers believed that the

Ni surface reconstruction played an important role whereas others attributed the phenomena to the impurities in sealants [30]. It also appears to be controversial that in some experiments, the second stage degradation reached saturation after hundreds of hours of test in H_2S containing H_2 [34, 35].

Novel sulfur resistant anode catalysts have also been intensively investigated. Among the various proposed alternative materials, perovskite structure oxides have been well-studied. Doped $SrTiO_3$, doped $LaVO_3$ and doped $LaCrO_3$ are three typical examples of this category [36-38]. Furthermore, ceria, tungsten bronze and pyrochlore structure oxide were also examined as anode candidates [39-41]. However, the performance of pure oxide anode was not comparable with Ni in terms of catalytic activity.

Coking is another critical problem associated with utilizing hydrocarbon fuels in SOFC. The carbon formed on the surface of Ni tends to grow inward to its crystal lattice and finally destroy the metallic structure integrity. Presently, in order to avoid detrimental coking effect, excess water has to be added into the anode feed, which enables CH_4 external reforming and CO mitigation to H_2 via WGS reactions. The external reforming process not only increases the system complexity, but also decreases SOFC efficiency [20]. Thus, a variety of research projects have been directed towards the development of high temperature carbon tolerance materials employed in SOFC [42]. In addition to the application of functional oxides discussed in the previous paragraph, alloying was another widely used strategy in designing coke-free high performance metallic catalyst.

For example, alloying element Cu can alleviate Ni coking considerably via suppressing the formation of C-C bond on Ni surface [43].

In summary, it is highly desirable to develop novel anode materials that are not deactivated by H_2S-containing hydrocarbon fuels while maintaining satisfactory activity towards their electrochemical oxidations.

1.4 Objectives and Thesis Contents

The significant achievements of the current research will be reviewed in Chapter 2. The methodology applied in this work will be discussed in Chapter 3. This research work will aim to reach two equally important goals. The first one is to investigate novel SOFC materials which meet the target requirements of high temperature S and C resistance. To address the existing challenges, suitable materials will be proposed, tested and optimized as the anode current collector (Chapter 4) and the anode catalyst (Chapters 5 and 8). Based on the different degrees of coking, H_2S poisoning and other conditions, the SOFC service conditions will be analyzed/categorized and the selected materials will be employed in each category. Subsequently, the SOFC performance can be optimized while satisfying the overall requirements.

The second goal is to study the novel alternative applications of SOFC in value-added chemicals production by using the developed catalysts mentioned above. In this section, SOFC will be designed as an electrochemical reactor in which CO can be concentrated from syngas (Chapters 6-8). H_2 in the feedstock

16

will be ionized to pass through the ceramic proton-conducting electrolyte and oxidized by air at the cathode side. In addition, a novel mechanism entitled as H_2 electrocatalytic selective oxidation in syngas will also be proposed. In this work, the electrolyte will be the conventional oxygen ionic conductor; suitable anode catalyst will be developed which preferentially activates H_2 and facilitates the oxidation of readily chemisorbed H atoms by O^{2-}. Fig. 1-6 demonstrates the three major sections of the thesis and the numbers in the brackets indicate the corresponding chapters in which those topics will be addressed.

Thesis Contents

Literature Survey (1-2) and Methodology (3)

Current Collector Development (4)

Anode Catalyst Development (5,8)

SOFC Novel Applications (6-8)

Conclusions, Recommendations and Future Work (9)

Figure 1-6 Major contents of the thesis.

References:

[1] OECD, *OECD Factbook 2011-2012: Economic, Environmental and Social Statistics*, OECD Publishing, 2012.

[2] U. S. Energy Information Administration (EIA), "International Energy Outlook 2009", US Department of Energy, Washington DC, 2009.

[3] http://www.bionomicfuel.com/fossil-fuels-reserves-will-not-last-long/.

[4] www.naturalgas. org/overview/background.asp.

[5] Y. C. Wu, *Energy Quarterly*, 1976, **6**, 1-15.

[6] A. Demirbas, A.S. Demirbas and A. H. Demirbas, *Energy Sources*, 2004, **26**,191-204.

[7] International Energy Agency, "World Energy Outlook 2004", OECD Publishing, 2004.

[8] http://en.wikipedia.org/wiki/Combined_cycle

[9] U. S. Energy Information Administration (EIA), "Natural Gas Issues and Trends 1998", US Department of Energy, Washington DC, 1999.

[10] National Petroleum Council (NPC), "Electric Generation Efficiency: Working Document of the NPC Global Oil & Gas Study", Highbeam Research. Retrieved 18 July 2007.

[11] S. Wu, M. A. Uddin, E. Sasaoka, *Fuel*, 2006, **85**, 213-218.

[12] S. Bargigli, M. Raugei, S. Ulgiati, *Energy*, 2004, **29**, 2145-2159.

[13] L. K. Rath, J. R. Longanbach, *Energy Sources*, 1991, **13**, 443-459.

[14] https://en.wikipedia.org/wiki/Syngas.

[15] http://fossil.energy.gov/programs/powersystems/gasification/

[16] I. Wender, *Fuel Process. Technol.*, 1996, **48**, 187-297.

[17] BASF, 1923. US Patents 1,558,559 and 1,569,775.

[18] G. Hoogers, "Fuel Cell Technology Handbook", CRC Press LLC, Boca Raton, FL, 2002.

[19] A. Arpornwichanop, Y. Patcharavorachot and S. Assabumrungrat, *Chem. Eng. Sci.*, 2010, **65**, 581-589.

[20] S. C. Singhal, K. Kendall, "High Temperature Solid Oxide Fuel Cells: Fundamentals, Design, and Applications", Elsevier, 2003.

[21] A. Atkinson, S. Barnett, R. J. Gorte, J. T. S. Irvine, A. J. Mcevoy, M. Mogensen, S. C. Singhal and J. Vohs, *Nat. Mater.*, 2004, **3**, 17-27.

[22] http://www.bloomenergy.com/fuel-cell/energy-server/.

[23] http://www.forbes.com/sites/energysource/2010/02/24/the-economics-of-bloom-energys-breakthrough-fuel-cell/.

[24] X. Z. Fu, J. Y. Lin, S. H. Xu, J. L. Luo, K. T. Chuang, A. R. Sanger and A. Krzywicki, *Phys. Chem. Chem. Phys.*, 2011, **13**, 19615-19623.

[25] G. Karagiannakis, S. Zisekas and M. Stoukides, *Solid State Ionics*, 2003, **162**, 313-318.

[26] S. H. Jensen, H. Larsen, Peter, M. Mogensen, *Int. J. Hydrogen Energy*, 2007, **32**, 3253-3257.

[27] Q. Van Overmeere, K. Kerman and S. Ramanathan, *Nano Letters*, 2012, **12**, 3756-3760.

[28] A. Casanova, *J. Power Sources*, 1998, **71**, 65-70.

[29] L. Yang, Z. Cheng, M. L. Liu, W. Lane, *Energy Environ. Sci.*, 2010, **3**, 1804-1809.

[30] D. W. Dees, U. Balachandran, S. E. Dorris, J. J. Heiberger, C. C. McPheeters, and J. J. Picciolo, in Proceedings of the First International Symposium on Solid Oxide Fuel Cells, S. C. Singhal, Editor, PV 89-11, p. 317, The Electrochemical Society Proceedings Series, Pennington, NJ (1989).

[31] Z. Cheng, J. H. Wang, Y. M. Choi, L. Yang, M. C. Lin and M. L. Liu, *Energy Environ. Sci.*, 2011, **4**, 4380-4409.

[32] Y. Matsuzaki and I. Yasuda, *Solid State Ionics*, 2000, 132, 261-269.

[33] K. Sasaki, K. Susuki, A. Iyoshi, M. Uchimura, N. Imamura, H. Kusaba, Y. Teraoka, H. Fuchino, K. Tsujimoto, Y. Uchidaand N. Jingo, *J. Electrochem. Soc.*, 2006, 153, A2023-A2029.

[34] W. Feduska and A. O. Isenberg, *J. Power Sources*, 1983, **10**, 89-102.

[35] E. Batawi, U. Weissen, A. Schuler, M. Keller and C. Voisard, *ECS Trans.*, 2001, **2001-16**, 140-147.

[36] S. W. Tao, J. T. S. Irvine, *Nat. Mater.*, 2003, **2**, 320-323.

[37] D. P. Fagg, V. V. Kharton, A. V. Kovalevsky, A. P. Viskup, E. N. Naumovich, J. R. Frade, *J. Eur. Ceram. Soc.*, 2001, **21**, 1831-1835.

[38] Z. Cheng, S. W. Zha, L. Aguilar, D. Wang, J. Winnick, M. L. Liu, *Electrochem. Solid State Lett.*, 2006, **9**, A31-A33.

[39] T. Hibino, A. Hashimoto, M. Yano, M. Suzuki, M. Sano, *Electrochim. Acta*

2003, **48**, 2531-2537.

[40] P. R. Slater, J. T. S. Irvine, *Solid State Ionics*, 1999, **124 (1–2)**, 61-72.

[41] B. J.Wuensch, K. W. Eberman, C. Heremans, E. M. Ku, P. Onnerud, E. M. E. Yeo, S. M. Haile, J. K. Stalick, J. D. Jorgensen, *Solid State Ionics*,2000, **129**, 111-133.

[42] C. W. Sun, U. Stimming, *J. Power Sources*, 2007, **171**, 247-260.

[43] L. C Jia, X. Wang, X, B. Hua, W. L. Li, B. Chi, J. Pu, S. L. Yuan and L. Jian, *Int. J. Hydrogen Energy*, 2012, **37**, 11941-11945.

Chapter 2 Principles of SOFC

2.1 Thermodynamics and Polarizations

2.1.1 Nernst equation

The electrochemical reaction process incurred in a fuel cell can be represented via the fundamental rules of thermodynamics in terms of efficiency and open-circuit potential (OCV). The data obtained through thermodynamic calculation can be also persuasive criteria in evaluating the performance of a practical fuel cell. Therefore, it is necessary to start from the most fundamental principles.

For any fuel cell, the maximum non-volume work which is the electrical work (W_{elec}) completed by the system equals to the change of Gibbs free energy (ΔG):

$$W_{elec} = -\Delta G \tag{2-1}$$

For example, the overall oxidation reactions of syngas in SOFC are:

$$2H_2 + O_2 \rightarrow 2H_2O \tag{2-2}$$

$$2CO + O_2 \rightarrow 2CO_2 \tag{2-3}$$

For either 1 mole of H_2 or CO is reacted, 2 moles of electrons are produced:

$$W_{elec} = EQ = 2FE \tag{2-4}$$

thus：

$$\Delta G = -2FE \tag{2-5}$$

Where F is Faraday's constant, E is the reversible voltage and Q is the quantity of electric charge produced. So under the standard condition, the reversible voltage is:

$$E^0 = \frac{-\Delta G^0}{2F} \tag{2-6}$$

The superscript "0" indicates the standard condition. Since $\Delta G = \Delta H - T\Delta S \approx \Delta H^0 - T\Delta S^0$, we can calculate the voltage of syngas (C/H = 3/2) fuelled SOFC via inserting the corresponding values at 1023 K which is a typical operating temperature for SOFC:

$\Delta H^0(H_2) = $ -241810 J mol^{-1} $\qquad\qquad$ $\Delta S^0(H_2) = $ -44.42 J mol^{-1} K^{-1}

$\Delta H^0(CO) = $ -281970 J mol^{-1} $\qquad\qquad$ $\Delta S^0(CO) = $ -86.42 J mol^{-1} K^{-1}

Then the reversible voltage equals to:

$$E^0 = -\Delta G^0/2F$$

$$= 1.01 \ V \tag{2-7}$$

Meanwhile, considering the effect of gas concentration for the reaction below：

$$aA \ (g) + bB \ (g) \rightarrow cC \ (g) \tag{2-8}$$

then:

$$\Delta G' = \Delta G^0 + RT \ln \frac{(p_C / p^\theta)^c}{(p_A / p^\theta)^a (p_B / p^\theta)^b} \tag{2-9}$$

p^θ is the standard pressure，p_X is the partial pressure of the corresponding gas,

so in syngas fuelled SOFC, the theoretical voltage should be:

$$E' = E^0 - \frac{RT}{2F} \ln \left(\frac{p_{O_2}^{0.5} \, p_{H_2}^{0.4} \, p_{CO}^{0.6}}{p_{H_2O}^{0.4} \, p_{CO_2}^{0.6}} \right)$$

(2-10)

2.1.2 Practical fuel cell efficiency

The efficiency of a fuel cell in practice is mainly consisted of three parts: thermodynamic efficiency, voltage efficiency and fuel utilization efficiency [1].

$$\varepsilon_{tot} = \varepsilon_{thermo} \times \varepsilon_{voltage} \times \varepsilon_{fuel}$$

(2-11)

Thermodynamic efficiency is the amount of energy extracted from chemical reaction available to do work relative to the total energy, which is also called reversible efficiency. The former part is related to the change of Gibbs free energy and the latter equals to the total heat released by the reaction, thus:

$$\varepsilon_{thermo} = \frac{work}{heat} = \frac{\Delta G}{\Delta H}$$

(2-12)

Voltage efficiency is defined as the ratio of fuel cell working potential over the reversible Nernst voltage. The loss of voltage is widely believed to be constituted by three parts: activation polarization, ohmic polarization and concentration polarization. Each one of them will be further discussed in the following subchapters.

$$\varepsilon_{voltage} = \frac{V_{working}}{V_{Nernst}}$$

(2-13)

Fuel utilization efficiency accounts for the fact that not all the fuel going into the fuel cell will participate in the electrochemical reaction; some may flow through the anode chamber without being oxidized. For example, the fuel utilization of a commercial stack in Versa Power Inc. is approximately 50% at operating conditions [2].

2.1.3 Activation polarization

One of the most important parameters in determining the performance of a fuel cell is the I-V curve, also called polarization curve, which describes the relationship between voltage (V) and current (I).
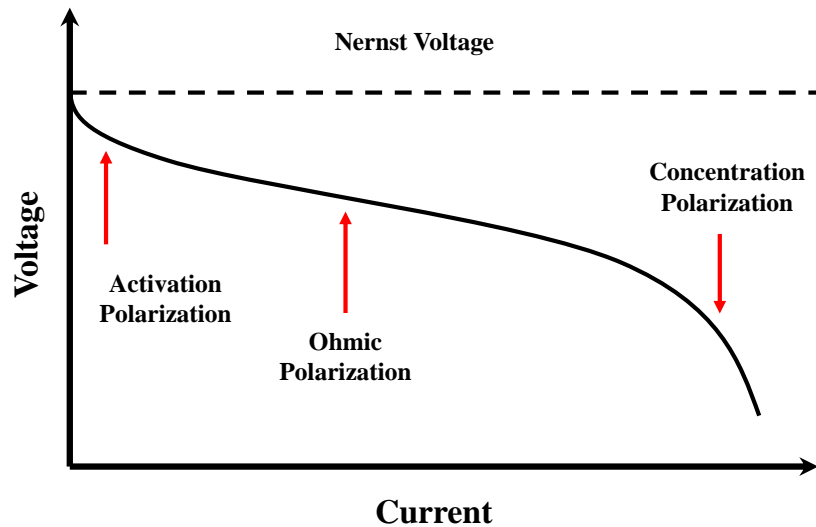
Figure 2-1 A schematic of a typical I-V curve of fuel cell.

For an ideal fuel cell system, the voltage will stabilize at a constant value equaling to Nernst potential. In practice, however, dramatic voltage drop can be

always observed in the I-V. This loss can be classified into three categories, namely activation polarization, ohmic polarization and concentration polarization, respectively. At the starting point of I-V curve, the loss is predominated by activation polarization.

Most electrochemical reactions are characterized by multi-step and reversibility. For the rate determined step, the forward and backward reactions reach equilibrium quickly, leading to the same forward and back current density: $j_{for} = j_{back} = j_0$ [1]. Herein, j_0 is defined as the exchange current density and at this point, the net current is zero. In order to overcome the energy barrier which limits the reaction kinetics, a potential difference is build up across the reaction interface, which makes the forward reaction much faster than the backward one. This potential is activation polarization (η_{act}). The relationship between current density and activation polarization can be described using the well-known Butler-Volmer (BV) equation.

$$j = j_0 \exp\left\{\frac{\alpha\eta_{act}nF}{RT}\right\} - j_0 \exp\left\{-\frac{(1-\alpha)\eta_{act}nF}{RT}\right\} \qquad (2\text{-}14)$$

Where j is the current density, α is the transfer coefficient determining the influence of interface overpotential over the activation barrier, n is the amount of substance.

There are two approximations for BV equation when η_{act} is either small or large enough. When η_{act} is small, (<15 mV at room temperature [3]), BV equation

26

can be simplified as

$$j = j_0 \left\{ \frac{\eta_{act} nF}{RT} \right\} \quad (2\text{-}15)$$

since $\lim\limits_{x \to 0} e^x = 1 + x$. This indicates a linear relationship between j and η_{act}, which

offers the possibility to measure j_0. When η_{act} large enough, the forward reaction

will dominate in BV equation, making the second term negligible and:

$$j = j_0 \exp \left\{ \frac{\alpha \eta_{act} nF}{RT} \right\} \quad (2\text{-}16)$$

Thus:

$$\eta_{act} = -\frac{RT}{\alpha nF} \ln j_0 + \frac{RT}{\alpha nF} \ln j \quad (2\text{-}17)$$

As a result, plotting η_{act} vs $\ln j$ should yield a straight line, both α and j_0 can be

calculated by the slope and intercept of fitted straight line.

2.1.4 Ohmic polarization

In the middle of the polarization curve, the quasi-linear potential loss is related

to charge transport resistance in fuel cell components predominated by ohmic

resistance. At a given current density, the corresponding ohmic voltage loss, η_{ohm},

is given by [4]:

$$\eta_{ohm} = (\rho_e l_e + \rho_c l_c + \rho_a l_a + R_{contact})j \quad (2\text{-}18)$$

ρ_e, ρ_c and ρ_a are the electrolyte, the cathode and the anode resistivity,

respectively, whereas l_e, l_c and l_a are thicknesses of the electrolyte, the cathode

and the anode, respectively; $R_{contact}$ is defined as the contact resistance.

For conventional Ni based SOFC, the ionic resistivity of YSZ at 800°C is

around 50 $\Omega \cdot cm$, the electronic resistivity of cathode material, Sr-doped LaMnO$_3$

is approximately 10^{-2} $\Omega \cdot cm$ and that of the Ni/YSZ cermet is on the order of 10^{-4}

$\Omega \cdot cm$ [4]. Thus, the ohmic polarization mainly comes from the electrolyte,

making a thin film electrolyte SOFC in high demand.

2.1.5 Concentration polarization

At high current density, mass transfer limitation controls the potential drop.

The reactants transferred to the reaction sites are inadequate to compensate the

ones reacted whereas the outgoing products are unable to diffuse out of the porous

electrode in time. Considering the fuel depletion effect, the concentration of

reactants at the electrode/electrolyte interface can be calculated through Fick's

law,

$$C_R^* = C_R^B - \frac{j\delta}{nFD^{eff}} \tag{2-19}$$

where C_R^* is the concentration of reactant at interface, C_R^B is the bulk

concentration, D^{eff} is the effective diffusivity and δ is the thickness of diffusion

layer. Consequently, the potential loss originated from diluted reactants is defined

as concentration polarization η_{conc}:

$$\eta_{conc} = E_{nernst}^B - E_{nernst}^* \tag{2-20}$$

According to a semi-empirical equation [5],

$$\eta_{conc} = -B\ln(1 - \frac{j}{j_l}) \tag{2-21}$$

B is constant predicted empirically and j_l is defined as the limiting current density

measured when C_R^* falls to zero.

2.2 SOFC Anodic Catalysis

2.2.1 Anode catalytic process

In general, the electrocatalytic reaction (ECR) process is essentially identical with conventional counterpart (CCR). Using H_2 oxidation on Ni/YSZ catalyst as an example, the catalytic process can be ascribed in the following steps [3]:

(1) chemisorption equilibrium of H_2:

$$H_2 + (Ni) + (Ni) \rightleftharpoons H(Ni) + H(Ni) \tag{2-22}$$

(2) adsorbate oxidation within triple-phase boundary (TPB):

$$H(Ni) + O^{2-}(YSZ) \rightleftharpoons (Ni) + OH^-(YSZ) + e^-(Ni) \tag{2-23}$$

$$H(Ni) + OH^-(YSZ) \rightleftharpoons (Ni) + H_2O(YSZ) + e^-(Ni) \tag{2-24}$$
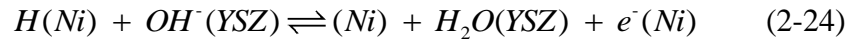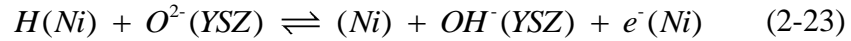
(3) desorption equilibrium of H_2O:

$$H_2O(YSZ) \rightleftharpoons H_2O + (YSZ) \tag{2-25}$$

(4) oxygen ion incorporation:

$$(YSZ) + O_O^{\times}(YSZ) \rightleftharpoons V_O^{\cdot\cdot} (YSZ) + O^{2-}(YSZ) \qquad (2\text{-}26)$$

Nevertheless, a distinguishing characteristic of ECR differing from CCR can be identified in step (2). In CCR, the readily activated H_2 can be oxidized directly upon interaction with the surrounding oxidants. In ECR, on the other hand, the red-ox process is exclusively occurred at the TPB. Once the reaction starts, a localized surface diffusion area (SDA) will be established simultaneously, which is adjacent to TPB and extends to Ni with the width of several hundreds of Angstrom [6]. When *H(Ni)* is electrochemically consumed at TPB, chemisorbed H_2 located within SDA will be driven to diffuse across SDA to TPB where they will participate following reactions as illustrated in Figure 2-2.
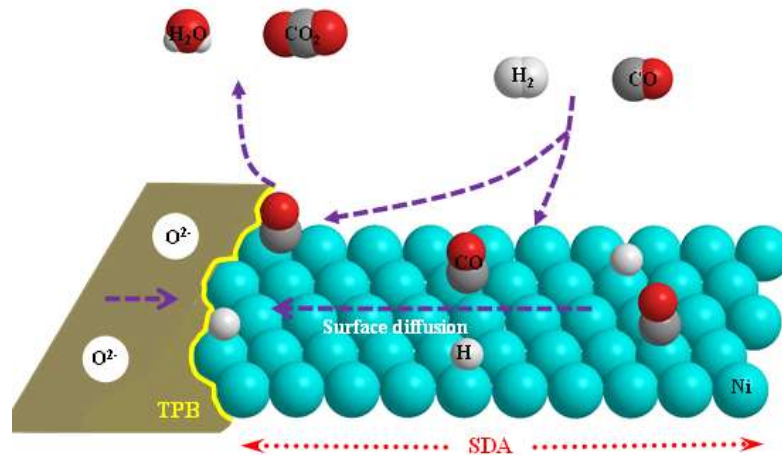
Figure 2-2 A schematic of the electrocatalytic reaction (ECR) in SOFC.

2.2.2 Anode catalyst progress

Over the last several decades of continuous efforts, tremendous progresses

have been achieved in the development of SOFC anode materials [7-24]. This subchapter will only review the symbolic milestones of the achievements.

2.2.2.1 Ni/YSZ cemet

Since the debut of Ni/YSZ introduced by Spacil in 1964 [7], this anode material has been intensively utilized in solid oxide fuel cell industry. Nowadays almost every commercially available SOFC stack anode is based on this iconic composite [8]. In this anode system, the contiguous YSZ phase acts as a framework for the dispersion of Ni while prohibiting its high temperature agglomeration. This ionic conductor can also effectively extend the length of TPB, which is beneficial to the performance increase. Meanwhile, the combination of Ni/YSZ tends to reduce the coefficient of thermal expansion (CTE) mismatch between YSZ electrolyte and anode compared with using Ni alone. Last but not the least, excellent elevated temperature compatibility of the two phases is another credit enabling the application of co-firing technique in the preparation of thin film SOFC. Nonetheless, Ni is prone to suffer coking, sulfur poisoning and red-ox instability, which makes the research for its alternatives a critical task.

2.2.2.2 Ceria

Good carbon resistance and relatively high sulfur tolerance make ceria based anode catalyst very promising. Ceria acts as the active phase catalyzing the fuel oxidation due to the presence of the red-ox couple of Ce^{4+} to Ce^{3+} [9]. Accordingly, ceria based SOFC permits the direct usage of dry methane as the fuel and is able to operate at H_2S level up to 450ppm without apparent loss of

performance [10, 11]. However, its low electronic conductivity necessitates the coupling of another conductive phase, such as coke resistant Cu, before the application in SOFC. Recently, in order to increase its catalytic activity, nano-sized noble metal particles were uniformly distributed on the ceria surface, or even designed to form metal-ceria core-shell structures [12].

2.2.2.3 Perovskite oxides

The chemical formula of perovskite oxide is ABO_3, A is the larger cation and B is the smaller cation. In this structure, the B cation is 6-fold coordinated and the A cation is 12-fold coordinated with the oxygen anions. In SOFC anode catalyst, the A-site is usually alkaline earth metal elements whereas transition metal elements are commonly filled into B-site. In order to acquire sufficient electrocatalytic capability, adequate electric conductivity as well as acceptable stability, substitution of parent cations with similar-sized ones occupying different valences is applied and preferable defects can be introduced into the structure.

Up to date, there are mainly three series of perovskite anode catalysts including chromate, titanate and vanadate. To meet the requirements of anode catalyst, co-doping of both A- and B- sites has become a widely followed strategy in tailoring the parent oxide properties [13-17]. Typical catalysts of this category contain $La_{0.75}Sr_{0.25}Cr_{0.5}Mn_{0.5}O_{3-\delta}$, B-site doped $La_{0.3}Sr_{0.7}TiO_{3-\delta}$ and B-site doped $La_{0.75}Sr_{0.25}VO_{3-\delta}$. Presently, in order to overcome their disadvantages such as low catalytic activity, more active species have been introduced into the anode oxide matrix through either ex-solution upon reduction or direct infiltration [12, 16, 17].

These secondary phases contribute considerably to the SOFC performance maximization.

2.2.2.4 Miscellaneous complex oxides

In addition to perovskite oxides, a variety of complex oxides have been reported using as anode candidate materials. For instance, Slater et $al.$ [18, 19] investigated tungsten bronze materials with the compositions of $(Ba/Sr/Ca/La)_{0.6}M_xNb_{1-x}O_{3-\delta}$ (with M = Mg or In) as potential anode. They had good conductivity characteristics and were stable after prolonged reduction treatment.

The pyrochlore-type oxides, with a general formula of $A_2B_2O_7$, were also proposed as candidate materials. At 1000 °C, the ionic conductivity of $(Gd_{0.98}Ca_{0.02})_2Ti_2O_7$ was about 10^{-2} S cm^{-1}, which was comparable to YSZ [20, 21]. When it was further doped with Mo, high mixed ionic and electronic conductivity under reducing condition was observed, making it suitable as an anode material [22].

Recently it was reported that the combination of Ni and $BaZr_{0.1}Ce_{0.7}Y_{0.2-x}Yb_xO_{3-d}$ had high tolerance to coking and sulfur poisoning while maintaining outstanding catalytic activity [23]. Yun-Hui Huang et $al.$ [24] developed a double perovskite anode material Sr_2MgMoO_6 which showed a comparable performance with Ni in hydrogen and methane fuels. It could also tolerate up to 50 ppm H_2S without apparent performance degradation ($< 5\%$) upon 200 h longevity test.

2.3 SOFC in Practice

2.3.1 Fuels processing

Currently, before the raw feedstock is ready to be electrochemically oxidized by SOFC, fuel processing is always mandatory to ensure good performance of SOFC. Take natural gas treatment as an example, the impurity such as H_2S in the sour gas must be removed via desulfurization process, otherwise both the anode catalyst and other SOFC stack component will be at risk of deactivation and corrosion, respectively. Since purified CH_4 can easily cause coking issue on Ni catalyst, an extra component named external steam reformer is required to be installed in a SOFC stack to reform CH_4 into syngas. With adequate amount of steam and sufficient SOFC fuel utilization applied, coke from syngas can be suppressed [25].
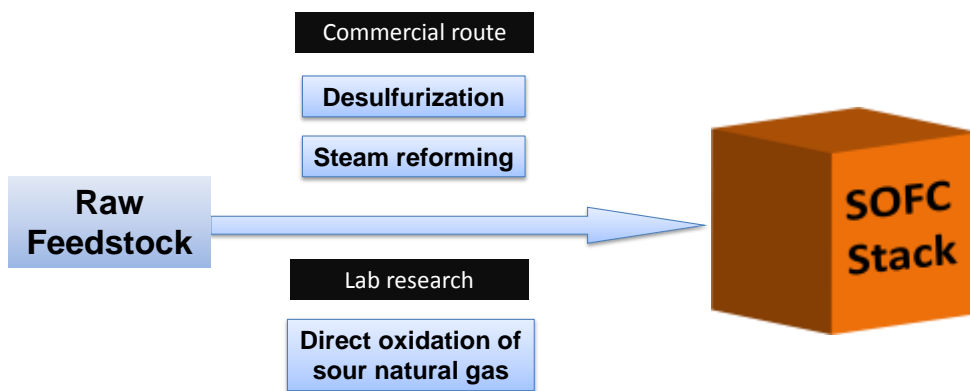
Figure 2-3 SOFC raw feedstock processing routes.

In order to reduce the technical complexity, direct oxidation of raw feedstock

has been proposed. In this route, neither of the previous mentioned treatments is required to deal with the corrosive fuels. However, the simplification of fuel processing adds higher requirements to the SOFC system [26-27].

2.3.2 Single cell design
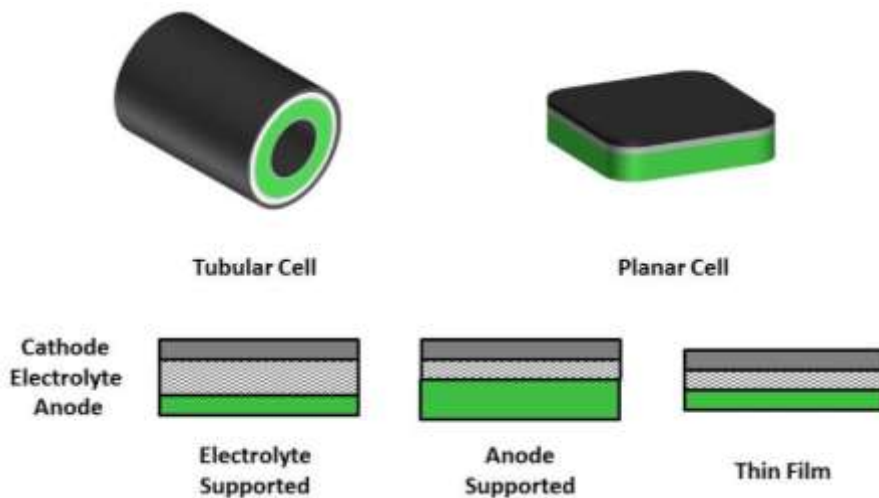
Figure 2-4 Single cell design and development routes.

Basically, SOFC design can be divided into two major categories: tubular cell and planar cell (Fig. 2-4). Because of technical issues such as fabrication/testing complexity, inefficient current collection and sequential lower power density, the majority of attentions have been paid to the planar cells development, especially in the research laboratories where the performance determination of proposed electrode catalyst candidate is the main concern. Therefore, all the cells to be discussed in this thesis will be planar cells.

Planar SOFC developed in the early stage was usually electrolyte supported in which the thick electrolyte also provided mechanical support to both of the thin electrodes films. Because of high ohmic resistance of commonly used electrolyte materials, electrolyte supported SOFC inevitably suffers high ohmic polarization loss. Anode supported design significantly reduces the thickness of electrolyte and the internal ohmic resistance of fuel cell, thus was applied in most of commercial SOFC. Major issues associated with this structure were believed to be red-ox and longevity operation instability. Recently, SOFC design has progressed to thin film electrolyte supported, however, the electrolyte thickness has decreased to obtain an excellent balance between performance and durability.

2.3.3 Stack components

In addition to the single cell, several critical components also play important roles in a SOFC stack in which all the single cells are packed in series. In order to separate the air flow transporting through the cathode chamber and the fuel flow from the anode chamber of the adjacent cell, a conductive interconnect is allocated between the upper and the lower cell (Fig. 2-5). Meanwhile, two current collectors are attached to both sides of the interconnect serving to collect and conduct the current generated by the electrodes. In H_2S containing hydrocarbon fuelled SOFC, sulfur and coke resistance is mandatory requirements for the anode current collector, which are not possessed by conventional ones. Therefore, novel materials have to be developed to address the problem.
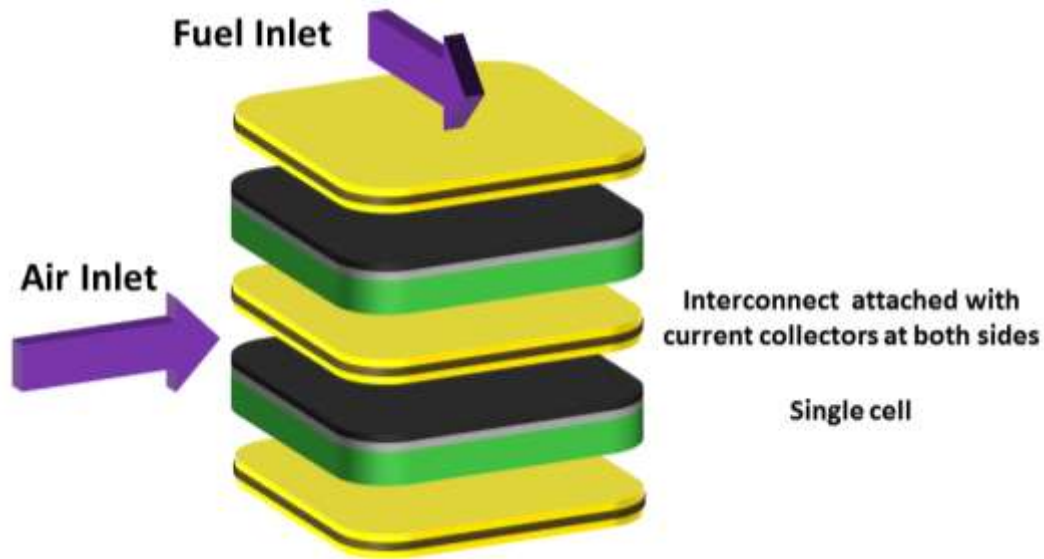
Figure 2-5 A typical structure of planar SOFC stack.

References:

[1] R. O'hayre, *et al.*, "Fuel Cell Fundamentals", Chapter 3, John Wiley& Sons Inc., New York, 2006

[2] B. Borglum, 10th Annual SECA Workshop, Pittsburgh, PA, USA, July 15, 2009.

[3] H. Zhu, R. J. Kee, V. M. Janardhanan, O. Deutschmann, and D. G. Goodwin. *J. Electrochem. Soc.*, 2005, **152**, A2427–A2440.

[4] S. C. Singhal，K. Kendall. "High Temperature Solid Oxide Fuel Cells: Fundamental, Design and Application", Chapter 9, Elsevier Limited, Amsterdam, 2003.

[5] Matthew M. Mench, "Fuel Cell engines", Chapter 4, John Wiley& Sons Inc.,

New Jersey, 2008.

[6] R. E. Williford and L. A. Chick, *Surf. Sci.*, 2003, **547**, 421-437.

[7] H. S. Spacil, US Patent 3,558,360; filed October 30, 1964, modified November 2, 1967, granted March 31, 1970.

[8] C. W. Sun, U. Stimming, *J. Power Sources*, 2007, **171**, 247-260.

[9] S. Park, J. M. Vohs and R. J. Gorte, *Nature*, 2000, **404**, 265-267.

[10] H. He, R. J. Gorte, *Solid State Lett.*, 2005, **8**, A279-A280.

[11] R. J. Gorte and J. M. Vohs, *J. Catal.*, 2003, **216**, 477-486.

[12] J. S. Kim, N. L. Wieder, A. J. Abraham, M. Cargnello, P. Fornasiero, R. J. Gorte and J. M. Voh, *J. Electrochem. Soc.*, 2011, 158, B596-B600.

[13] S. W. Tao, J. T. S. Irvine, *Nat. Mater.*, 2003, **2**, 320-323.

[14] D. P. Fagg, V. V. Kharton, A. V. Kovalevsky, A. P. Viskup, E. N. Naumovich, J. R. Frade, *J. Eur. Ceram. Soc.*, 2001, **21**, 1831-1835.

[15] Z. Cheng, S. W. Zha, L. Aguilar, D. Wang, J. Winnick, M. L. Liu, *Electrochem. Solid State Lett.*, 2006, **9**, A31-A33.

[16] W. Kobsiriphat, B. D. Madsen, Y. Wang, L. D. Marks and S. A. Barnett, *Solid State Ionics*, 2009, **180**, 257-264.

[17] G. L. Xiao, C. Jin, Q. Liu, A. Heyden and F. L. Chen, *J. Power Sources*, 2012, **201**, 43-48.

[18] P. R. Slater, J. T. S. Irvine, *Solid State Ionics*, 1999, **124 (1–2)**, 61-72.

[19] P. R. Slater, J. T. S. Irvine, *Solid State Ionics*, 1999, **120 (1–4)**, 125-134.

[20] S. Kramer, M. Spears, H. L. Tuller, *Solid State Ionics*, 1994, **72**, 59-66.

[21] S. A. Kramer, H. L. Tuller, *Solid State Ionics*, 1995, **82**, 15-23.

[22] O. Porat, C. Heremans, H. L. Tuller, *Solid State Ionics*, 1997, **94**, 75-83.

[23] L. Yang, S. Z. Wang, K. Blinn, M. F. Liu, Z. Liu, Z. Cheng and M. L. Liu, *Science*, 2009, **326**, 126-129

[24] Y. H. Huang, R. I. Dass, J. C. Denyszyn and J. B. Goodenough, *Electrochem. Commun.*, 2007, **9**, 1881-1885.

[25] J. R. Rostrup-Nielson, *Catal. Today*, 1993, **18**, 305-324.

[26] A. L. Dicks, *J. Power Sources*, 1996, **61**, 113-124.

[27] B. C. H. Steele, A. Heinzel, *Nature*, 2001, **414**, 345-352.

Chapter 3 Methodology

3.1 Materials Preparations

The homemade $BaCe_{0.7}Zr_{0.1}Y_{0.2}O_{3-\delta}$ (BZCY) electrolyte material and $Ba_{0.5}Pr_{0.5}CoO_{3-\delta}$ (BPC) cathode catalyst reported in Chapter 5 and 6 were synthesized via sol-gel auto-combustion method. The preparation of BZCY was detailed here as an example and illustrated in Fig. 3-1. Firstly, stoichiometric amounts of $Ba(NO_3)_2$, $ZrO(NO_3)_2 \cdot xH_2O$, $Ce(NO_3)_3 \cdot 6H_2O$ and $Y(NO_3)_3 \cdot 6H_2O$ were first dissolved in deionized water. Subsequently, citric acid and NH_4NO_3 were added as chelating agent and as oxidant, respectively. The molar ratio of citric acid: total metal ions: NH_4NO_3 was 1.5: 1: 3. The pH of the resulting solution was adjusted to about 8 using ammonium hydroxide and heated on a hot plate. After water evaporation, the residue foamy gel was self-ignited to form fine powder. Then the as-combusted powders were calcined at 1100 ^{o}C for 10 h in air to form pure perovsikte phase.

$Ba_{0.5}Pr_{0.5}CoO_{3-\delta}$ (BPC) cathode catalyst was synthesized via a similar technical route.

40
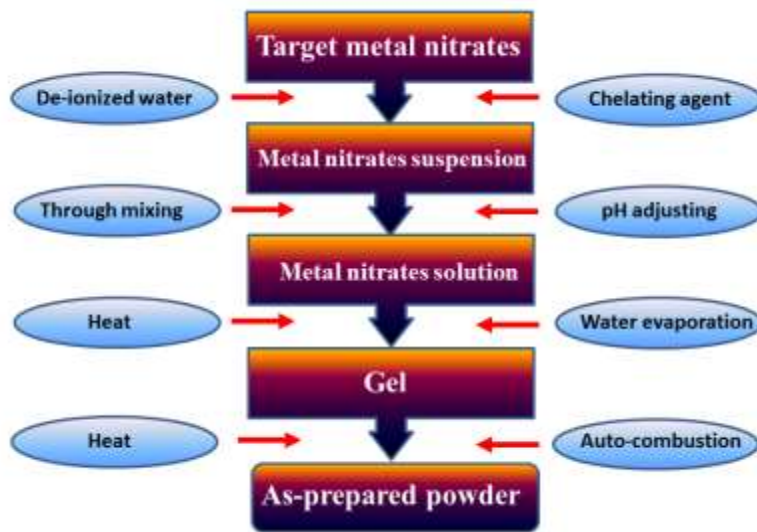
Figure 3-1 Flow chart of sol-gel auto-combustion method.

3.2 Materials Characterizations

3.2.1 X-ray diffraction (XRD)

XRD is a technique to determine the crystallographic structure of the investigated materials. The incident beam of X-ray is able to be diffracted by the crystalline atoms into many specific directions. The intensities and angles of those diffracted beams were recorded which reveal various information such as lattice parameters, defects or disorders and grain size of nanoparticles. Power diffraction and thin film diffraction are two commonly used XRD modes in the study of inorganic materials. The difference of the two modes is that in thin film diffraction, the incident beam of X-ray is fixed at a very small angle ($< 5^\text{o}$)

relative to the sample surface tangential direction, which is helpful in the characterization of thin film materials.

In this thesis, powder diffraction was performed using a Rigaku Rotaflex X-ray diffractometer with Co Ka radiation and the data were analyzed using JADE software.

3.2.2 Scanning electron microscope (SEM)

SEM is a powerful technique in the achievement of imaging information on surface morphology and composition. In this equipment, a high-energy beam of electron is scanned on the sample surface, generating signals such as secondary electrons (SE) and back scattered electrons (BE). SE signal is mainly used to obtain the images on the topographic information whereas BE signal is capable of providing compositional information of the surface. However, conventional SEM is equipped with a thermionic electron sources having relative low brightness and thermal drift during operation which negatively affect the resolution of the image. Field emission is one way of generating electrons that avoids these problems. In field emission (FE) SEM, the electron beam is generated using a cold cathode field emitter and the emission is reached by placing the filament in a huge electrical potential gradient. Thus, cleaner and higher resolution (~ 2 nm) image can be obtained via FE-SEM.

In this thesis, morphologies of samples were determined using a Hitachi S-2700 SEM and high resolution images were obtained using a JEOL 6301F FE-SEM equipped with a TGP x-ray analysis system for the acquisition of elemental information.

3.2.3 Energy dispersive X-ray spectroscopy (EDS)

EDS is usually an accessory coupled with SEM apparatus for elemental analysis. Normally, the incident high energy beam of electrons may excite an electron in an inner shell of an atom, ejecting it out of the shell and creating an electron hole at the mean time. Therefore, an electron from an outer, higher-energy shell then fills the hole, and the energy difference between the outer and the inner shell may be released in the form of an X-ray. The energy of the characteristic X-rays are measured to determine the elements present and the relative energy intensity difference among different elements also allows the quantitative measurement of elemental surface concentration.

In this thesis, surface composition of samples were determined using a EDS attached with Hitachi S-2700 SEM.

3.2.4 X-ray photoelectron spectroscopy (XPS)

XPS is a surface-sensitive spectroscopic technique that determines the composition, chemical and electronic state, and the surface film thickness (<10 nm) of the sample. The principle of this equipment is similar with EDX, XPS spectra are obtained by irradiating a material with a beam of X-rays instead of electrons in EDX, while simultaneously measuring the number of electrons that escape from the surface of the material and determining the kinetic energy of them.

In this thesis, XPS was performed using a Kratos Analytical AXIS 165. A monochromated Al Ka ($hv = 1486.6$ eV) source was used at a power of 210 W, the base pressure in the analytical chamber was maintained at of 3×10^{-8} Pa. The obtained spectra were analyzed using the Thermo Avantage software referenced to the C 1s binding energy of 285.0 eV. For curve fitting and de-convolution, a shirley-type background subtraction and a Gaussian–Lorentzian peak shape were applied.

3.3 SOFC Button Cell Preparations

Anode supported SOFC design was applied in the work described in Chapter 3 and 5-7 for both oxygen-ion conducting SOFC and proton-conducting SOFC. All the button cells were fabricated via a spin coating process which is illustrated

in Fig. 3-2. Herein, the preparation of oxygen-ion conducting SOFC is detailed as an example.
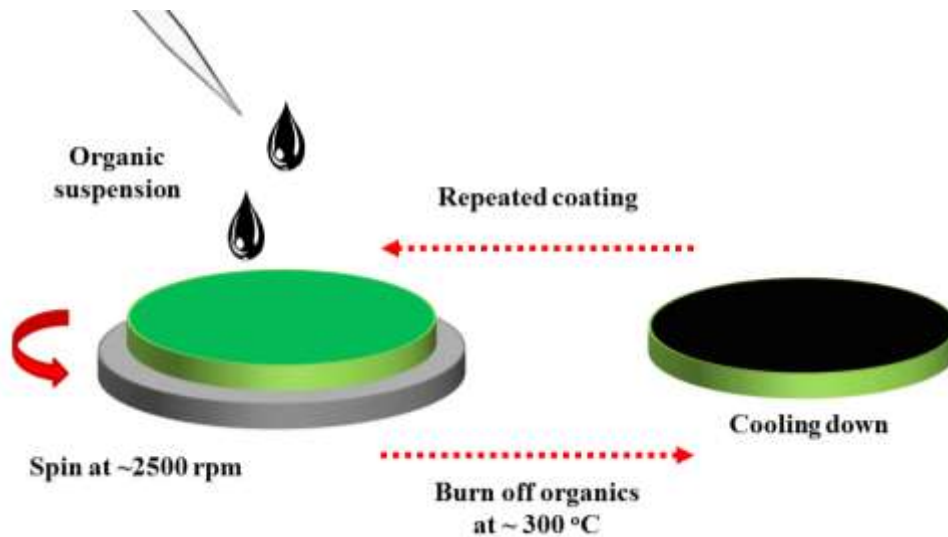
Figure 3-2 A schematic of spin coating for the fabrication of electrolyte and electrode thin films.

To fabricate the anode support substrate, 33 wt% YSZ (yttria-stabilized zirconia; TZ-8Y, Tosoh Corporation), 45 wt% NiO and 22 wt% corn starch were initially mixed in ethanol for 24 h using a ball-milling process. After drying the milled slurry, the powder was sieved through a 150-mesh screen to produce a uniform and fine particle mixture. The resulting powder was pressed into discs of 2.54 cm in diameter and then sintered at 1100 ^{o}C for 2 h to obtain strong substrates.

The composition of anode functional layer starting materials was chosen as 50 wt% NiO + 50 wt% YSZ. The powder mixture was produced by ball milling

for 24 h. The electrolyte material was YSZ. The cathode material was a mixture of 50 wt% $La_{0.8}Sr_{0.2}MnO_{3-\delta}$ (LSM-20, Fuel Cell Materials) and 50 wt% YSZ. The anode functional layer and YSZ electrolyte thin film were applied sequentially onto the pre-sintered anode support using spin coating. Then the half-cell was sintered at 1400 ^{o}C for 4 h. Finally, the composite cathode layer was coated onto the densified electrolyte using spin coating and then sintered at 1150 ^{o}C for 2 h.

The proton-conducting SOFC was fabricated via a similar route. Notable differences were that the BZCY electrolyte densification was carried out at 1420 ^{o}C for 4 h and the final BPC/BZCY cathode layer coated on the BZCY electrolyte was sintered at 1000 ^{o}C for 2 h.

3.4 SOFC Button Cell Tests

The SOFCs button cells were set up by securing the MEA between a coaxial pair of alumina tubes using ceramic sealant, which was cured by heating in a Thermolyne F79300 tubular furnace. When the anticipated temperature was reached and the fuel cells conditioning processes, specified in each individual chapter were completed, the impedance and current-voltage characteristics were determined using a Solartron 1287 electrochemical interface together with a 1255B frequency response analyzer. The impedance spectra of cells were obtained under open circuit with AC amplitude of 10 mV and the frequency range from 0.1 Hz to 100 KHz.

The anode effluent gas composition from the anode chamber prior to and after the electrochemical reactions was analyzed using a Hewlett-Packard model HP5890 gas chromatography (GC) equipped with a packed bed column operated at 80 ^{o}C with a thermal conductivity detector. The variation of anode effluent gas composition as functions of either SOFC applied voltage or operating time was monitored continuously using a Thermostar QMS 200 mass spectrometer (MS). The entirely SOFC button cell test set-up was illustrated in Fig. 3-3.
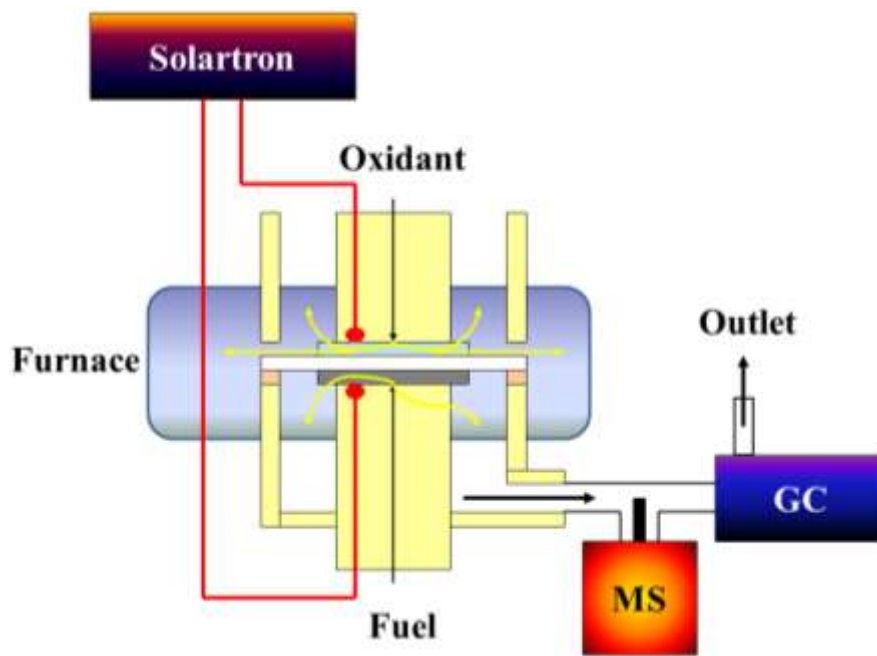
Figure 3-3 A schematic of SOFC button cell test set-up.

Chapter 4 Ni-P Coated Ni Foam as Coking

Resistant Current Collector

4.1 Introduction

Syngas, a mixture of hydrogen and carbon monoxide (H_2 + CO), has gained increasing interest as fuel for solid oxide fuel cells (SOFC) due to its lower price and high abundance relative to pure H_2 [1-4]. When SOFC design is based on electrode support rather than electrolyte support, the optimum operating temperature is decreased from ~1000 ^{o}C to ~750 ^{o}C, which makes the use of metallic current collectors (i.e., the interconnect) economically feasible [5]. However, the use of metallic components in syngas fuel at elevated temperature may lead to severe coking, also known as metal dusting, resulting in performance degradation during long term operation [6, 7].

Great efforts have been made to protect metals against metal dusting in carbon containing atmospheres [8-10]. For example, carbon deposition is suppressed when H_2S is present in feeds such as syngas or natural gas [8]; however, H_2S poisons Ni anode catalyst [11]. Dense, uniform oxide layers have been applied in attempts to provide protections [9], but their low electronic conductivity does not meet the requirements for use as current collector. Although

electroplated Cu is effective in protecting Ni [10], it is difficult to form uniformly thick deposits on a highly porous matrix such as Ni foam. Also, a high Cu/Ni ratio is needed to inhibit carbon deposition.

Electroless plating of Ni-P coatings is a well-known commercial process which has been applied in many fields owning to its excellent capability to provide coatings with good corrosion resistance, high uniformity of the deposits on complex shapes, low cost and outstanding compatibility with the metal matrix [12, 13]. However, there have been no reports regarding the application of Ni-P as coking resistant coating for current collectors. In this work, Ni-P alloy was electrolessly plated onto Ni foam current collectors. The resistance to carbon deposition onto the plated Ni foam was studied and the performance of syngas SOFC with plated current collector was also investigated.

4.2 Experimental

The Ni foam used is a commercial product (1.7 mm thick, 0.51 g cm^{-2}), INCOFOAM$^{\circledR}$ from Vale Canada Ltd. It was cut into 1cm x 1cm squares and treated with ultrasonic bath in ethanol for 30 min, then those samples were washed with de-ionized water ultrasonically for 10 min.

Both homemade and commercial electroless plating solutions from Alfa Aesar were adapted in this experiment to achieve different compositions of the coating. The composition of homemade solution was: $NiSO_4$ $6H_2O$ 0.23 mol L^{-1};

NaH_2PO_2 H_2O 0.17 mol L^{-1} and $Na_3C_6H_5O_7$ $2H_2O$ 0.27 mol L^{-1}. Before plating, Ni foam samples were immersed into plating solution and evacuated (<20 kPa) for 5 min to remove bubbles that formed on the foam. Then the solution was heated up to 85 ^oC in a water bath at which it was held for 10~30 min during the plating process. After plating all the plated samples were rinsed with de-ionized water and dried in a stream of air. Both plated and naked Ni foam samples were put into a quartz tube and treated with syngas (60% CO + 40% H_2). The weight gains corresponding to the amounts of carbon deposites were determined as a function of temperature and duration of exposure.

The most widely used anode supported SOFC design was selected in this experiment [14-16]. XRD, SEM and EDS analysises were performed in this chapter. Plated Ni foam and Au mesh were used as anode and cathode current collectors during fuel cell tests. The active area of the button cell was 0.25 cm^2, anode fuel flow rate was 50ml min^{-1} whereas cathode air flow rate was 100ml min^{-1}.

4.3 Results and Discussions

4.3.1 Characterization of Ni-P coatings

Fig. 4-1 shows the XRD patterns of samples before and after high temperature treatment in H_2 for 6 h. The diffraction peaks in XRD patterns for

samples were wide before high temperature operation, indicating that the initial Ni-P coatings on Ni foam were amorphous. However, after high temperature treatment, the meta-stable phase transformed into more stable Ni and Ni_3P crystalline phases. Thus, the surface composition of plated Ni foam current collector comprised mainly metallic Ni and Ni_3P during SOFC operation at elevated temperatures. EDS analysis showed that the P content of different coatings depended on the plating conditions as shown in Table 4-1. After electroless plating, the porosity of plated Ni foam decreased to 52.3% from original 66.2% based on the weight gains.

Table 4-1 P content of coatings.

Sample	P content in the coating (wt%)
Ni-P-L	1.2
Ni-P-M	6.5
Ni-P-H	10.7
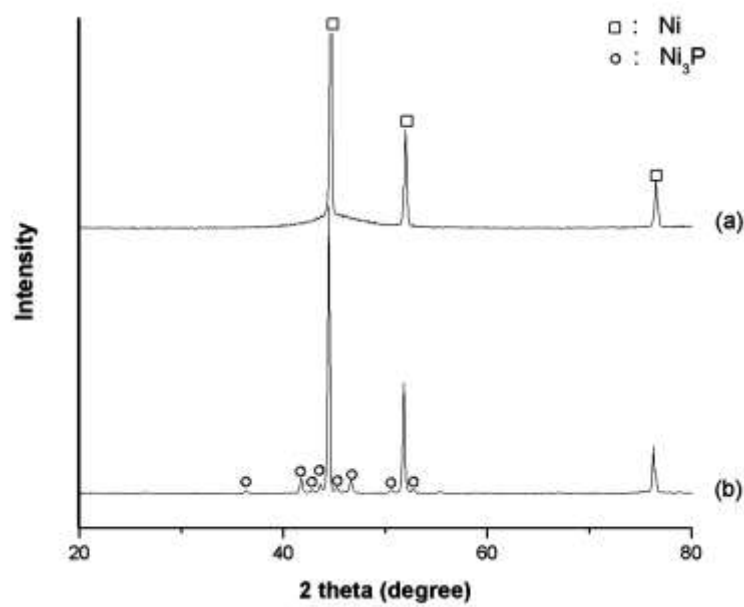
Figure 4-1 XRD patterns of (a) plated Ni foam before heat treatment; (b) plated

Ni foam after heat treatment in H_2 at $750\,^{\circ}C$ for 6 h.
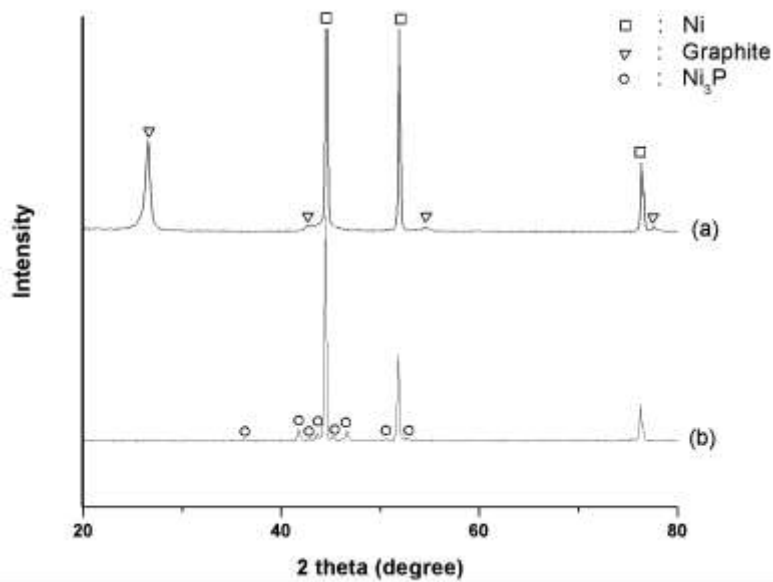
Figure 4-2 XRD patterns of (a) naked Ni foam; (b) plated Ni foam, after treatment

in syngas at $750\,^{\circ}C$ for 24 h.

4.3.2 Carbon deposition tests

Fig. 4-3 shows photographs of samples with different P content in the coatings after the treatment in syngas at 750 ^{o}C for 24 h. Both naked Ni foam and the plated Ni foam with 1.2 wt% P (sample: Ni-P-L) turned black and brittle whereas there was no apparent surface change for the plated Ni foams with higher P content of 6.5 wt% (sample: Ni-P-M) and 10.7 wt% (sample: Ni-P-H). The weight gains of the samples of naked Ni foam and Ni-P-L each were more than 50%, resulted from high carbon deposition, whereas there was very little weight
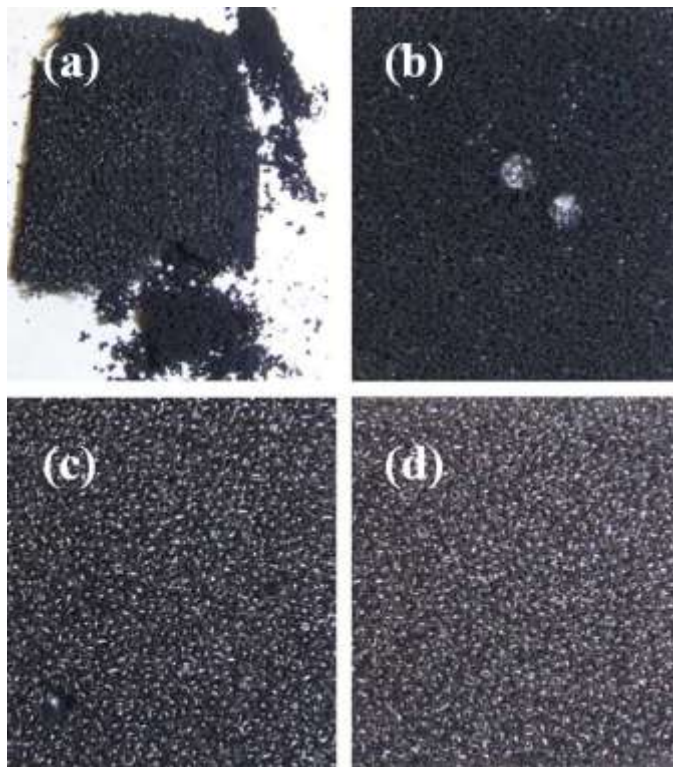
Figure 4-3 Photographs of (a) naked Ni foam; (b) Ni-P-L; (c) Ni-P-M; (d) Ni-P-H, after treatment in syngas at 750 ^{o}C for 24 h.

change for Ni-P-M and Ni-P-H. XRD patterns (Fig. 4-1, 2) also confirmed that no carbon was deposited on Ni-P-M. Thus the sample of Ni-P-M was chosen as the coating for the following parametric studies.
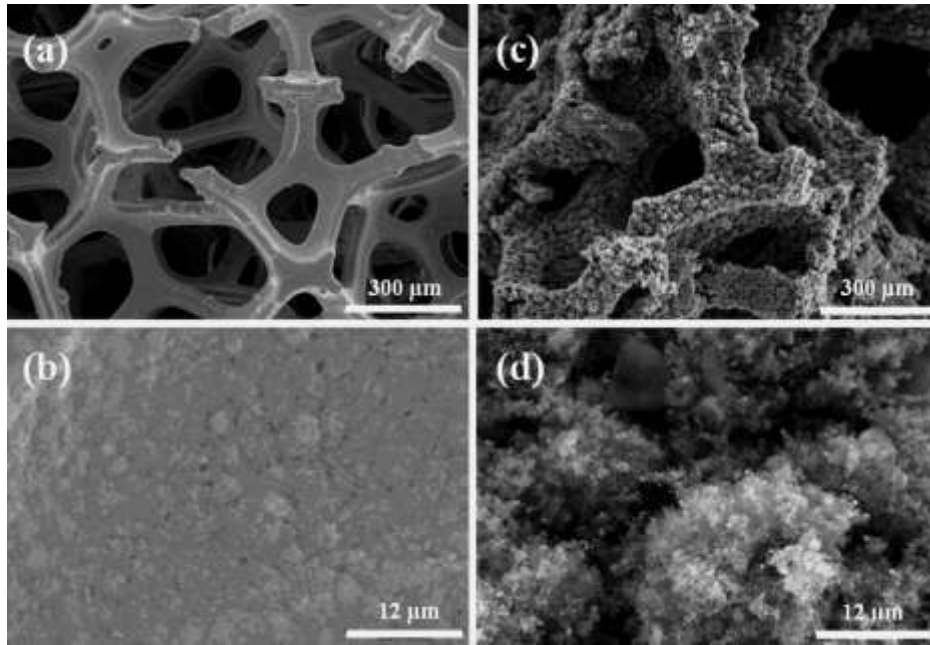
Figure 4-4 SEM images of (a, b) Ni-P-M; (c, d) naked Ni foam, after treatment in syngas at 750 $^{\circ}$C for 24 h.

The amount of carbon deposition from syngas on both naked Ni foam and Ni-P-M was determined as a function of temperature and duration of exposure. SEM images (Fig. 4-4) showed that the surface of naked Ni foam was fully covered with graphite, and the sample became brittle and lost its integrity after the treatment in dry syngas at 750 $^{\circ}$C for 24 h. In contrast, the plated Ni foam was still

shiny with no detectable carbon deposits on the surface and no apparent mechanical strength loss. Fig. 4-5 shows the weight gain as a function of time for naked Ni foam and Ni-P-M after being exposed to dry syngas for at 750 ^{o}C. The amount of coking on naked Ni foam increased dramatically and there was a 247 % weight gain after 48 h treatment in syngas. In contrast, there was no obvious weight change for plated Ni foam during the same exposure time. Fig. 4-6 demonstrates the superior carbon deposition resistance of plated Ni foam when compared to naked Ni foam in dry syngas for 24 h at temperatures between 600 ^{o}C and 800 ^{o}C.
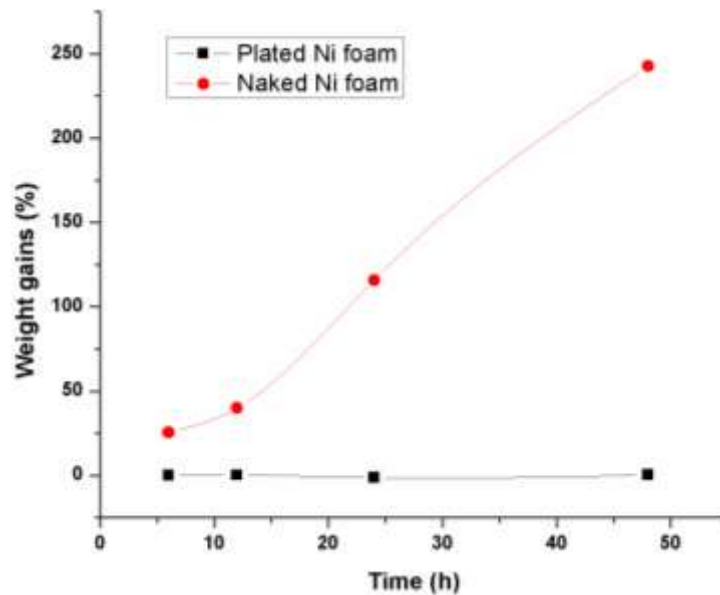
Figure 4-5 Weight gains of naked and plated Ni foam after treatment in syngas at 750 ^{o}C for 48 h.
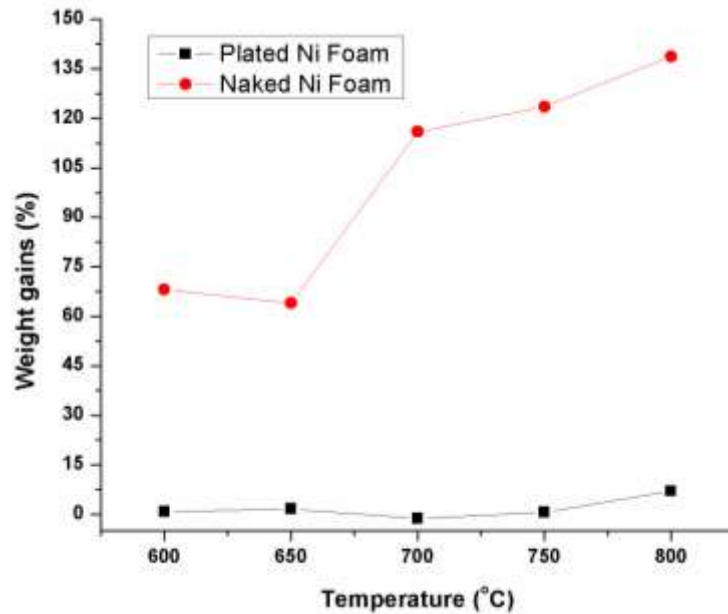
Figure 4-6 Weight gains of naked and plated Ni foam after treatment in syngas for 48 h as a function of temperature between 600 ^{o}C and 800 ^{o}C.

Carbon deposition on metallic Ni in syngas was studied by many researchers [e.g. 7, 17]. There are two main reactions that are sources of carbon:

$$CO + H_2 \rightarrow C + H_2O \qquad\qquad (4\text{-}1)$$

$$2CO \rightarrow CO_2 + C \qquad\qquad (4\text{-}2)$$
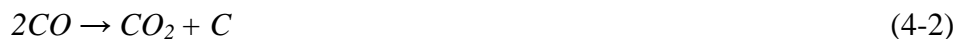
Reaction (1) was believed to be the predominant reaction due to its higher rate [17]. The carbon formed on the metal surface from reactions of gaseous phases diffused into the bulk and the Ni foam structure was destroyed by direct inward growth of carbon [18]. The coking resistance mechanism of Ni-P coatings is attributable to dilution or poisoning of Ni surface active sites at which C is formed through deposition of inert Ni_3P. This inert phase changes the type and structure

56

of chemisorbed species from syngas. Similar mechanisms have been reported for coking-free catalysts such as sulfur-passivated Ni and copper-diluted Ni [19-21].

4.3.3 Fuel cell tests

Fig. 4-7 shows a SEM image of a fuel cell cross-section after testing. The thicknesses of the respective layers were: (1) Ni-YSZ anode support substrate: ~800 μm; (2) Ni-YSZ anode functional layer: ~15 μm; (3) YSZ electrolyte ~10 μm; (4) LSM/YSZ composite cathode: ~30 μm. The YSZ electrolyte was dense, which was also proven by the open circuit potential (OCV) (Fig. 4-8; >1.15 V in H_2). The fuel cell had a low area specific resistance (ASR; Fig. 4-9) and exhibited
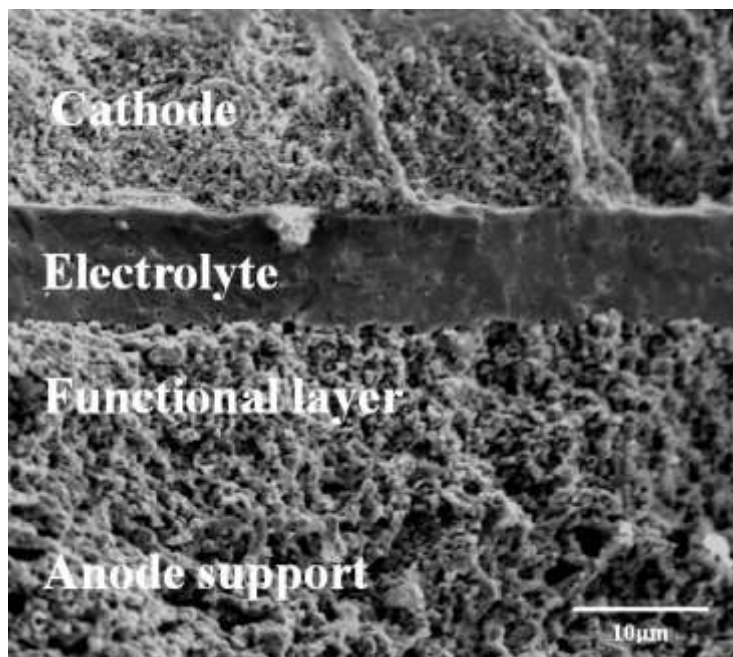
Figure 4-7 SEM cross-section image of a typical tested fuel cell.

57

maximum power densities of 0.38 W cm^{-2}, 0.59 W cm^{-2}, 0.94 W cm^{-2} and 1.32 W cm^{-2} at 700 $^{\circ}$C, 750 $^{\circ}$C, 800 $^{\circ}$C and 850 $^{\circ}$C, respectively (Fig. 4-8). Thus the low ASR fuel cells provided a good platform for comparison testing of current collectors since their performances were very sensitive to changes in system internal ohmic resistance.
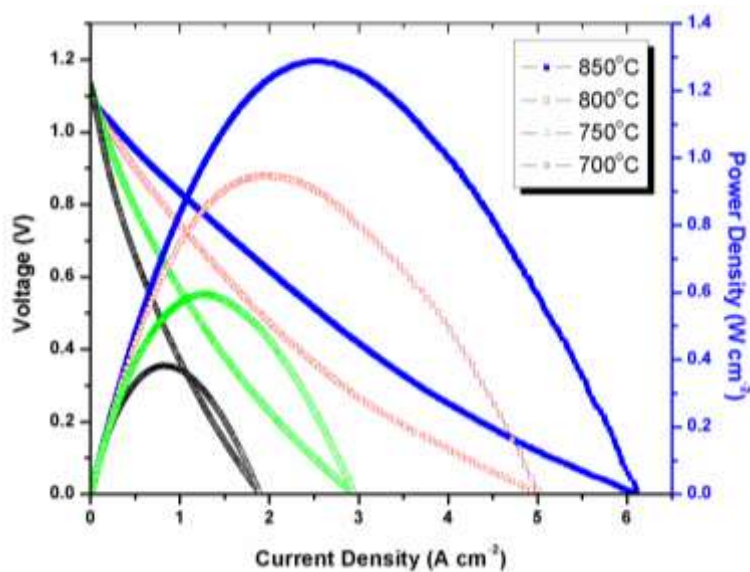
Figure 4-8 Current-voltage characteristics and power densities of a typical SOFC fuel cell in H$_2$ at different temperatures.

Fig. 4-10 shows the voltage-current characteristics and power density curves of two fuel cells tested at 800 $^{\circ}$C in H$_2$ using Ni-P-M and naked Ni foam current collector, respectively. Both cells had good power densities (>900 mW cm^{-2}) and low ohmic resistance (Fig. 4-11), indicating the good electronic conductivity of both naked and plated Ni foams. From the IV curve of the plated Ni foam group,

it was observed that the small decrease in porosity after plating had little influence on mass transport. The different shape of EIS curve for naked Ni foam group was caused by extra water present in the electrode originated from leakage. However, the EIS curves revealed that Ni-P-M had slightly higher ohmic resistance. The cause might be either higher contact resistance, as plated Ni foam is more rigid than naked Ni foam [22], or the small overall increase in thickness of the material.
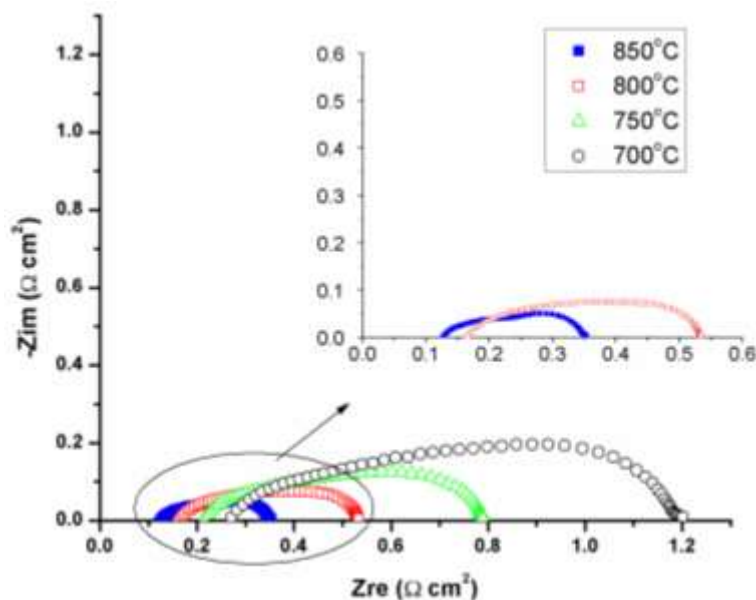
Figure 4-9 Electrochemical impedance spectra of a typical SOFC fuel cell in H_2 at different temperatures.

For comparison of plated Ni foam with a current collector of known performance, the performances of otherwise identical fuel cells fed with humidified syngas at $800\,^{\circ}C$ also were determined using Au mesh and Ni-P-M as anode current collectors. The Au current collector was chosen for the comparison

since it has high conductivity and stability in sygnas at elevated temperature [10].

The peak power densities for cells with Au mesh and plated Ni foam current

collector were high and almost identical (~800 mW cm^{-2}) as shown in Fig. 4-12.

From the EIS curves (Fig. 4-13) it was found that the internal ohmic resistance of

cell with Ni-P-M collector was very close to that with Au mesh current collector

in syngas, which suggested that plated Ni foam had similar excellent conductivity

when used in the syngas at the cell's operating temperature.
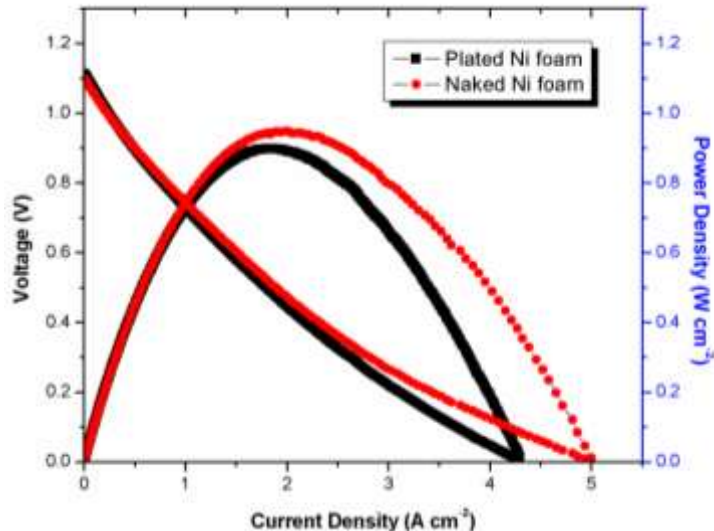
Figure 4-10 Comparison of current-voltage characteristics and power densities of

SOFC with plated and naked Ni foam anode current collectors in H$_2$ at 800 ^{o}C.

Although the behaviors and stabilities of plated Ni foams had been evaluated

by heating in syngas in the quartz tube, it also was necessary to evaluate their

performances as current collectors in an operating fuel cell system because the

working fuel cell environment is more complex: (1) the current collectors are in

contact with the cell electrodes at high temperature, thus the pressure might damage the coatings and there might be reactions between syngas and current collectors; and (2) the electrochemical reaction products (CO_2 and H_2O) in the cell may also cause deterioration of the current collectors. Fig. 4-14 shows stability test curves of cell with plated Ni foam current collector discharging at 0.75 V and 800 ^{o}C for 24 h in either H_2 or humidified syngas. The respective power densities were ~750 mW cm^{-2} in H_2 and ~490 mW cm^{-2} in humidified syngas, and no apparent degradation was observed during each 24 h test. After test, no carbon deposits, structural damages or products of reaction with anode were observed by SEM on plated Ni foam. Thus Ni-P plated Ni foam current collectors have excellent stability during fuel cell operation under working conditions.
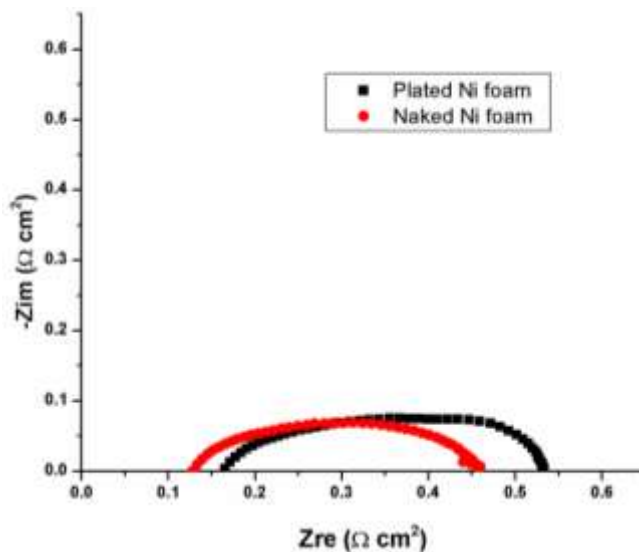
Figure 4-11 Comparison of electrochemical impedance spectra of SOFC with plated and naked Ni foam anode current collectors in H_2 at 800 ^{o}C.
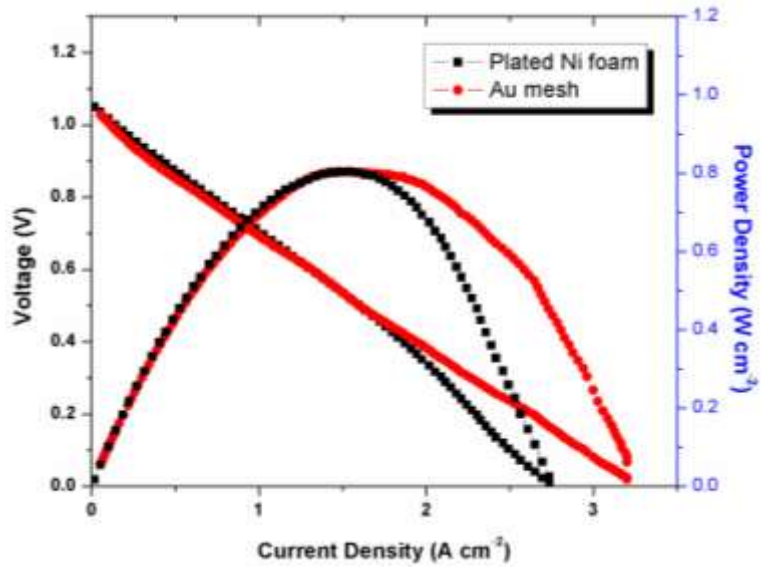
Figure 4-12 Comparison of current-voltage characteristics and power densities of SOFC with plated Ni foam and Au mesh current collectors in syngas at 800 °C.
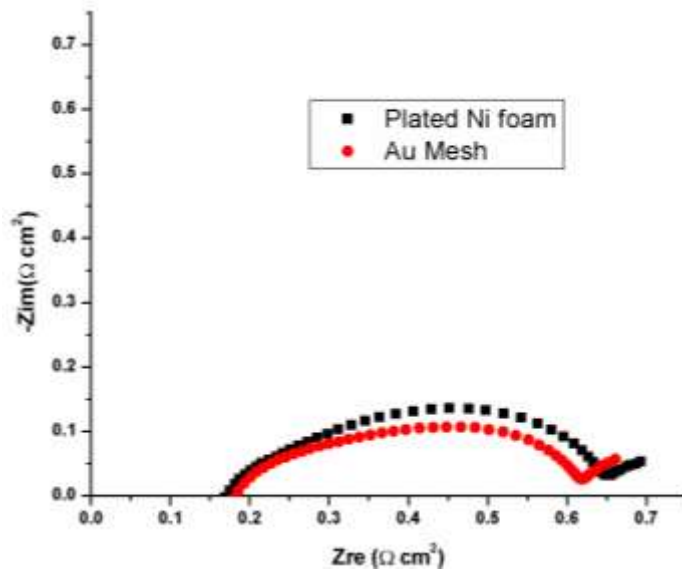
Figure 4-13 Comparison of electrochemical impedance spectra of SOFC with plated Ni foam and Au mesh as anode current collectors in syngas at 800°C.
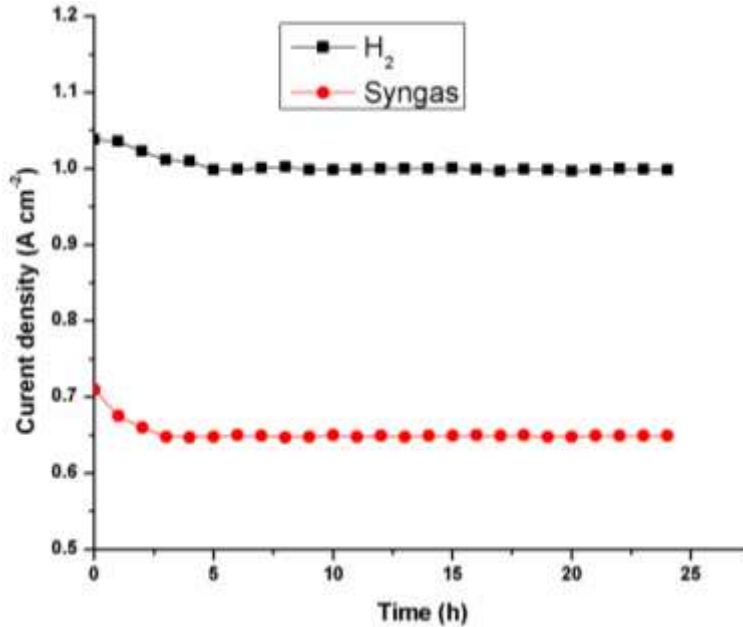
Figure 4-14 Stability of SOFC with plated Ni foam anode current collector in H_2 and syngas at 0.75V and 800 ^{o}C over 24 h.

4.4 Conclusions

Electroless plating of Ni-P onto Ni foam provides an easy, quick and inexpensive method to produce a highly uniform protective coating comprising mainly Ni and Ni_3P at SOFC working temperatures (> 600 ^{o}C). Plated Ni foams with coatings having P content higher than 6.4 wt% have much better coking resistance and structure stability in syngas at various temperatures (600 ~ 800 ^{o}C) than either naked Ni foam or the same foam coated with Ni-P with lower P content. SOFC for current collector test has a maximum power density exceeding 1.3 W cm^{-2} in H_2 at 850 ^{o}C and 0.8 W cm^{-2} in syngas at 800 ^{o}C. The SOFC

system with plated Ni foam anode current collector has performance as good as the one using naked Ni foam in pure H_2 and the one using Au mesh in syngas. They also exhibit high and stable power outputs during stability test using either H_2 or humidified syngas as fuels. Thus Ni-P plated Ni foam is a promising anode current collector in the syngas SOFC system.

References

[1] O. Costa-Nunes, R.J. Gorte, J.M. Vohs, *J. Power Sources*, 2005, **141**, 241-249.

[2] C.O. Colpan, I. Dincer, F. Hamdullahpur, *Int. J. Hydrog. Energy*, 2007, **32**, 787-795.

[3] R.J. Kee, H.Y. Zhu, A.M. Sukeshini, G.S. Jackson, *Combust. Sci. Technol.*, 2008, **180**, 1207-1244.

[4] R. Suwanwarangkul, E. Croiset, E. Entchev, S. Charojrochkul, M.D. Pritzker, M.W. Fowler, P.L. Douglas, S. Chewathanakup, H. Mahaudom, *J. Power Sources*, 2006, **161**, 308-322.

[5] J.W. Fergus, *Mater. Sci. Eng. A-Struct. Mater. Prop. Microstruct. Process.*, 2005, **397**, 271-283.

[6] Z. Zeng, K. Natesan, Metal dusting problem with metallic interconnects for solid oxide fuel cell, in: P. Knauth, J.M. Tarascon, E. Traversa, H.L. Tuller (Eds.) Solid State Ionics-2002, Materials Research Society, Warrendale, 2003, pp. 557-562.

[7] V. Alzate-Restrepo, J.M. Hill, *J. Power Sources*, 2010, **195**, 1344-1351.

[8] A. Schneider, H.J. Grabke, *Mater. Corros.*, 2003, **54**, 793-798.

[9] H.J. Grabke, E.M. Muller-Lorenz, *Mater. Corros.*, 1998, **49**, 317-320.

[10] X.Z. Fu, J. Melnik, Q.X. Low, J.L. Luo, K.T. Chuang, A.R. Sanger, Q.M. Yang, *Int. J. Hydrog. Energy*, 2010, **35**, 11180-11187.

[11] J. Dong, Z. Cheng, S.W. Zha, M.L. Liu, *J. Power Sources*, 2006, **156**, 461-465.

[12] H. Ashassi-Sorkhabi, S.H. Rafizadeh, *Surf. Coat. Technol.*, 2004, **176**, 318-326.

[13] C.D. Gu, J.S. Lian, G.Y. Li, L.Y. Niu, Z.H. Jiang, *J. Alloy. Compd.*, 2005, **391**, 104-109.

[14] F. Zhao, A.V. Virkar, *J. Power Sources*, 2005, **141**, 79-95.

[15] P. Von Dollen, S. Barnett, *J. Am. Ceram. Soc.*, 2005, **88**, 3361-3368.

[16] C.R. Xia, M.L. Liu, *J. Am. Ceram. Soc.*, 2001, **84**, 1903-1905.

[17] P.L. Walker, J.F. Rakszawski, G.R. Imperial, *J. Phys. Chem.*, 1959, **63**, 140-149.

[18] C.M. Chun, J.D. Mumford, T.A. Ramanarayanan, *J. Electrochem. Soc.*, 2000, **147**, 3680-3686.

[19] C.H. Rochester, R.J. Terrell, *J. Chem. Soc., Faraday Trans.*, 1977, **73**, 609-621.

[20] J.R. Rostrupnielsen, *J. Catal.*, 1984, **85**, 31-43.

[21] L. De Rogatis, T. Montini, A. Cognigni, L. Olivi, P. Fornasiero, *Catal. Today*, 2009, **145**, 176-185.

[22] S.P. Jiang, J.G. Love, L. Apateanu, *Solid State Ionics*, 2003, **160**, 15-26. .

Chapter 5 Effective Conversion of Sour Natural Gas (0.5% H_2S + CH_4) in Solid Oxide Fuel Cells using Pd-CeO$_2$/La$_{0.3}$Sr$_{0.7}$TiO$_{3+\delta}$ Anode

5.1 Introduction

Solid oxide fuel cell (SOFC) has been intensively studied over the last several decades as a promising power source. Utilizing the oxygen ionic conductor as the electrolyte, SOFC is able to convert a variety of fuels including various hydrocarbons to electricity [1-3]. Therefore, natural gas, one of the most economical and abundant fossil fuels becomes an ideal feedstock for SOFC [4-6]. The typical raw natural gas (sour gas), however, contains significant amount of H_2S; adding desulfurization and steam reforming components will greatly increase system complexity and cost. Therefore, SOFC anode catalyst has to be highly resistant to sulfur poisoning as well as carbon deposition in addition to offering the electro-catalytic activity towards fuel oxidation [7]. Thereby, the fuel compatibility of the commonly used Ni anode becomes a great challenge because it is prone to catalyze the formation of coke and suffer detrimental sulfur poisoning.

To address the requirements of the anode running in sour gas, great efforts have been devoted to the development of carbon and sulfur tolerant anode materials. A variety of materials including oxide and sulfide were studied as the anode candidates [3, 8-16]. During the investigations, it was found that the alternative anode catalysts such as $Cu-CeO_2$ and $La_{0.75}Sr_{0.25}Cr_{0.5}Mn_{0.5}O_{3-\delta}$ were able to resist adequately low concentration of H_2S (< 500 ppm) without suffering drastic performance loss [10-12]. However, once high concentration of H_2S (> 5000 ppm) was present in the feedstock, severe catalyst deactivation was observed, which was ascribed to the sulfidation of the anode candidates [11, 13]. On the other hand, although transition metal sulfides and doped $SrTiO_3$ exhibited excellent stability in the fuels with high concentration H_2S, their low activities hindered the effective conversion of sour gas in SOFC [12, 14-16].

In order to overcome the intrinsic limitations of low activity, an alternative strategy was adapted to have used those oxides only as electronic conductors, while the primary catalytic capability came from the sequentially infiltrated active secondary phases or exsoluted catalytic metal particles from the host oxide upon reduction [17-20]. SOFC equipped with these composite anodes demonstrated comparable performance with that using Ni-YSZ as anode in pure H_2 and CH_4. Herein, in an attempt to achieve an effective utilization of sour gas via SOFC, Pd-CeO_2 modified $La_{0.4}Sr_{0.6}TiO_3$ was developed and investigated as anode catalyst in SOFC fed with sour natural gas (0.5% H_2S + CH_4).

5.2 Experimental

The three-layer YSZ wafer was fabricated by Dr. Gorte's group in University of Pennsylvania using tape casting. Firstly, pure YSZ tape (white) and 50 wt % YSZ + 50 wt % graphite tape (black) were cut into designated area. Then, the two black layers serving as porous electrodes were laminated onto the white layer which was the electrolyte. Finally, the whole wafer was sintered at 1500 $^{\circ}$C for 4 h. After electrolyte densification, the thickness of electrode layer was ~ 50 μm with a porosity of ~ 60 % and the thickness of electrolyte was ~ 80μm. The following experiment was conducted in University of Alberta.

LST was prepared with aqueous solution containing stoichiometric amount of La(NO$_3$)$_3$·6H$_2$O, Sr(NO$_3$)$_2$ and [CH$_3$CH(O-)CO$_2$·NH$_4$]$_2$·Ti(OH)$_2$, using urea as the chelating agent. Initially, LST precursor was added into the porous YSZ electrode backbone through infiltration. After each infiltration, the wafer was heated to 500 $^{\circ}$C in order to burn off the metal salts and this process was repeated until ~ 45 wt % loading was obtained. The wafer was then calcined at 1100 $^{\circ}$C for 4 h to produce pure perovskite structure. Sequentially, the cathode catalyst La$_{0.8}$Sr$_{0.2}$FeO$_{3-\delta}$ (LSF) was infiltrated into the other porous electrode of the wafer using the same method with ~ 40 wt % loading, followed by calcination at 850 $^{\circ}$C for 4 h.

After the fabrication of the membrane electrode assembly (MEA) was completed, the investigated active phases (0.5 wt % Pd + 5 wt % CeO$_2$) were infiltrated into porous LST/YSZ anode using (NH$_3$)$_4$Pd(NO$_3$)$_2$ and Ce(NO$_3$)$_3$

aqueous solutions, respectively.

During fuel cell test, Au paste was used as both anode and cathode current collectors. The fuel to the anode was either humidified H_2, CH_4 or 0.5% H_2S + CH_4 with a flow rate of ~ 30 mL/min. The cathode side was exposed to the ambient air. The active area of cathode or anode was ~0.35 cm^2. The SOFC impedance spectra were obtained at open circuit with an AC perturbation of 5 mA and a frequency range between 0.003 Hz and 300 kHz.

5.3 Results and Discussions

5.3.1 Stability of Pd-CeO$_2$/ LST in sour gas

Fig. 5-1 shows the XRD patterns of the composite anode material after 0.5% H_2S + CH_4 treatment at 850 ^{o}C for 5 h. It was observed that pure LST was formed after 1100 ^{o}C calcination of the precursor and no LST sulfidation products, La_2S_3, SrS or TiO_2 were identified [21], indicating excellent sulfur resistance of LST in 0.5% H_2S + CH_4. Similar conclusions were also reported in previous work [12, 16]. In contrast, CeO_2 was partially sulfidized under the examined conditions and peaks corresponding to Ce_2O_2S were identified. Nevertheless, upon re-oxidation of the sulfidized sample, all Ce_2O_2S was subsequently transformed back to CeO_2, which suggested the potential of catalyst regeneration once H_2S was removed from the fuels.
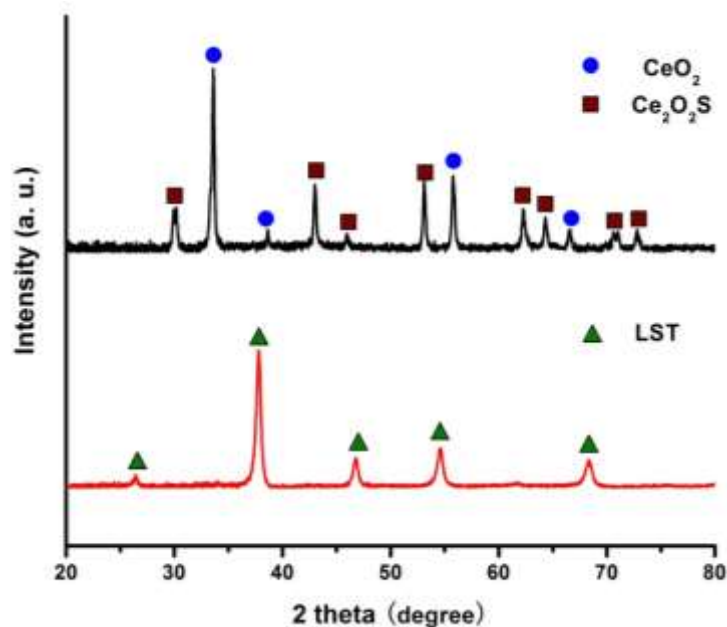
Figure 5-1 XRD patterns of CeO_2 and LST after 0.5% H_2S + CH_4 treatment at 850 ^oC for 5 h.

In fact, high temperature *in-situ* examination of Pd stability in sour gas required sophisticated apparatus [22], on the other hand, it was suspicious that palladium sulfide formed under high temperature was decomposed during cooling process. A similar scenario had misled the study of H_2S poisoning on Ni anode in SOFC [7]. This makes the results from the *ex-situ* determination questionable. Thus, thermodynamic calculations were more reliable to provide the accurate and necessary information in terms of Pd phase transformation in sour gas at various temperatures. In general, there were three possible reactions between Pd and H_2S as listed below:

$$Pd + 2H_2S(g) \rightarrow PdS_2 + 2H_2(g) \qquad \Delta_r G_m(800\,^oC) = 52.41 \; kJ \; mol^{-1} \qquad \text{(5-1)}$$

$$Pd + H_2S(g) \rightarrow PdS + H_2(g) \qquad \Delta_r G_m(800\,^oC) = 2.07 \; kJ \; mol^{-1} \qquad \text{(5-2)}$$

$$4Pd + H_2S(g) \rightarrow Pd_4S + H_2(g) \qquad \Delta_r G_m(800\,^oC) = -5.71 \; kJ \; mol^{-1} \qquad \text{(5-3)}$$
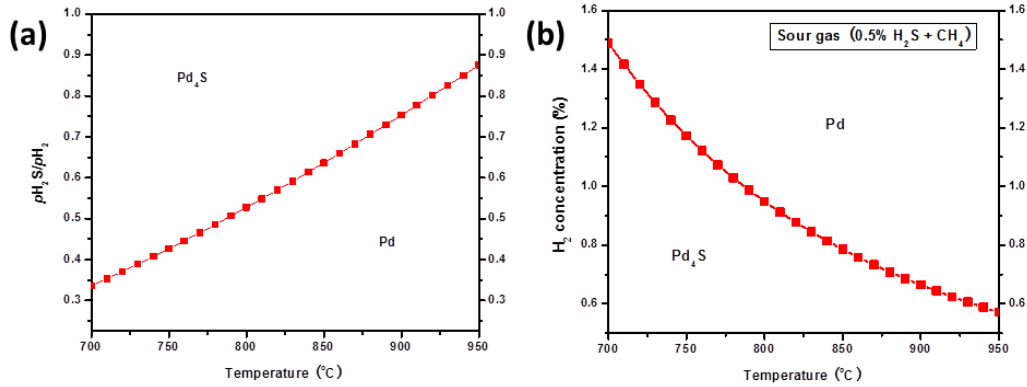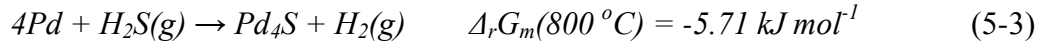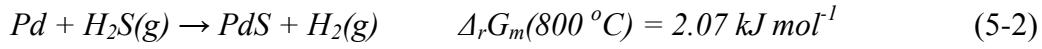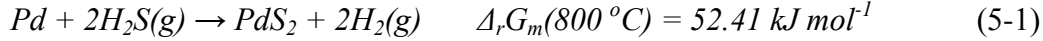
Figure 5-2 Pd-Pd$_4$S phase diagram calculated in (a) H$_2$-H$_2$S, (b) CH$_4$-H$_2$S gas mixture at temperature between 700 ^{o}C and 900 ^{o}C.

From the comparison of the change of Gibbs free energy within the temperature range of SOFC operation, only reaction (3) was thermodynamically more favorable and needed to be considered when investigating Pd chemical stability. Fig. 5-2 shows the phase diagram of Pd-S system calculated using HSC Chemistry 5.0 software. In H$_2$-H$_2$S environment at 850 ^{o}C which was a typical SOFC operation temperature, metallic Pd remained stable when pH_2S/pH_2 was below ~64 % corresponding to a composition of ~39 % H$_2$S balanced by H$_2$. In sour gas (5000 ppm H$_2$S + CH$_4$), although the absolute H$_2$S concentration was far below the previously calculated Pd sulfidation limit in H$_2$-H$_2$S system, its

pH$_2$S/pH$_2$ was significantly higher since initially, H$_2$ was not presented in the gas mixture. Therefore, in order to stabilize Pd in sour gas, the required minimum H$_2$ concentration was determined as a function of temperature showed in Fig. 5-2b. It can be observed that a minimum of ~0.79 % H$_2$ was required to chemically stabilize Pd at 850 ^{o}C.

Table 5-1. Typical composition of humidified sour gas at 850 ^{o}C.

Gas	H$_2$	CO	CO$_2$	H$_2$S	H$_2$O	N$_2$	CH$_4$
Composition (%)	6.8	< 2	< 2	ND	ND	trace	88.5

ND: Not Determined

Table 5-1 reveals a typical composition of the humidified sour gas at 850 ^{o}C in anode chamber of SOFC based on LST catalyst. At high temperature, H$_2$ could be produced in sour gas via catalyzed methane steam reforming/thermal cracking, or the thermal decomposition of H$_2$S. The concentration of the small amount of H$_2$ in sour gas was usually between 5 % to 10 %, which was adequately high to suppress the Pd sulfidation since pH$_2$S/pH$_2$ could be kept below the tolerance limit according to Fig. 5-2b. Therefore, it could be concluded that metallic Pd was chemically stable in sour gas without being sulfidized, which was in accordance with the results of the XPS analysis.

5.3.2 Button cell characterization and performance

Fig. 5-3 shows the SEM images of the electrode microstructure. For the purpose of obtaining a better observation of the infiltrated Pd-CeO$_2$ without the distraction of high loading of LST, only Pd-CeO$_2$ was impregnated into the porous YSZ matrix at first. After heat treatment, the Pd nanoparticles were agglomerated preferentially along YSZ grain boundaries where surface energies were lower. The diameters of those nanoparticles were approximately between 20nm and 50 nm. It was also expected that Pd might tend to partially segregate along the triple- phase
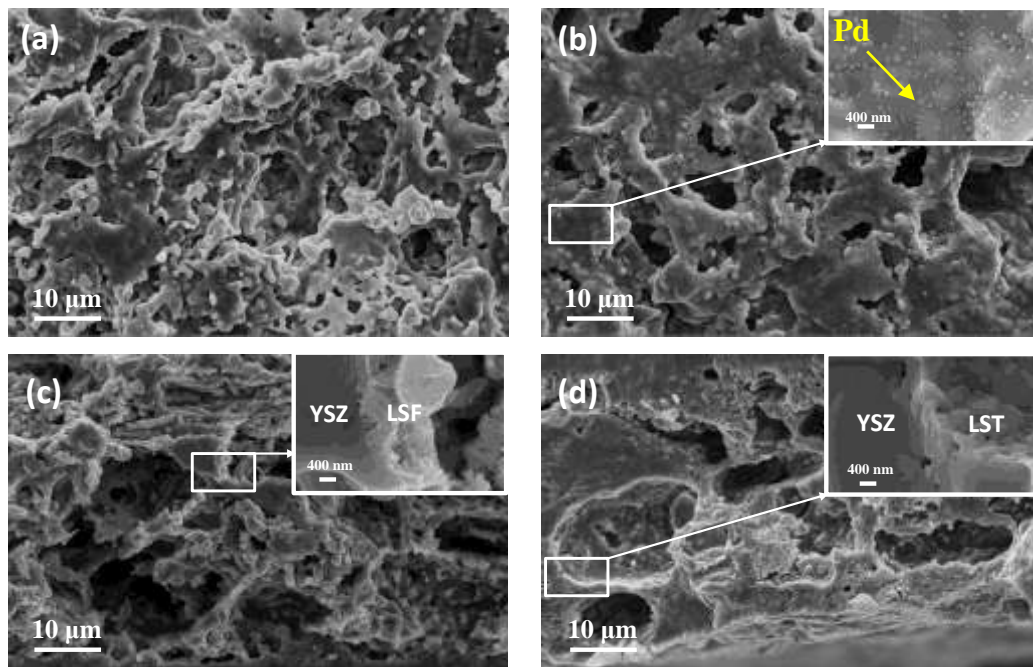
Figure 5-3 SEM images of the microstructure of (a) porous YSZ anode matrix; (b) Pd-CeO$_2$ infiltrated YSZ anode; (c) LSF infiltrated YSZ anode and (d) LST infiltrated YSZ anode after 10 h calcination at 850 $^\circ$C.

boundary (TPB) where YSZ and LST met with each other. Thereby, both the catalyst activity and the length of the TPB were effectively maximized. Figs. 5-3c and 5-3d exhibit the microstructure of YSZ matrix with LSF and LST loadings, respectively. The contiguous LSF and LST phases were deposited onto YSZ surface and served as cathode catalyst and anode electronic conductor, respectively. Fig. 5-4a exhibited the cross-sectional image of the MEA after infiltration of the specific materials in the electrodes. The final Pd-CeO$_2$/LST infiltrated YSZ anode is showed in Fig. 5-4b and Fig. 5-5.
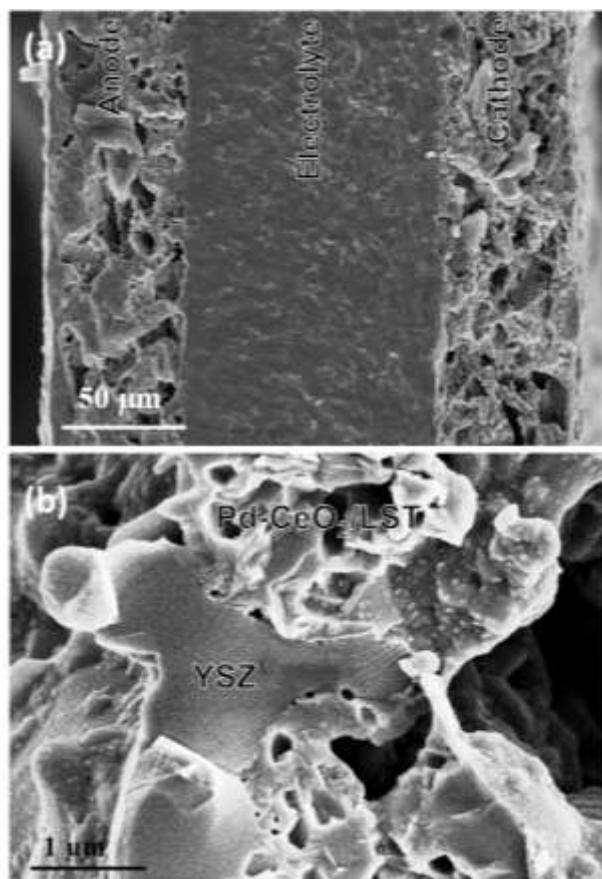
Figure 5-4 SEM images of the cross-section of (a) button cell, (b) Pd-CeO$_2$/LST infiltrated YSZ matrix after 10 h calcination at 850 ^{o}C.

Agglomerated Pd nanoparticles were visibly deposited on both YSZ and LST phases. The EDS mapping data in Fig. 5-5 also indicated that Pd particles were segregated to form bigger clusters in certain area whereas CeO_2 was essentially sustained the homogeneity on LST/YSZ surface after heat treatment.
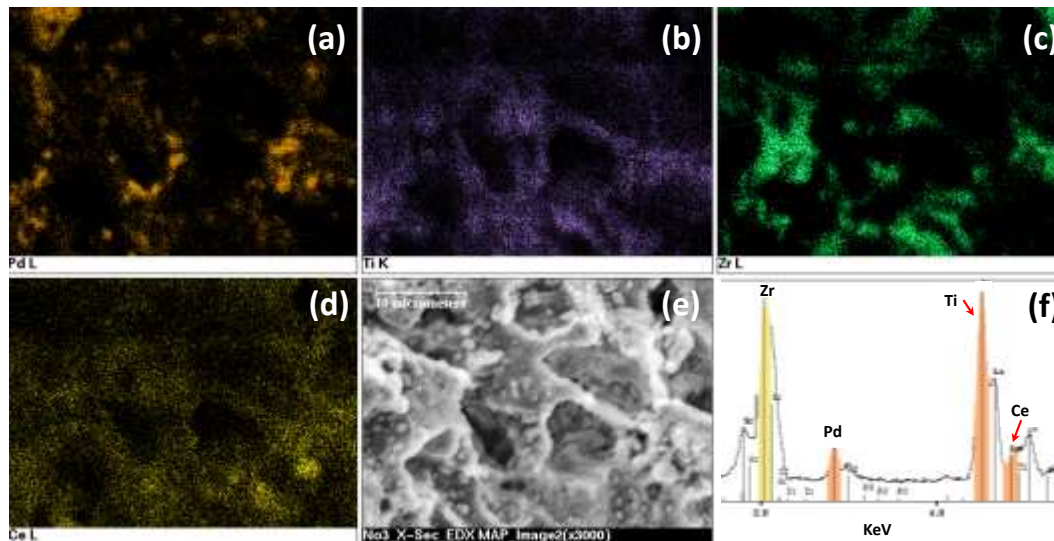
Figure 5-5 EDX elemental mappings and spectrum of LST-CeO_2/LST anode microstructure after 10 h calcination at 850 ^{o}C. (a) Pd-, (b) Ti-, (c) Zr-, (d) Ce-mapping, (e) SEM image and (f) the overview of the detected elements spectrum.

Fig. 5-6 presents a typical cell performance in H_2, the maximum power densities reached 195 mW cm^{-2}, 315 mW cm^{-2}, 507mW cm^{-2} and 642 mW cm^{-2} at 700 ^{o}C, 750 ^{o}C, 800 ^{o}C and 850 ^{o}C, respectively. It was notable that when the temperature was increased from 800 ^{o}C to 850 ^{o}C, an increase in maximum power density was not as apparent as that when temperature increased from 750 ^{o}C to 800 ^{o}C. This was likely to be ascribed to the Pd nanoparticles agglomeration upon

prolonged exposure to the high temperature environment. At 850 $^{\circ}$C, the total polarization resistance of the cell was 0.71 Ω cm^2 consisted of 0.17 Ω cm^2 ohmic and 0.59 Ω cm^2 non-ohmic resistance (Fig. 5-7), which was comparable with the literature [23].
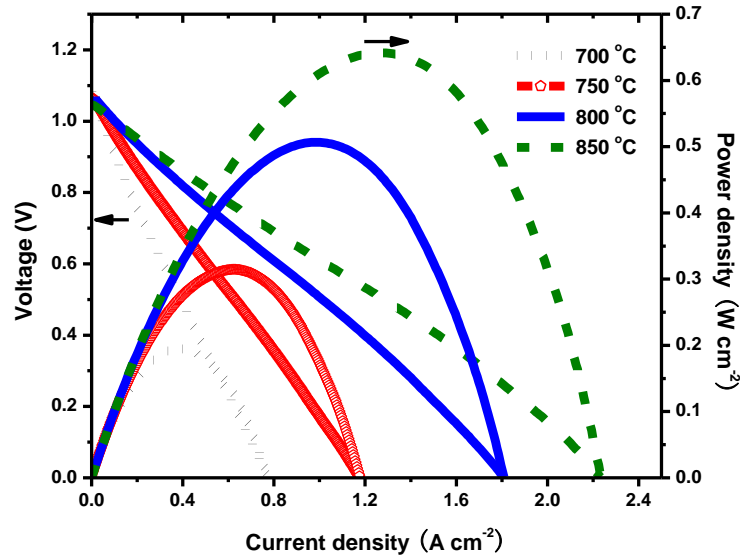
Figure 5-6 I-V and power density curves of button cells using Pd-CeO$_2$ infiltrated LST anode at different temperatures in humidified H$_2$.
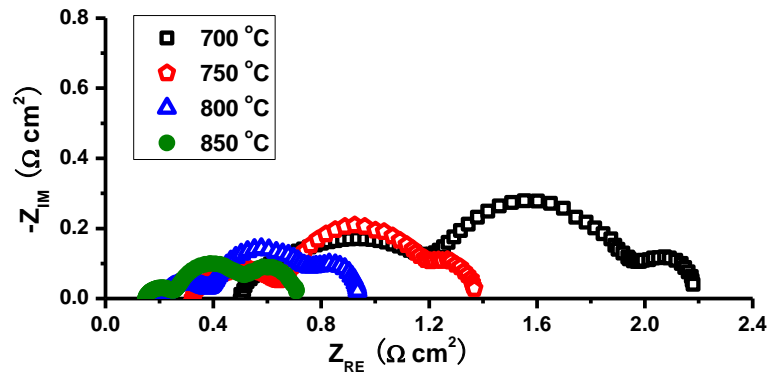
Figure 5-7 Impedance spectra of button cells using Pd-CeO$_2$ infiltrated LST anode at different temperatures in humidified H$_2$.

5.3.3 Button cell performance in sour natural gas

In order to evaluate the activity and sulfur resistivity of the anode materials under investigation, the SOFC button cells were tested in both humidified CH_4 and 0.5% $H_2S + CH_4$. Fig. 5-8 demonstrates the I-V and power density characters of the SOFC with LST infiltrated anode. The LST anode exhibited a negligible catalytic activity toward CH_4 oxidation, with which the SOFC reached a maximum power density of 6.5 mW cm^{-2}. Although the addition of H_2S into the anode feed enhanced the performance drastically in accordance with other reports [12, 16], the maximum power density was only 67 mW cm^{-2}, which was still unsatisfactory in terms of pursuing effective conversion of CH_4 in SOFC. During the impedance spectra analysis, the low frequency was terminated at 0.1 Hz for the test in both fuels due to the inability to collect stable points below this frequency. It was not surprised to observe that the radius of the semi-circle for 0.5% $H_2S + CH_4$ fuelled SOFC was considerably smaller than the other one. This suggested that LST had a better activity for sour natural gas conversion, or possibly indicated that the presence of H_2S might promote CH_4 electrochemical oxidation via a synergic effect with LST.

After the impregnation of Pd-CeO$_2$ into LST anode, the performances of fuel cells increased significantly; maximum power densities reached to 288 mW cm^{-2} in humidified CH_4 and 274 mW cm^{-2} in 0.5% $H_2S + CH_4$. The performance in sour natural gas was drastically improved in comparison with the literature [16]. In potentiodynamic scan, the scanning was stopped at 0.4 V since the current was

starting to decrease when the voltage was at about 0.5 V. It was noticed that in Pd-

CeO$_2$/LST cells, the H$_2$S enhancement effect did not play an important role in
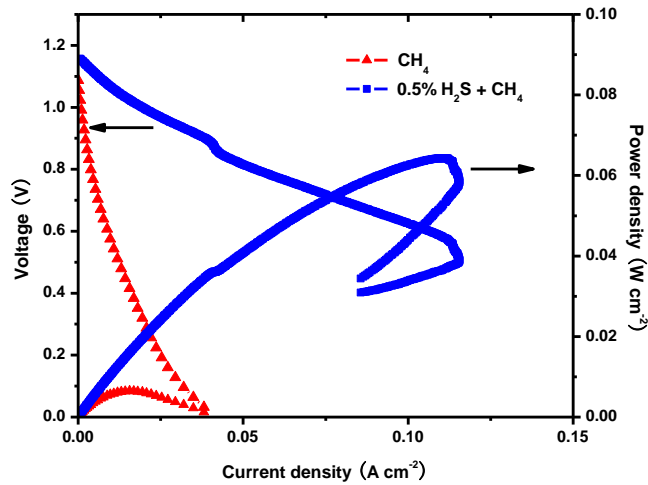
Figure 5-8 I-V and power density curves of button cells using LST infiltrated anode in either humidified CH$_4$ or 0.5% H$_2$S + CH$_4$ at 850 ^{o}C.
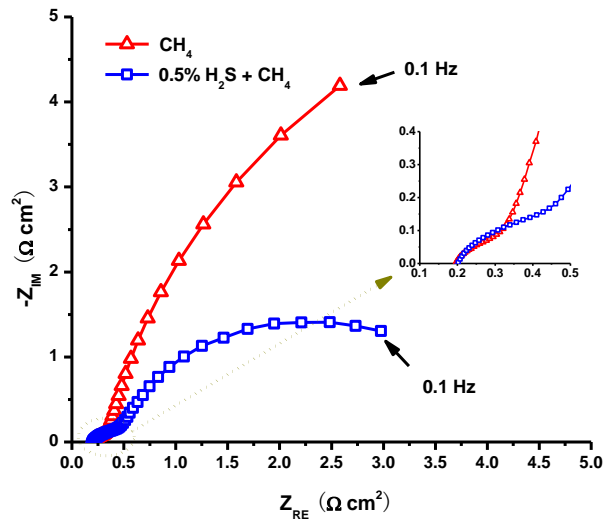
Figure 5-9 Impedance spectra of button cells using LST infiltrated anode in either humidified CH$_4$ or 0.5% H$_2$S + CH$_4$ at 850 ^{o}C.

improving the power output; the fuel cells performance was eventually reduced slightly instead. The impedance spectra in Fig. 5-11 reveal that the uniformly distributed Pd-CeO$_2$ particles contributed dramatically to the non-ohmic polarization resistance drop. Nonetheless, the introduction of H$_2$S into the pure CH$_4$ did not further decrease the resistance. On the contrary, it increased the resistance from 1.4Ω cm^2 to more than 2.8 Ω cm^2. Presumably, the positive effect of H$_2$S enhancement was far less significant to completely compensate the negative impact of catalyst deactivation. The partial sulfidation of CeO$_2$ to Ce$_2$O$_2$S confirmed through XRD was attributable to the degradation of catalyst activity. Meanwhile, the chemisorbed S and its compounds on Pd surface were able to massively block the active sites. This poisoning effect was believed to be the other reason for the SOFC performance loss.

In fact, among most of the transition metals, Pd owns both excellent low sulfur sensitivity and high activity. Firstly, relative to Ni and Co catalyst, the calculated results shown in Fig. 5-2 suggested that Pd could tolerate higher concentration of H$_2$S without forming metal sulfides which were detrimental to the catalyst activity and structural stability [24]. Secondly, Pd was able to maintain sufficiently high activity while partially poisoned by H$_2$S. Studies have correlated this property with its face-centered cubic (FCC) structure [25, 26]. Lastly, according to the examination through computational calculation, Pd had a significantly lower sulfur adsorption energy compared with other investigated metallic candidates. Thus, Pd was anticipated to be more resistant to H$_2$S

poisoning. In summary of the three points discussed above and the H_2S enhancement effect offering extra performance improvement, it was not abnormal to observe a high power output in sour gas fed SOFC.
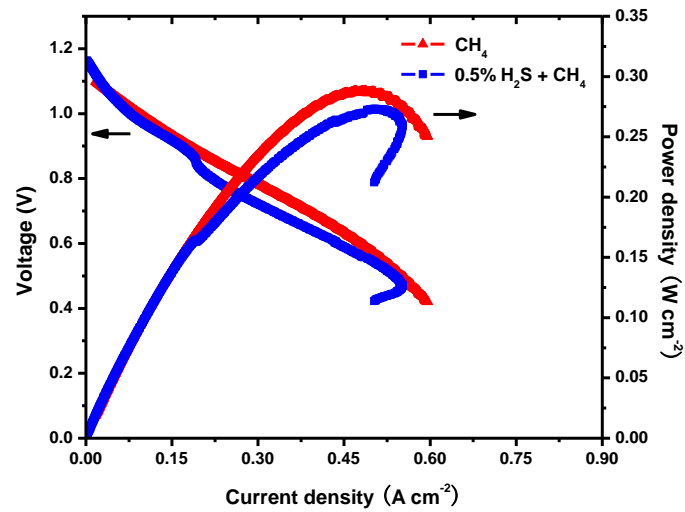
Figure 5-10 I-V and power density curves of button cells using Pd-CeO$_2$ infiltrated LST anode in either humidified CH$_4$ or 0.5% H$_2$S + CH$_4$ at 850 ^{o}C.
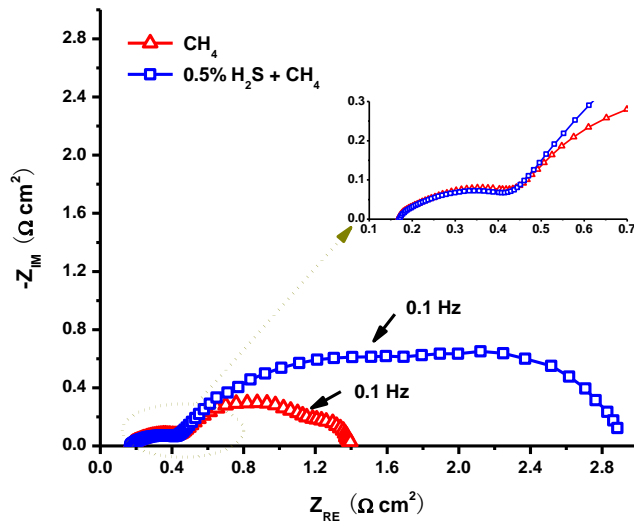
Figure 5-11 Impedance spectra of button cells using Pd-CeO$_2$ infiltrated LST anode at different temperatures in either humidified CH$_4$ or 0.5% H$_2$S + CH$_4$.

5.4 Conclusions

SOFC using Pd-CeO$_2$/LST anode was fabricated via infiltration and exhibited good performance in both desulfurized fuels and sour natural gas. The experimental characterization combined with a Pd-Pd$_4$S phase diagram study confirmed the high stability and sulfur resistance of Pd in 0.5 H$_2$S + CH$_4$, which was attributable to the enhancement effectiveness of sour natural gas conversion.

Although Pd-CeO$_2$/LST composite exhibited the promising potential as a high performance sulfur tolerant anode candidate, it was still a concern that the well-dispersed Pd nanoparticles might suffer thermal stability issues in longevity test at 850 ^{o}C. Future structural optimization via Pd@CeO$_2$ core-shell cluster may be the next step towards preventing the deteriorate agglomeration of Pd [27].

References

[1] S. Park, J. M. Vohs and R. J. Gorte, *Nature*, 2000, **404**, 265-267.

[2] A. Atkinson, S. Barnett, R. J. Gorte, J. T. S. Irvine, A. J. Mcevoy, M. Mogensen, S. C. Singhal and J. Vohs, *Nat. Mater.*, 2004, **3**, 17-27.

[3] S. W. Tao, J. T. S. Irvine, *Nat. Mater.*, 2003, **2**, 320-323.

[4] J. Weissbart and R. Ruka, *J. Electrochem. Soc.*, 1962, **109**, 723-726.

[5] J. Laurencin, F. Lefebvre-Joud, G. Delette, *J. Power Sources*, **2008**, 177, 355-368.

[6] T. Suzuki, T. Yamaguchi, K. Hamamoto, Y. Fujishiro, M. Awanoand N. Sammes, *Energy Environ. Sci.*, 2011, **4**, 940-943.

[7] Z. Cheng, J. H. Wang, Y. M. Choi, L. Yang, M. C. Lin and M. L. Liu, *Energy Environ. Sci.*, 2011, **4**, 4380-4409.

[8] D. P. Fagg, V. V. Kharton, A. V. Kovalevsky, A. P. Viskup, E. N. Naumovich, J. R. Frade, *J. Eur. Ceram. Soc.*, 2001, **21**, 1831-1835.

[9] J. B. Goodenough, Y. H. Huang, *J. Power Sources*, 2007, **173**, 1-10.

[10] H. Kim, J. M. Vohs, R. J. Gorte, *Chem. Commun.*, 2001, **22**, 2334-2335.

[11] H. P. He, R. J. Gorte, J. M. Vohs, *Electrochem. Solid-State Lett.*, 2005, **8**, A279-A280.

[12] R. Mukundan, E. L. Brosha, F. H. Garzon, *Electrochem. Solid State Lett.*, 2004, **7**, A5-A7

[13] X. J. Chen, Q. L. Liu, S. H. Chan, N. P. Brandon, K. A. Khor, *J. Electrochem. Soc.*, 2007, **154**, B1206-B1210.

[14] M. Liu, G. Wei, J. L. Luo, A. R. Sanger and K. T. Chuang, *J. Electrochem. Soc.*, 2003, **150**, A1025-A1029.

[15] C. Yates, J. Winnick, *J. Electrochem. Soc.*, 1999, **146**, 2841-2844.

[16] A. L. Vincent, J. L. Luo, K. T. Chuang, A. R. Sanger, *Appl. Catal. B-Environ.,* 2011, **106,** 114-122.

[17] S. Lee, G. Kim, J. M. Vohs and R. J. Gorte, *J. Electrochem. Soc.*, 2008, **155**, B1179–B1183.

[18] S. P. Jiang, *Mater. Sci. Eng. A-Struct. Mater. Prop. Microstruct. Process.*, 2006, **418**, 199-210.

[19] W. Kobsiriphat, B. D. Madsen, Y. Wang, L. D. Marks and S. A. Barnett, *Solid State Ionics*, 2009, **180**, 257-264.

[20] L. Adijanto, V. B. Padmanabhan, R. Kungas, . J. Gorte and J. M. Vohs, *J. Mater. Chem.*, 2012, 22, 11396-11402.

[21] Z. Cheng, S. W. Zha and M. L. Liu, *J. Electrochem. Soc.*, 2006, **153**, A1302-A1309.

[22] Z. Cheng, H. Abernathy and M. Liu, *J. Phys. Chem. C*, 2007, **111**, 17997-18000.

[23] S. W. Lee, G. Kim, J. M. Vohs and R. J. Gorte, *J. Electrochem. Soc.*, 2008, **155**, B1179-B1183.

[24] T. Rosenqvist, *J. Iron Steel Inst.*, London, 1954, **176**, 37-57.

[25] T. P. Radhakrishnan, L.L. Scheir, *Electrochim. Acta*, 1966, **11**, 1007-1021.

[26] B. D. Morreale, M. V. Ciocco, B. H. Howard, R. P. Killmeyer, A. V. Cugini and R. M. Enick, *J. Membr. Sci.*, 2004, **241**, 219-224.

[27] J. K. Kim, N. L. Wieder, A. J. Abraham, M. Cargnello, P. Fornasiero, R. J. Gorte, and J. M. Vohs. *J. Electrochem. Soc.*, 2011, **158**, B596-B600.

Chapter 6 Co-generation of Electricity and CO from Syngas via Proton-conducting Solid Oxide Fuel Cells

6.1 Introduction

Fossil resources are the main energy sources at present and for the foreseeable future [1]. These resources are nonrenewable and the worldwide growing energy demand cannot be met by renewable energies in the medium term [2]. Hence it is urgent and important to utilize fossil fuels in much cleaner and more efficient ways. Solid oxide fuel cells (SOFC) can directly convert readily available feedstock such as syngas ($CO + H_2$) into power with significantly higher energy conversion efficiency and lower environmental impact compared to current combustion power plants [3-5], thus it is believed to be a promising candidate method for future power generation.

In addition to the role as a fuel, syngas and its main constituents, namely H_2 and CO are also crucial raw materials for the production of various organic chemicals [6]. However, syngas is completely oxidized into H_2O and CO_2 in conventional SOFCs with oxygen ionic electrolyte, in which greenhouse gas CO_2

is inevitably generated, resulting in increasingly serious environmental problem. In this work, proton conducting SOFCs were proposed to use for the co-production electricity and CO from syngas. The highly concentrated CO feedstock can significantly reduce the cost of the downstream CO purification process. At the same time, instead of consuming energy during CO concentration, reasonable amount of electricity can be co-generated.

6.2 Experimental

Here $BaCe_{0.7}Zr_{0.1}Y_{0.2}O_{3-\delta}$ (BZCY) was used as proton conducting electrolyte material since it was reported as having a good balance between protonic conductivity and stability [7]. During fuel cell test, Ag paste was used as the cathode current collector whereas Au paste as the anode counterpart. 10% H_2 (balanced with Ar) was fed via the anode feed tube to reduce the NiO anode into Ni. After the furnace reached the stable temperature for fuel cell test, 10% H_2 was replaced by pure H_2 as anode feed and oxygen was fed to the cathode as oxidant. Certified composition of gas mixtures were used as the feedstock of the fuel cell reactor. The flow rates of fuels and oxidant were adjusted using mass flow controller.

6.3 Results and Discussions

6.3.1 Characterization of materials and fuel cell reactors characteristics

The XRD patterns confirmed that both calcined BZCY and BPC powders were pure perovskite and double perovskite oxides, respectively. No impurity peaks were identified. The cross-sectional SEM image of the cell after operation in Fig. 6-1 showed that the thin film electrolyte was fully densified with the thickness of approximately 20 μm, the anode functional layer adjacent to the anode substrate was about 25 μm thick. In fuel cell test, The OCV of the proton conducting SOFCs was more than 1.1V at 600 ^{o}C, confirming that the BZCY thin film electrolyte was sufficiently dense to block gases crossover between the two electrodes. The SOFCs provided high power density from 383 to 548 mW.cm^{-2} as the operating temperature increased from 600 ^{o}C to 700 ^{o}C. Therefore, the high performance SOFCs can serve as an effective reactor for the conversion of H_2 and the concentration of CO from syngas.
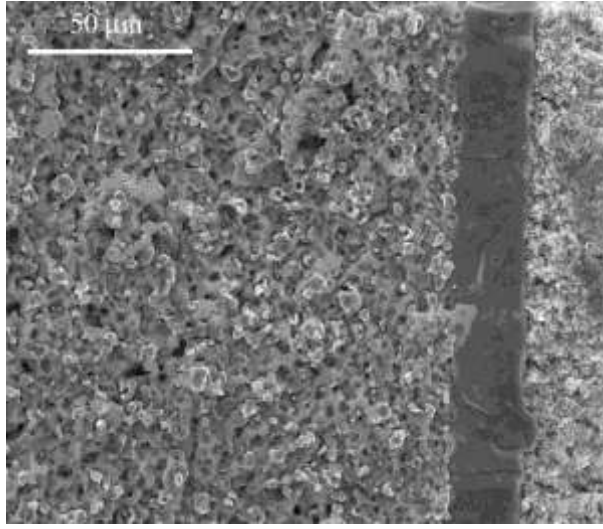
Figure 6-1 Cross-sectional SEM images of anode supported SOFCs with anode, electrolyte and cathode from the left to the right after test in syngas.
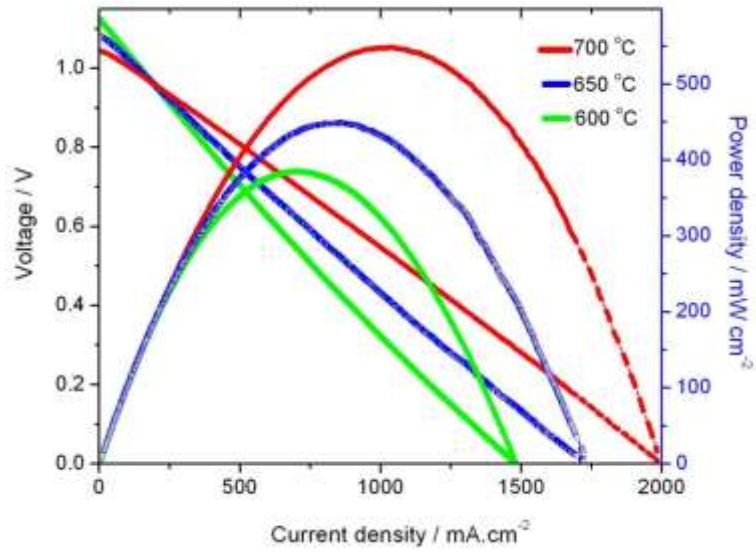
Figure 6-2 I-V curves and power density profiles of SOFC fed by H_2 at different temperatures.

6.3.2 CO concentration using proton-conducting SOFC

The operating principle of SOFC for co-generation of CO and electricity from syngas is described in Fig. 6-3. At elevated temperature, both CO and H_2 in syngas were readily activated by the anode catalyst. However, only H_2 could be selectively and effectively driven to move across the proton conducting electrolyte and oxidized at the cathode side. Depending on the degree of H_2 conversion, theoretically, the CO concentration in the anode effluent can be up to 100% when H_2 utilization in SOFC reached 100 %.
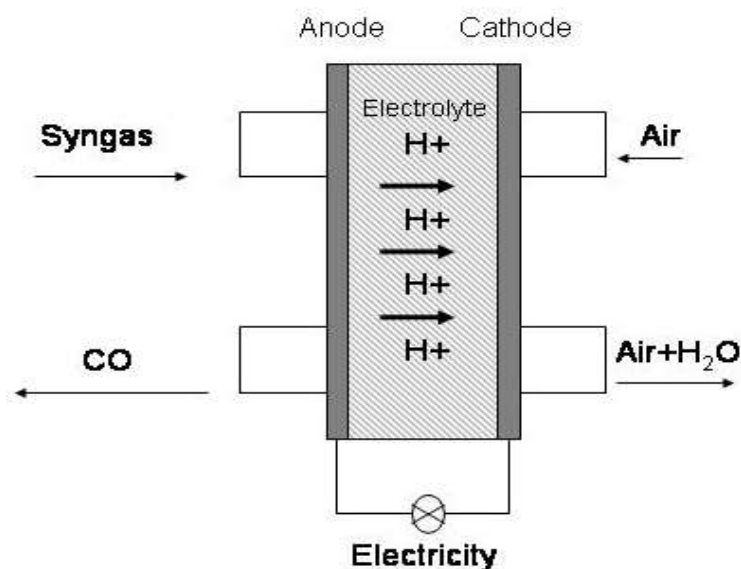
Figure 6-3 Schematic of proton conducting SOFCs for co-generation of CO and electricity from syngas.

The maximum power density decreased comparing to pure H_2 when the fuel was diluted with either CO or N_2 as shown in Fig. 6-4. Generally, the overrall fuel

cell performances in 20% CO-containing H_2 or 20% N_2-containing H_2 were essentially identical at 700 $^{\circ}C$, implying that only H_2 was electrochemically converted. The maximum power density in syngas was slightly lower than that diluted with N_2. From impedance spectra obtained under the same condition, it could be observed that the polarization resistance in syngas cell was higher, suggesting slower electrode reaction rate at the anode triple-phase boundaries (TPB). The lower ohmic resistance could be ascribed to the deposition of carbon which decreased the contact resistance between the cell and the current collector. Nevertheless, the existance of CO in the fuel did not undermine the performance of proton conducting SOFC significantly and a reasonable power output was maintained in syngas. The basic electrochemcial test results looked promising for the role of SOFC in co-generation of CO and electricity from syngas.

In consideration of the power output and fuel conversion limitation of a single button cell, syngas was diluted with He during CO concentration effect measurement. When fuel cell was operating under galvanostatic mode with different discharging current, GC was used to analyze the composition change of anode exhaust gas. H_2 and CO content variations were obtained by measuring the composition before and after discharging. Fig. 6-6 shows that the H_2 content decreased obviously whereas CO content increased with current. When the current density of the cell was 400 mA cm^{-2}, 23.4 % of H_2 was consumed in the stream and CO concentration increased 6.8 %, which confirmed that H_2 was selectively converted while CO was enriched. Hence, it was expected that a cell

91

test setup with high fuel utilization could concentrate CO considerably from syngas.
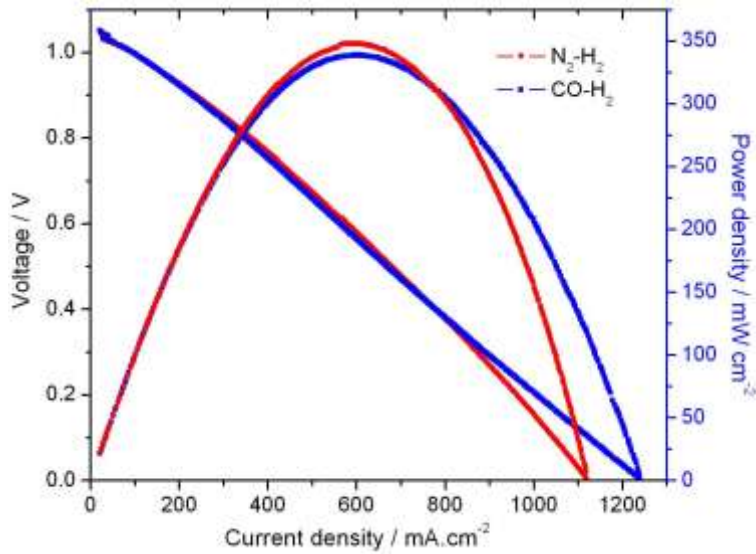
Figure 6-4 I-V and power density curves of SOFCs fed by either 100 mL min^{-1} 20% CO-containing H_2 or 100 mL min^{-1} 20% N_2-containing H_2 at 700 ^{o}C.
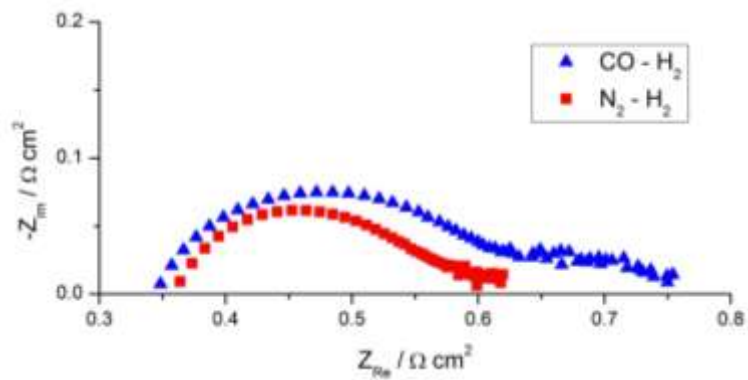
Figure 6-5 Impedance spectra of SOFCs fed by either 20% CO-containing H_2 or 20% N_2-containing H_2 at 700 ^{o}C.
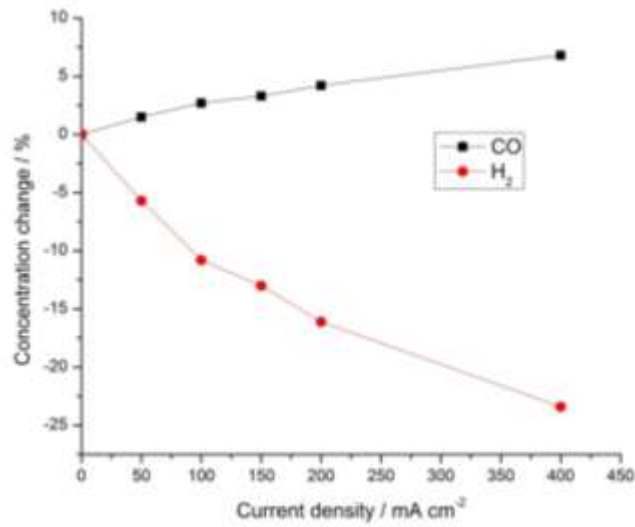
Figure 6-6 Effect of discharging current on the H_2 and CO content change in the anode effluent of SOFCs fed by dilute syngas (20% H_2 + 30% CO + 50% He) at different discharging currents at 700 ^{o}C.
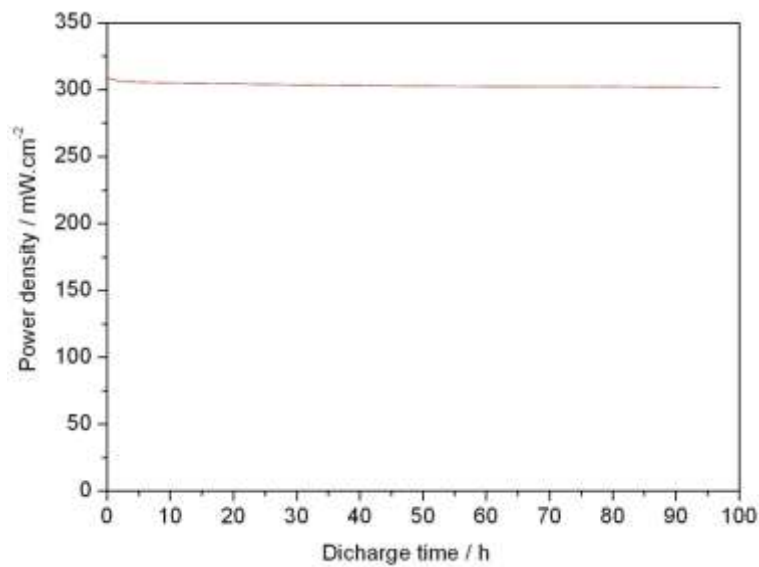
Figure 6-7 Stability test of SOFCs fed by H_2 at 0.75 V at 700 ^{o}C.

In fact, when fuel cell was operating with a 400 mA cm^{-2} current density, the voltage dropped to below 0.5V, which was not suitable for longevity test. During the study of temperature influence over CO enrichment, the current was set to 200 mA cm^{-2} to ensure that the voltage was above 0.7 V. Table I demonstrates the compositional change of diluted syngas (20% H_2 + 30% CO + 50% He) after passing through high temperature anode chamber of a stand-by SOFCs. Since no electrochemical reaction happened in the fuel cells, the interactions occurred among gaseous species were completely chemical. No CO_2 was detected, but it was observed that both the contents of CO and H_2 in the stream were lower than the original, which was mainly attributable to the methanation process [8]:

$$3H_2 + CO \rightarrow CH_4 + H_2O \qquad\qquad (6\text{-}1)$$

This reaction is exothermic and was suppressed when increasing the temperature. At 750 ^{o}C, only trace amount of CH_4 was found to exist and measured. Accordingly, it was advised that the fuel cell reactor need to work above 700 ^{o}C in order to minimize the CH_4 impurity in the concentrated CO.

The syngas composition changed once current was applied to the cell as described in Table II. While H_2 concentration increase was accompanied by CO decrease, CO_2 was not detected in the anode effluent after electrochemical conversion below 700 ^{o}C, which confirmed that CO was unable to be oxidized either chemically or electrochemically. When the fuel cell working temperature increased to 750 ^{o}C, although the H_2 concentration dropped from 18.8% to 16.2%, CO concentration remained at 28.5%, same as that before cell operation.

94

Meanwhile, CO_2 peak started to emerge in the GC spectra. The explanation of CO oxidation was that at 750 ^{o}C, BZCY electrolyte was not pure proton conductor, the oxygen ions movement began to contribute to the total ionic conductivity [9]. Therefore, the activated CO molecules were slowly oxidized by oxygen ions in the anode chamber.

Table 6-1 Diluted syngas compositions in the anode effluent before cell operation.

Gas Species	Ratio at 650 ^{o}C (%)	Ratio at 700 ^{o}C	Ratio at 750 ^{o}C
CO	21.9	25.0	28.5
H_2	12.4	16.9	18.8
CO_2	N/A*	N/A	N/A
CH_4	6.1	2.3	Trace

Table 6-2 Diluted syngas compositions in the operating cell anode effluent **

Gas Species	Ratio at 650 ^{o}C (%)	Ratio at 700 ^{o}C	Ratio at 750 ^{o}C
CO	23.1	26.3	28.5
H_2	10. 6	14.4	16.2
CO_2	N/A	N/A	Trace
CH_4	4.8	1.8	Trace

* "N/A" represents no peak was identified in the GC spectra

**Data obtained when fuel cells were discharging at 200 mA cm^{-2}.

6.3.3 Catalyst regeneration

Although the anode supported proton conducting SOFCs exhibited excellent stability during 96 h test in H_2 as shown in Figure 6-7, the maximum power density dropped rapidly from 225 mW cm^{-2} to 187 mW cm^{-2} within 4 h test in 20% H_2 + 30% CO + 50% He. Actually, Ni catalyst was well-known for its high activity toward H_2 oxidation, one of the biggest drawbacks associated with it was carbon deposition. The addition of water into the anode feed can suppress the coking [10]; however, the coexistence of water gas shift reaction (WGSR) reduced CO concentration and increased H_2 content which is not desirable in the present investigation.

$$H_2O + CO \rightarrow H_2 + CO_2 \tag{6-2}$$

Herein, a catalyst regeneration process was designed via exposing the partially deactivated cell to 3% H_2O-containing H_2 and simultaneously increasing the furnace temperature to 750 ^{o}C. After 16 h carbon removal (Fig. 6-8), the maximum power density was restored back to 218 mW cm^{-2} which was very close to the original performance. During two cycles of catalyst regeneration, the fuel cell performance was essentially fully recoverable. Nonetheless, after each one of the regeneration cycle, the power density dropped and the performance degradation rate in syngas became slightly higher.
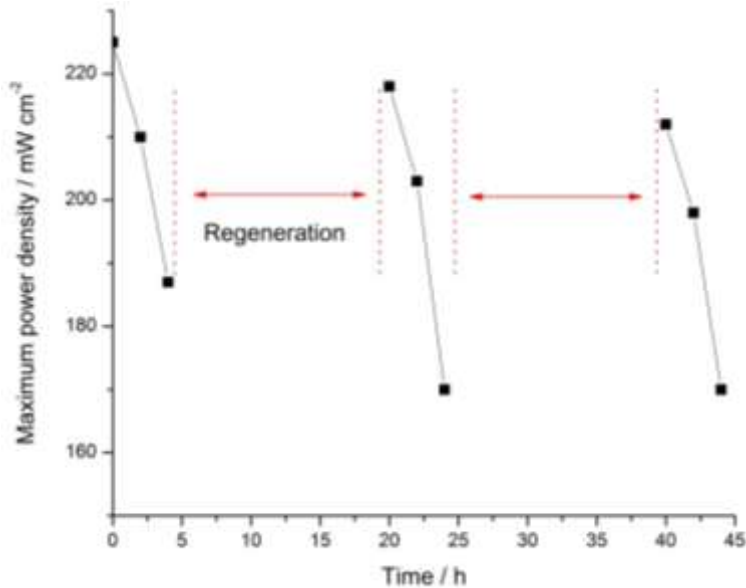
Figure 6-8 Anode catalyst regeneration in humidified H_2 overnight.

6.4 Conclusion

Anode supported proton conducting button SOFCs using BZCY as the electrolyte and BPC as the cathode exhibited excellent performance and stability in H_2. The addition of CO into anode feed did not significantly degrade cell performance. Thus, it was successfully used to concentrate CO from syngas with co-production of electricity. It was observed from the anode effluent of an operating SOFC that H_2 was selectively oxidized whereas CO was enriched. The formation of CH_4 was undesirable and was minimized via increasing the reactor temperature.

Future work should be focused on developing high performance coking resistant anode catalyst which ensures the high H_2 conversion and CO concentration effect simultaneously.

References

[1] J. Chow, R. J. Kopp and P. R. Portney, *Science*, 2003, **302**, 1528-1531.

[2] S. Nurnberger, R. Bubar, P. Desclaux, B. Franke, M. Rzepka and U. Stimming, *Energy Environ. Sci.*, 2010, **3**, 150-153.

[3] E. P. Murray, T. Tsai and S. A. Barnett, *Nature,* 1999, **400**, 649-651.

[4] S. McIntosh and R.J. Gorte, *Chem. Rev.,* 2004, **104**, 4845-4865.

[5] K. Sundmacher, *Ind. Eng. Chem. Res.*, 2010, **49**, 10159-10182.

[6] I. Wender, *Fuel Process. Technol.*, 1996, **48**, 189-297.

[7] C. D. Zuo, S. W. Zha, M. L. Liu, M. Hatano and M. Uchiyama, *Adv. Mater.*, 2006, **18**, 3318-3320.

[8] G. A. Mills and F. W. Steffgen, *Catal. Rev.-Sci. Eng.*, 1973, **8**, 159-210.

[9] H. Iwahara, T. Yajima and H. Ushida, *Solid State Ionics*, 1994, **70/71**, 267-271.

[10] D. L. Trimm, *Catal. Today*, 1997, **37**, 233-238.

Chapter 7 Insights into CO Poisoning in High

Performance Proton-conducting Solid Oxide Fuel Cells

7.1 Introduction

Solid oxide fuel cells with oxygen ion conducting electrolyte (OC-SOFC) have been intensively studied for the last several decades. OC-SOFC exhibits higher efficiency, lower environmental impact and comparable fuel diversity in comparison with the conventional thermal engine [1-3]. Since the discovery of protonic conductivity in some oxide materials in 1981[4], many research efforts have been focused on the development of proton-conducting solid oxide fuel cell (PC-SOFC) including those fueled by hydrocarbons through internal steam reforming and/or water gas shift reaction [5-8]. The apparent advantage of PC-SOFC over OC-SOFC is its higher theoretical efficiency since the major electrochemical reaction product, H_2O, is generated at the cathode side without diluting the anode fuels.

In fact, the performance of PC-SOFC fed by fuels containing hydrocarbon is significantly lower than the theoretical value. Jamsak reported that the dramatic power density decrease of the PC-SOFC fed by ethanol was due to an increase in ohmic resistance [5]. The high temperature derivatives of ethanol are mainly CO, H_2 and CH_4. Ni, et al., concluded that the extremely high ohmic overpotential and

concentration overpotential were responsible for the poor performance of methane fueled PC-SOFC [6]. Luisetto conducted experiments with syngas (obtained by CH_4 internal CO_2-reforming) as the fuel for PC-SOFC and ascribed the low power density to carbon deposition and high reaction resistance [7]. Although Arpornwichanop speculated that CO might deteriorate PC-SOFC performance but the experimental evidence is needed to be more convincing [8]. In contrast to the strong CO surface active site blocking effect on metallic catalysts at low temperature in proton exchange membrane fuel cells (PEMFC) [9-11], CO chemisorption was greatly suppressed at high temperature during CO/H_2 competitive adsorption [12]. Thus, CO poisoning effect in PC-SOFC was not normally considered.

In this chapter, proton conductor $BaCe_{0.7}Zr_{0.1}Y_{0.2}O_3$ (BZCY) was used as the electrolyte when fabricating high performance anode supported PC-SOFC. The influence of CO on the performance of cells at 700 ^{o}C was studied and three distinguishable poisoning stages and corresponding mechanisms were proposed.

7.2 Experimental

The cell used this chapter was modified using diluted Ag paste infiltrated into porous cathode layer in order to increase both activity and conductivity. The final active area of the fuel cells was 0.47 cm^2. In the fuel cell test, pure oxygen was used as the cathode oxidant with a flow rate of 50 mL min^{-1}. The anode inlet gas pressure was 137 kPa (20 psi), the composition was adjusted using three

100

independent and calibrated flow controllers connected to H_2, CO and N_2, respectively.

7.3 Results and Discussions

7.3.1 Button cell performances in H_2 and syngas
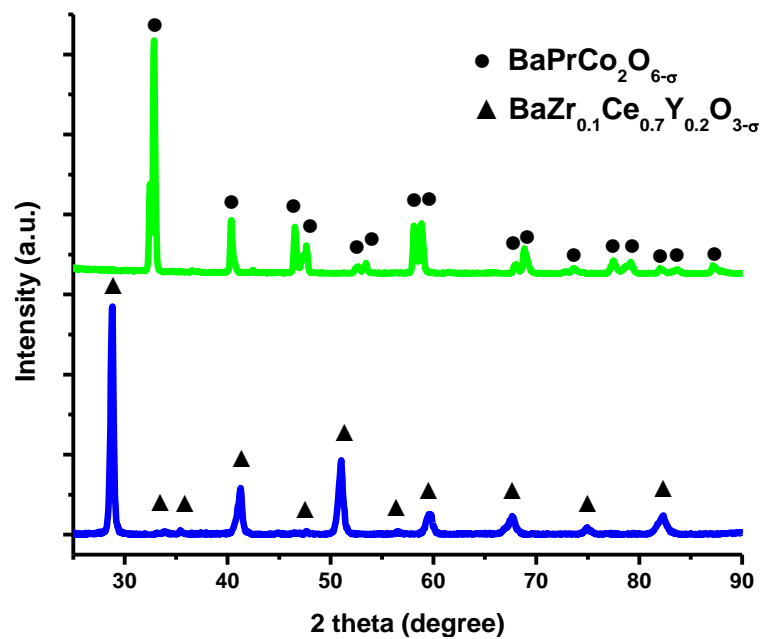
Figure 7-1 XRD patterns of synthesized BPC and BZCY powders.

XRD patterns of BPC and BZCY in Fig. 7-1 confirmed that the pure perovskite phase, no impurities were identified. Fig. 7-2 shows the microstructure of button cell cross-section, the BZCY electrolyte (~20 μm) was essentially dense without open micro pores or cracks. To investigate PC-SOFC button cell performance, we examined the current-voltage characteristics and the

corresponding power density curves in H_2 feed. The button cell exhibited maximum power densities of 488 mW cm^{-2}, 592 mW cm^{-2}, 705 mW cm^{-2} and 812 mW cm^{-2} at 600 °C, 650 °C, 700 °C and 750 °C, respectively (Fig. 7-3). Electrochemical impedance spectra were also analyzed in Fig. 7-4, which confirmed that the cell had a considerably low polarization resistance and therefore, made it extremely sensitive to poisoning effect. The test temperature for PC-SOFC in syngas was selected at 700 °C, not only because of the high protonic transport number of BZCY below this temperature [13,14], but also the minimized side reactions effects, which will be discussed in the following parts.
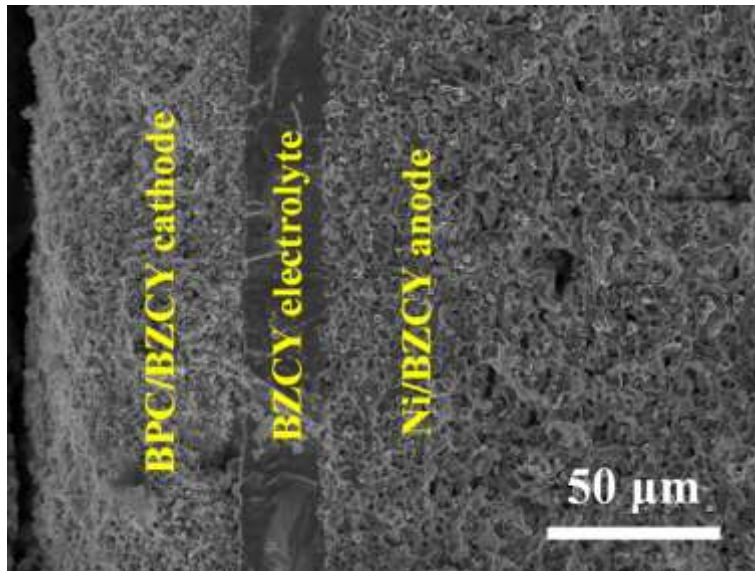
Figure 7-2 SEM image of button cell cross-section after operation

Fig. 7-5 compares the maximum power densities (MPD) of PC-SOFC in three groups of feed streams at 700 °C. Since MPD in CO containing fuels kept

decreasing as a function of time, all the data were recorded after 30 min of treatment by the specified gases. The red arrows in the figure indicated the percentage of power density losses in the CO containing feeds relative to the others which each individual groups. In group 1, the cells were fuelled by pure gases of either H_2 or CO. A MPD of 24 mW cm^{-2} was obtained in pure CO, which was 96.6 % lower than that in H_2. It also implied the BZCY electrolyte was not 100% protonic conductor at the examining temperature. The CO/H_2 ratio of syngas fuel in group 2 was fixed at 2, which was the same with that of methane-derived syngas. Relative to that fuelled by a CO-free mixed gas with a composition of $N_2/H_2 = 2$, the MPD dropped 9.2 % in syngas. This percentage of the decrease was escalated to 34.4% in group 3 when the CO/H_2 ratio of syngas was enhanced to 9.
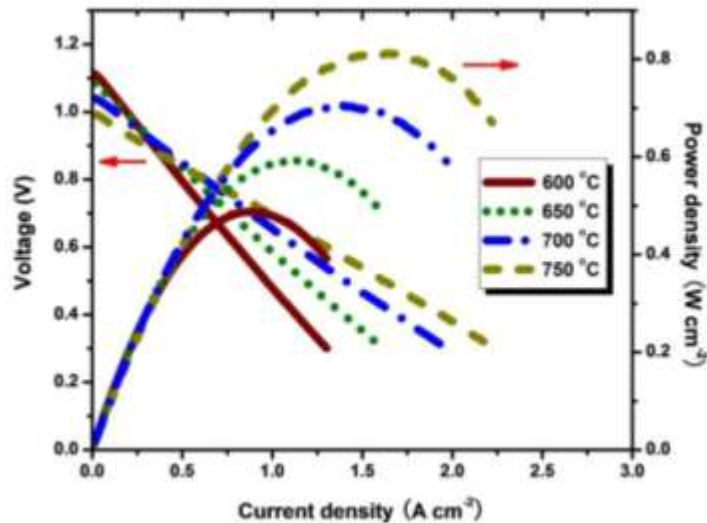
Figure 7-3 I-V characteristics and power density curves in H_2 at different temperatures.

103
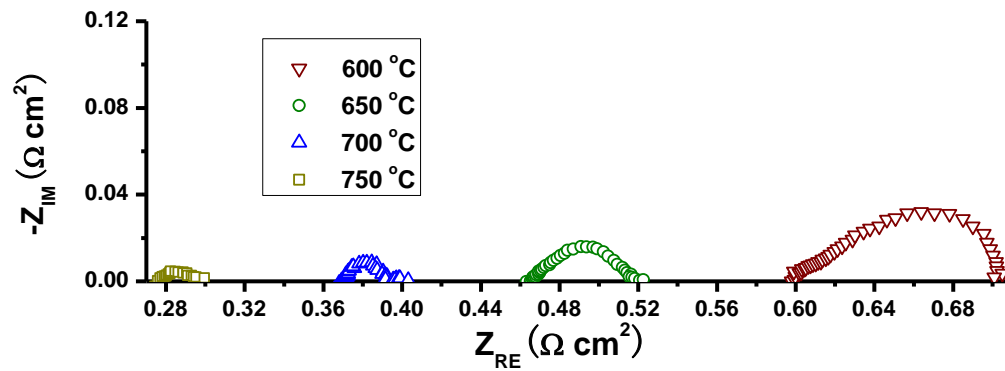
Figure 7-4 Impedance spectra H_2 at different temperatures
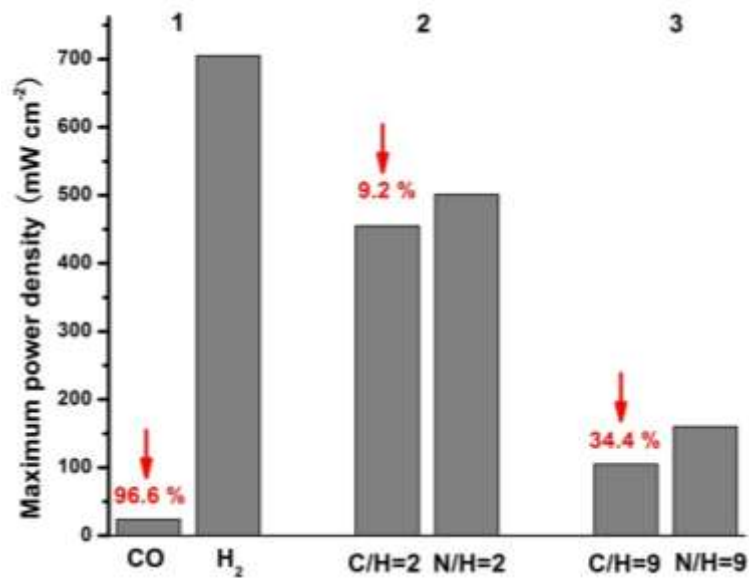
Figure 7-5 A comparison of PC-SOFC maximum power densities in CO, H_2, syngas and N_2-H_2 gas mixtures at 700 ^oC.

The negative effects of the presence of CO in the feed steam on the performance of PC-SOFC were systematically investigated in the following

sections as a function of PC-SOFC treatment time in syngas. The H_2 concentration in syngas was fixed at 10%, since lower H_2 content in the feedstock could drastically accelerate the poisoning rate and promote the effectiveness in evaluating the catalyst deactivation.
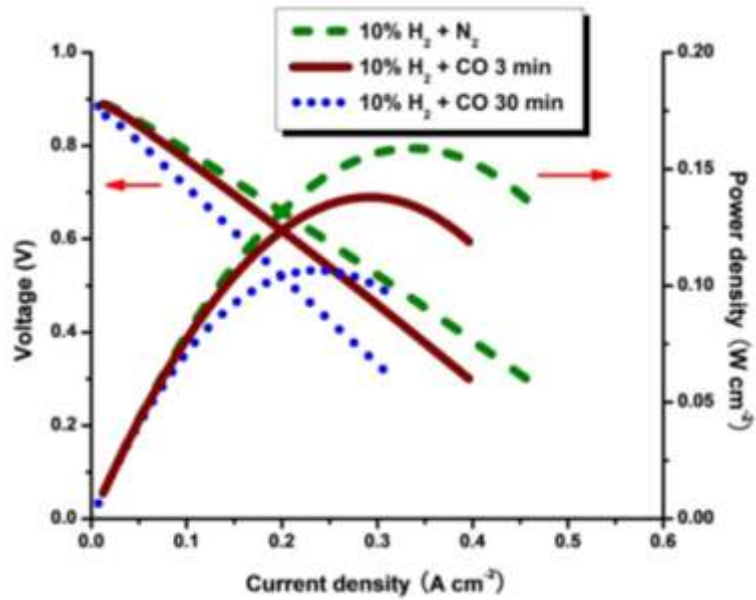
Figure 7-6 A comparison of I-V characteristics and power density curves at different stages of CO poisoning at 700 ^{o}C.
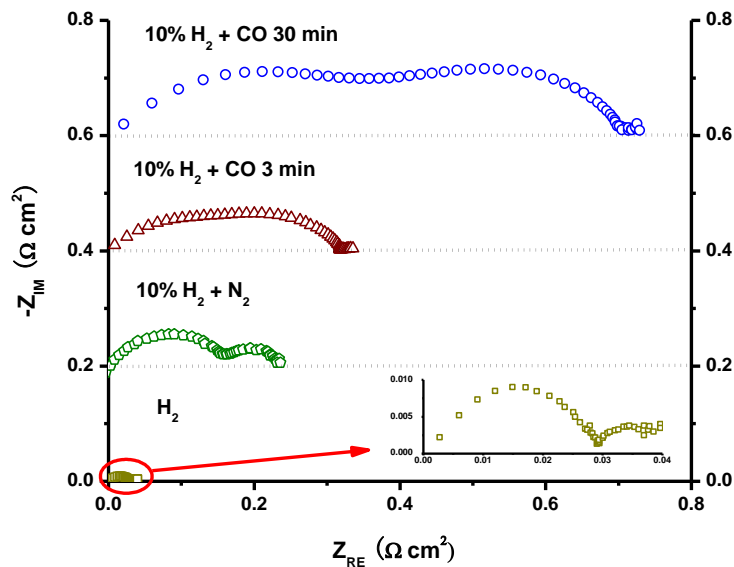
Figure 7-7 A comparison of impedance spectra at different stages of CO poisoning at 700 $^{\circ}$C.

7.3.2 The 1st stage: chemical poisoning effect

The influence of CO on fuel cell performance was firstly characterized through polarization curves and impedance spectra in 10% H_2 + CO. Around 20 % of maximum power density drop was observed right after the balance gas was changed to CO from N_2 (Fig. 7-6), although the open circuit voltage (OCV) did not change essentially. All the ohmic resistances of the impedance spectra in Fig. 7-7 were not illustrated. After the balance gas was switched from N_2 to CO, an increase in the polarization resistance was observed almost simultaneously.

106
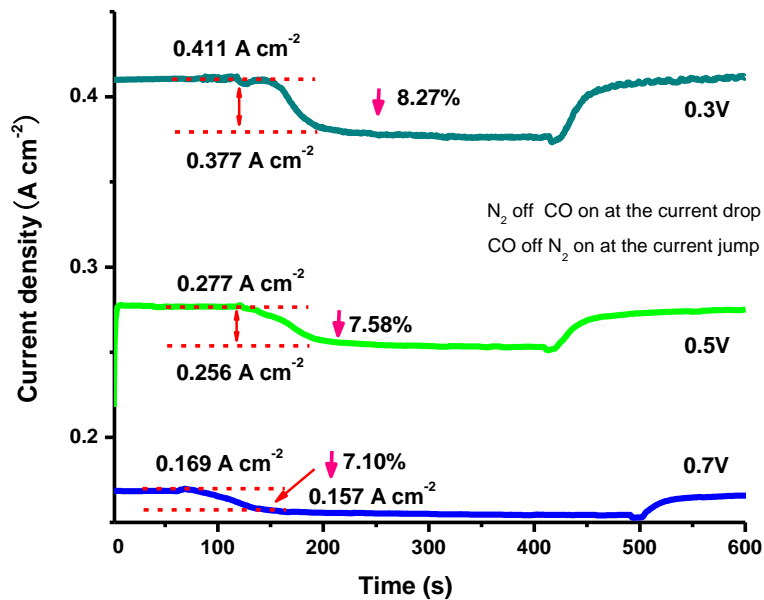
Figure 7-8 Variations of current density with different applied voltages during the 1st stage of CO poisoning study under PC-SOFC potentiostatic mode at 700 ^{o}C.
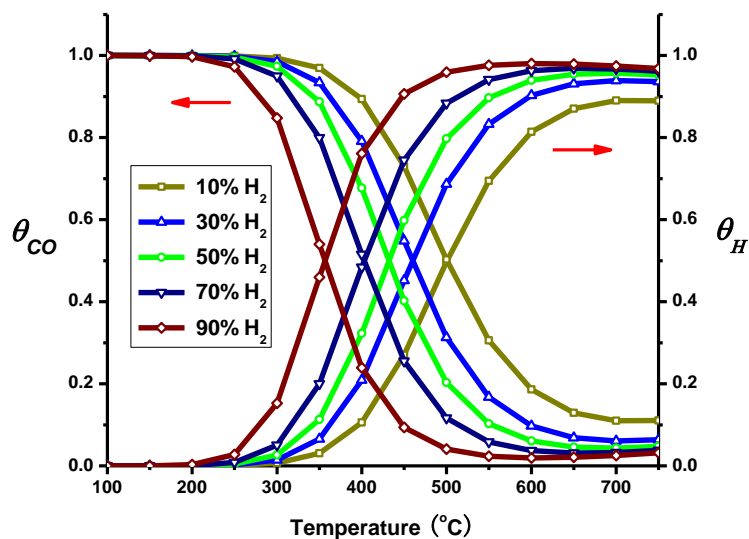
Figure 7-9 H and CO surface coverage as functions of temperature and H$_2$ partial pressure, the total pressure was 137 kPa.

Then CO poisoning effect was evaluated under potentiostatic mode for a short period of time (Fig. 7-8). After the initial introduction of CO, there was an immediate sharp current drop. The magnitude of it was between 7% and 9% depending on the applied potentials. In addition, the variation of anode feed flow rate did not play a significant role in shaping the poisoning curves. Once CO was removed from the fuel feed, the current was entirely recovered to its original value after the anode chamber gas substitution and the CO desorption from Ni were completed.

It was important that the binary diffusivity of H_2-N_2 and H_2-CO were essentially identical which made the mass transport influence on the fuel cells performance negligible [15]. Eventually, relative to N_2 which were inert gas, CO was readily activated by Ni catalyst. Since the chemisorbed CO molecules were essentially unable to be oxidized in PC-SOFC, they might sequentially influence the activation and conversion of H_2 molecules via either active site or geometric blocking mechanisms. Thus, a lower fuel cell performance and high polarization resistance were observed in syngas feed.

In order to evaluate the influence of CO on H_2 electrochemical oxidation in PC-SOFC at high temperature, a CO/H_2 competitive adsorption model was established. Both CO and H_2 adsorptions were based on Langmuir model as shown below,

$$H_2 + 2(Ni) \underset{k_d^H}{\overset{k_a^H}{\rightleftharpoons}} 2H_{ad}(Ni) \tag{7-1}$$

$$CO + (Ni) \underset{K_d^{CO}}{\overset{K_a^{CO}}{\rightleftarrows}} CO_{ad}(Ni) \qquad (7\text{-}2)$$

Where k_a and k_d represent the adsorption and the desorption rate constant, respectively; (Ni) indicates the surface active site on Ni. Assuming that the interaction among adsorbates was negligible and only linear structure of CO adsorption was considered [16], we can have the following expressions on surface coverage of CO and H (θ_H) shown in (7-3) and (7-4).

$$\theta_H = \frac{\sqrt{\left(\dfrac{k_a^H P_{H_2}}{k_d^H}\right)}}{1 + \dfrac{k_a^{CO} P_{CO}}{k_d^{CO}} + \sqrt{\left(\dfrac{k_a^H P_{H_2}}{k_d^H}\right)}} \qquad (7\text{-}3)$$

$$\theta_{CO} = \frac{\dfrac{k_a^{CO} P_{CO}}{k_d^{CO}}}{1 + \dfrac{k_a^{CO} P_{CO}}{k_d^{CO}} + \sqrt{\left(\dfrac{k_a^H P_{H_2}}{k_d^H}\right)}} \qquad (7\text{-}4)$$

where P is the partial pressure of the specified gaseous species. In the calculation, the total pressure was 137 kPa equaling to the experiment condition. By using the kinetic parameters and equations derived from literatures [17, 18], θ_{CO} and θ_H were obtained as functions of temperature and H_2 partial pressures (Fig. 7-9).

CO molecule was able to bind with the transition metal catalyst much more strongly than H_2 as a result of its unique electronic band structure. During competitive adsorption of CO and H_2 at low temperature (< 200 $^{\circ}$C), it is commonly known that the catalyst surface was exclusively covered by CO with

surface coverage (θ_{CO}) close to unit. The strong active site blocking effect was ascribed as the major reason for serious CO poisoning effect in PEMFC [9-11]. At high temperature (> 600 $^{\circ}$C), though the adsorption of H_2 was not greatly affected by CO adsorption, approximately 10 % of the Ni surface was still occupied by CO adsorbate in syngas consisting of 10% H_2/CO at 700 $^{\circ}$C as calculated in Fig. 7-5. Accordingly, it was not surprised to have observed 7 ~ 9 % current drop when CO was introduced to the fuel in Fig. 7-8. In summary, it was rational to conclude that the instant degradations observed in Figs. 7-6, 7-7 and 7-8 in syngas fuels were majorly attributed to the active site blocking effect of chemisorbed CO molecules.

7.3.3 The 2nd stage: electrochemical reaction accelerated carbon deposition

During the prolonged operation in CO containing feed, the PC-SOFC performance degraded gradually as shown in Fig. 7-10. The maximum power density decreased to 60 % of its original value while little OCV drop occurred (Fig. 7-6). In the meantime, the fuel cell ohmic resistance did not vary apparently within this stage. However, large increase of polarization resistance was detected indicating considerable deactivation of the catalyst and higher degree of CO poisoning (Fig. 7-7). Nevertheless, the severe performance loss at the current stage was fully recovered after CO flow was substituted by N_2. In addition, it was also found that the fuel cell operation conditions had an obvious influence on the level of the performance degradation as shown in Fig. 7-10.
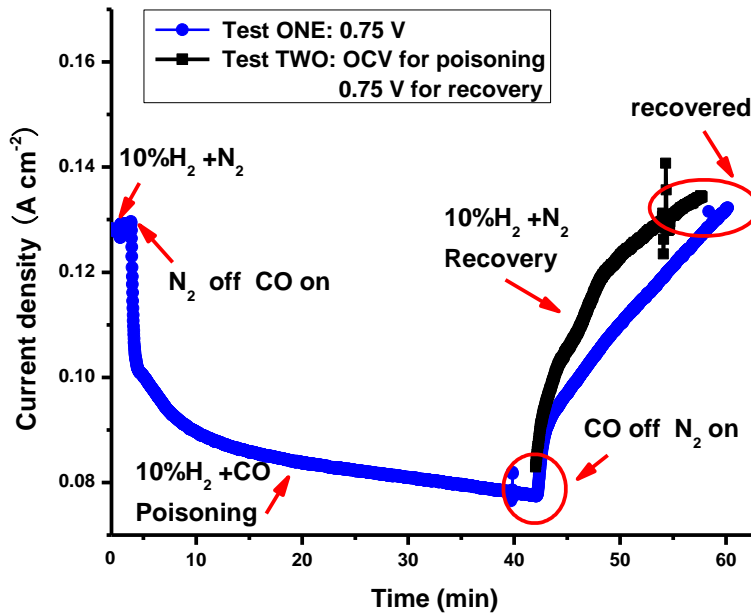
Figure 7-10 CO poisoning and recovery in the 2nd stage under different testing conditions at 700 ^{o}C.

In order to deconvolute CO poisoning mechanisms in terms of chemical and electrochemical reaction effects, a pair of tests with identical CO treatment time was conducted. In test ONE, both CO poisoning and recovery process were recorded under potentiostatic mode at 0.75 V. In contrast, in test TWO, the poisoning process was completed under OCV condition in which the PC-SOFC could be recognized as a pure chemical reactor without any electrochemical reactions. But the recovery was monitored under potentiostatic mode in order to determine and compare performance variations. From the results showed in Fig. 10, it could be observed that in test ONE, the current density drop resulting from CO effect was more severe than that of test TWO: after the 1st stage poisoning, the

current decreased further from 0.102 A cm^{-2} to 0.078 A cm^{-2} within 40 min in test ONE; however, after the identical time period of exposure to syngas, the performance only dropped to 0.082 A cm^{-2} in test TWO. During the recovery cycle, although the performance loss of cells in both tests were reversible, it took a longer time for the cell in test ONE to be fully recovered and a steeper current density recovery curve was recorded in test TWO. As θ_{CO} was only ~ 10% under experimental conditions, it was not suitable to reuse CO active site blocking mechanism to address the 2nd stage CO poisoning.

In fact, after the CO poisoning study, no obvious structure change of the anodes in either cells was found in the SEM examinations. Detailed surface information was revealed by using XPS analysis. Fig. 7-11 compares the spectra of C 1s of cells operated in either test ONE or test TWO, which indicates that carbon was deposited on the surface of Ni after syngas treatment. More importantly, a stronger carbon signal was always detected on the anode in test TWO. Eventually, when the fuel cell was a pure chemical reactor operating under OCV condition, the carbon deposition could be easily attributed to the applicable chemical reactions including:

$$CO + H_2 \leftrightarrow C + H_2O \tag{7-5}$$

$$2CO \leftrightarrow C + CO_2 \tag{7-6}$$

where reaction (7-5) is kinetically much faster and thus became the major source of coke [19]. In contrast, when the fuel cell was working under potentiostatic mode, this case might become complicated. In addition to the carbon sources from

112

reaction (7-5) and (7-6), it was plausible that there was another parallel carbon source contributed, or the existing carbon source was affected, by the electrochemical oxidation of H_2. The combined effects accelerated the carbon deposition and caused more severe cells performance loss in test TWO.
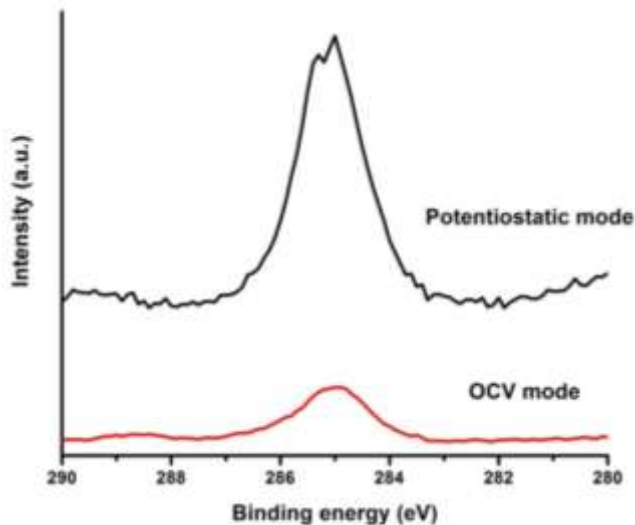
Figure 7-11 XPS spectra of C1s obtained on PC-SOFC anode after tests in either potentiostatic mode or OCV mode.

Based on the above point of view, an electrochemical reaction accelerated carbon deposition mechanism was proposed in explaining the 2nd stage CO poisoning effect. As long as the electrochemical oxidation of H_2 started to proceed, a localized surface diffusion area (SDA) would be established adjacent to TPB and extended to Ni with a width of several hundreds of Angstrom [20]. When H_{ad} was electrochemically consumed at TPB, both H_{ad} and CO_{ad} located within SDA began to move and redistribute driven by the gradient of chemical

potential [20, 21]. The resulting dynamic equilibrium of θ_H tended to decrease whereas θ_{CO} would rise up within SDA. Consequently, compared with θ_{CO} in a stand-by fuel cells functioning as a pure chemical reactor, the higher θ_{CO} on Ni in an operating PC-SOFC led to a faster catalyzed carbon deposition rate. The larger amount of carbon deposits on the surface of Ni would block more active sites, further slowed down H_2 electrochemical oxidation and more severely degraded PC-SOFC performance. A schematic of the mechanism was illustrated in Fig. 7-12.

The 2nd stage CO poisoning was starting to reach equilibrium after 5 h of CO treatment and full reversibility was maintained (Fig.7-13). Upon substitution of CO by N_2, there were basically two mechanisms which might be responsible for the carbon removal. The first one was attributable to the direct oxidation of carbon by oxygen ions since BZCY was not pure proton conductor at the experimental temperature [13, 14]: the PC-SOFC running in pure CO had a maximum power density of 25 mW cm^{-2} as described in Fig. 7-5. The other mechanism could be explained by the reaction of the carbon with the water vapor derived from either the anode fuel stream or the residual product of reaction (7-5).
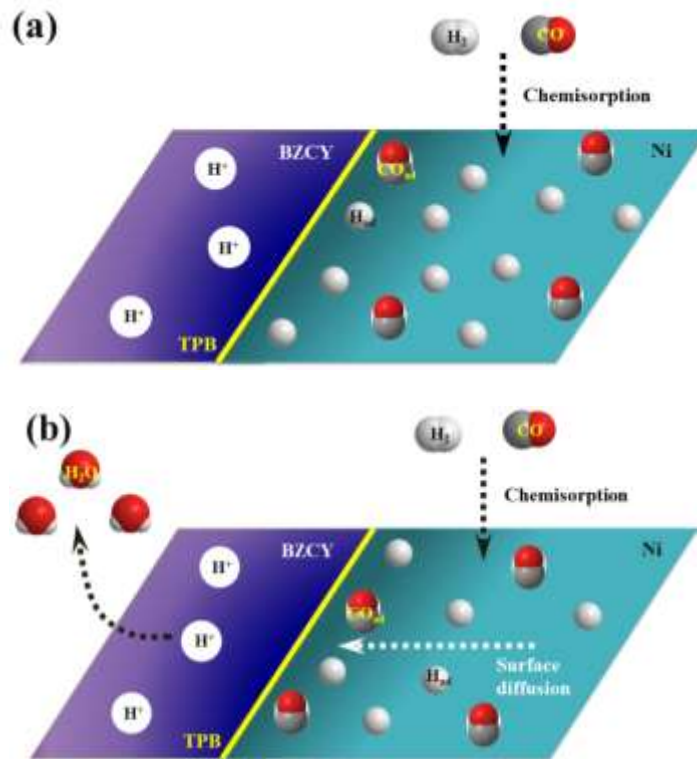
Figure 7-12 Schematics of the electrochemical CO poisoning mechanism. (a) the original state of the adsorbate distribution within the TPB adjacent area in a stand-by PC-SOFC; (b) the equilibrium state of the adsorbate distribution within the TPB adjacent area in an operating PC-SOFC.

7.3.4 The 3rd stage: metal dusting of Ni

Fig. 7-13 shows a typical fuel cell destructive test when the operation potential was 0.75V. A serious OCV drop was observed after 11 h of fuel cell operation in syngas. The main reason was believed to be the electrolyte deterioration caused by the volume expansion of coked Ni anode. Therefore, the PC-SOFC performance degradation at this stage was irreversible. Normally, after

long time operation in syngas, the deposited carbon atoms would develop sufficient C-C bonds and accumulate to form coke on Ni surface, which was thermodynamically unstable at high temperature. If it was not removed in time, the formed coke would trend to dissolve into and then grow inward to bulk Ni crystal lattice, resulting in serious metallic structural disintegration. This catastrophic interaction between coke and metal was entitled as metal dusting [22]. Since the 3rd stage poisoning always overlapped with the 2nd stage, precisely locating its starting point was not an easy task throughout the experiment. Usually, the cell performance deterioration started to become completely irreversible after 8 h of operation in 10% H_2 + CO. It should be noted that anode fuel flow rate was able to influence the 3rd stage poisoning and a higher flow rate of syngas could shorten the time of electrolyte cracking.
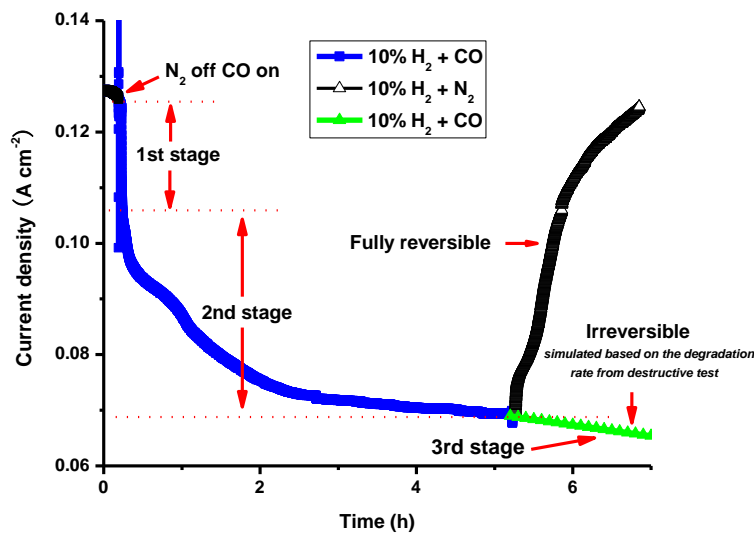
Figure 7-13 An overview of three stages of CO poisoning and recovery curves in Ni based PC-SOFC.
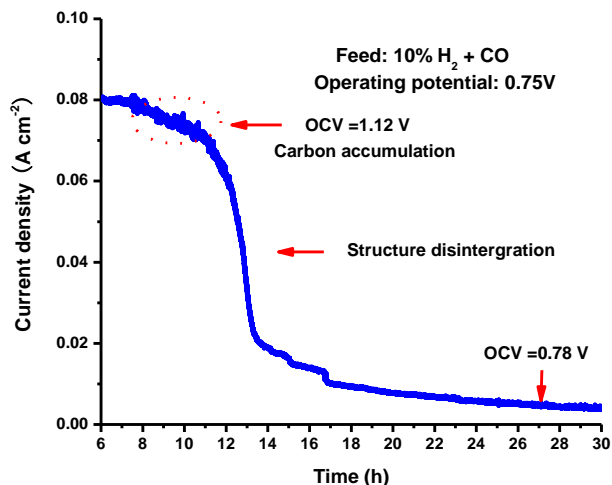
Figure 7-14 Influence of carbon deposition on PC-SOFC performance under potentiostatic mode. OCV was recorded in pure H_2.

In the meantime, since CO_2 was generated via reactions (7-7) and (7-8), a major concern associated with the PC-SOFC stability during longevity test was the interaction between CO_2 and BZCY which was capable to change the properties of both the anode and the electrolyte. Thus, the concentration of CO_2 in the anode chamber was measured by GC from the anode effluent. Analysis revealed that the CO_2 concentration was below 2 % under all the experimental conditions. The calculated equilibrium composition of 10% H_2 + CO at 700 ^{o}C in Fig. 7-16 also confirmed that no apparent gaseous compositional change was expected. Besides, because numerous studies have proved the chemical stability of BZCY in the environment with a CO_2 concentration around 10 % [23-25], the slow deterioration of BZCY was unlikely to happen, which led to the gradual irreversible drop of current. Thereby, the side reaction effects were unlikely to

overshadow the CO poisoning effect determination in PC-SOFC.
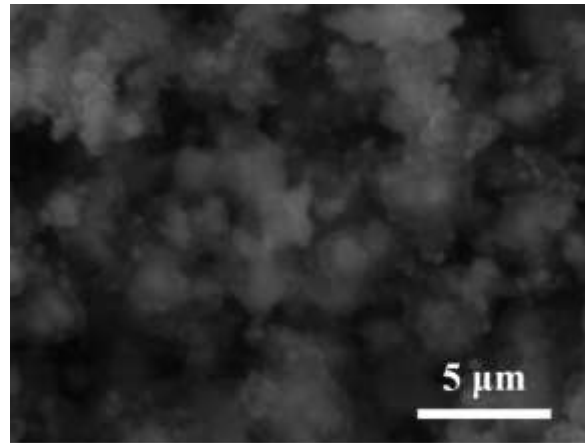
Figure 7-15 Microstructure of carbon deposits on the Ni anode after prolonged PC-SOFC operation in syngas at 700 $^{\circ}$C.
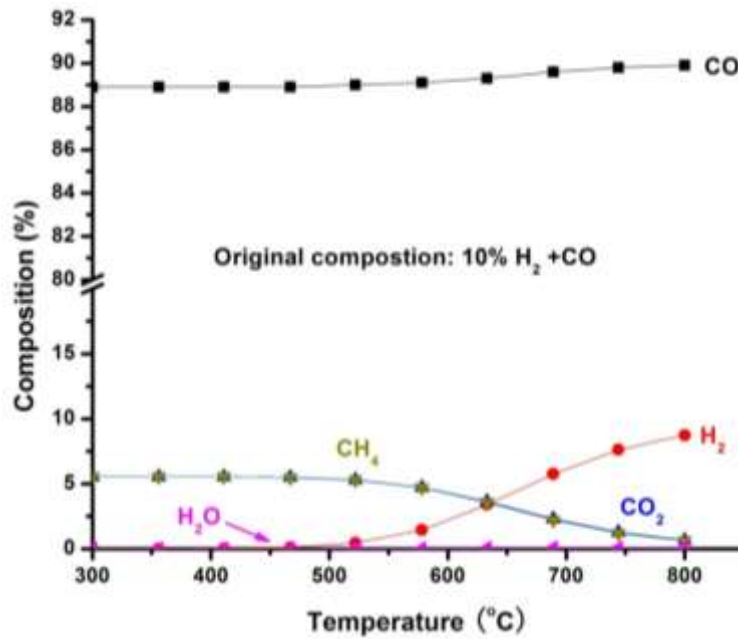
Figure 7-16 Equilibrium composition of 10% H_2 + CO at various temperatures.

7.4 Conclusions

CO poisoning in PC-SOFC at high temperature was significantly different from the low temperature catalyst deactivation observed in PEMFC. In PC-SOFC, the initial poisoning effect was instant and reversible, which could be explained using active site blocking effect by CO adsorbates. The 2nd stage poisoning was also fully reversible but took relatively longer time to reach equilibrium, which contributed more than 75 % of the total revisable fuel cell performance loss. The gradual poisoning effect was interpreted through the electrochemical reaction accelerated carbon deposition on Ni. Thereby, the following H_{ad} electrochemical oxidation was strongly suppressed. The third stage poisoning effect was destructive and irreversible, which was mainly caused by Ni metal dusting and BZCY electrolyte cracking under experimental conditions. Finally, when utilizing syngas in PC-SOFC with a Ni anode, it was highly recommended to increase the percentage of H_2 in the feedstock for an efficient fuel conversion.

References

[1] S. D. Park, J. M. Vohs and R. J. Gorte, *Nature*, 2000, **404**, 265-267.

[2] A. Atkinson, S. Barnett, R. J. Gorte, J. T. S. Irvine, A. J. McEvoy, M. Mogensen, S. C. Singhal and J. Vohs, *Nature Materials*, 2004, **3**, 17-27.

[3] Z. P. Shao and S. M. Haile, *Nature*, 2004, **431**, 170-173.

[4] H. Iwahara, T. Esaka, H. Uchida and N. Maeda, *Solid State Ionics*, 1981, **3-4**, 359-363.

[5] W. Jamsak, S. Assabumrungrat, P. L. Douglas, N. Laosiripojana, R. Suwanwarangkul, S. Charojrochkul and E. Croiset, *Chem. Eng. J.*, 2007, **133**, 187-194.

[6] M. Ni, D. Y. C. Leung and M. K. H. Leung, *J. Power Sources*, 2009, **194**, 1226-1227.

[7] I. Luisetto, E. Di Bartolomeo, A. DEpifanio and S. Licoccia, *J. Electrochem. Soc.*, 2011, **158**, B1368-B1372.

[8] A. Arpornwichanop, Y. Patcharavorachot and S. Assabumrungrat, *Chem. Eng. Sci.*, 2010, **65**, 581-589.

[9] H. F. Oetjen, V. M. Schmidt, U. Stimming and F. Trila, *J. Electrochem. Soc.*, 1996, **143**, 3838-3842.

[10] G. A. Camara, E. A. Ticianelli, S. Mukerjee, S. J. Lee and J. McBreen, *J. Electrochem. Soc.*, 2002, **149**, A748-A753.

[11] J. H. Wee and K. Y. Lee, *J. Power Sources*, 2006, **157**, 128-135.

[12] M. J. Kahlich, H. A. Gasteiger and R. J. Behm, *J. Catal.*, 1997, **171**, 93-105.

[13] H. Iwahara, T. Yajima and H. Ushida, *Solid State Ionics*, 1994, **70**, 267-271.

[14] K. Asano, Y. Tominaga, Y. Mugikura and T. Watanabe, *Solid State Ionics*, 2010, **181**, 236-239.

[15] Y. Jiang and A. V. Virkar, *J. Electrochem. Soc.*, 2003, **150**, A942-A951.

[16] A. Eichler, *Surf. Sci.*, 2003, **526**, 332-340.

[17] G. B. Raupp and J. A. Dumesic, *J. Catal.*, 1985, **96**, 597-612.

[18] T. Ishihara, N. Horiuchi, T. Inoue, K. Eguchi, Y. Takita and H. Arai, *J. Catal.*, 1992, **136**, 232-241.

[19] P. L. Walker, J. F. Rakszawski and G. R. Imperial, *J. Phys. Chem.*, 1959, **63**, 140-149.

[20] R. E. Williford and L. A. Chick, *Surf. Sci.*, 2003, **547**, 421-437.

[21] S. B. Adler, *Chem. Rev.*, 2004, **104**, 4791-4843.

[22] J. C. N. Paz and H. J. Grabke, *Oxid. Met.*, 1993, **39**, 437-456.

[23] K. H. Ryu and S. M. Haile, *Solid State Ionics*, 1999, **125**, 355-367.

[24] K. D. Kreuer, *Ann. Rev. Mater. Res.*, 2003, **33**, 333-359.

[25] S. Barison, M. Battagliarin, T. Cavallin, L. Doubova, M. Fabrizio, C. Mortalò, S. Boldrini, L. Malavasi and R. Gerbasi, *J. Mater. Chem.*, 2008, **18**, 5120-5128.

Chapter 8 Electrocatalytic Selective Oxidation of H_2 in H_2/CO Gas Mixtures using Solid Oxide Fuel Cells

8.1 Introduction

Solid oxide fuel cells (SOFC) have attracted increasing attentions as promising power sources [1]. Besides their use as electricity generators; SOFCs have potential applications in chemical production and energy storage [2, 3]. Herein, we describe H_2 electrocatalytic selective oxidation in syngas using SOFC with cogeneration of electricity. The Ni-S anode catalyst shows up to 92% H_2 selectivity through selective surface diffusion mechanism. During cyclic treatment, H_2 selectivity and conversion can reach 87.1% and 97.3 %, respectively. We also demonstrate reasonable power output and longevity test stability of the reactor. The observation of electrocatalytic selective oxidation expands the concept of conventional selective oxidation, diversifies the range of targeted reactants and minimizes the energy waste.

8.2 Experimental

8.2.1 Electrochemical tests

The SOFC anode supported button cell fabrication and basic testing techniques were detailed in Chapter 3. Before H_2S treatment, button cell was operated under potentiostatic mode in a pure H_2 stream so as to achieve a steady state and complete NiO reduction. During the H_2S treatment process and the following electrochemical tests, the concentration of H_2S was adjusted by mixing certain gases with certified 500 ppm H_2S + H_2 using separate mass flow controllers. The concentration of H_2 in syngas was controlled roughly by mass flow controller first and then read by data obtained from gas chromatograph (GC, Agilent Technologies 6890N). The flow rate of anode fuel gas varied from 10 to 30 mL min^{-1} whereas the cathode oxygen flow rate was 50 mL min^{-1}. N_2 was used as the reference gas in terms of H_2 selectivity estimation via electrochemical method since the binary diffusivity of H_2-CO was essentially identical with that of H_2-N_2, as shown below [4]:

$$D_{H_2\text{-CO}} = 6.373 \text{ cm}^2 \text{ s}^{-1}$$

$$D_{H_2\text{-}N_2} = 6.303 \text{ cm}^2 \text{ s}^{-1}$$

Thus, there was little fuel dilution effects on SOFC performance.

8.2.2 Other characterizations

Anode effluent composition was analyzed using mass spectrometer (Thermostar QMS 200) and a GC using TCD detectors. Concentrations of CO_2 and H_2 before and after fuel cell operation were both recorded.

CO_2, despite its extremely low concentration, was among the components of the exhaust gases even under OCV condition of the fuel cell because of CO-H_2 reactions at high temperatures and gas leakage from either electrolyte or sealant. Thus, the conversion and selectivity of H_2 were calculated from the following equations:

$$H_2\ conversion\ =\ \frac{moles\ of\ H_2\ converted}{moles\ of\ H_2\ introduced} \times 100\% \tag{8-1}$$

$$H_2\ selectivity\ =\ \frac{moles\ of\ H_2\ converted}{moles\ of\ H_2\ converted\ +\ moles\ of\ CO_2\ produced} \times 100\%$$

$$\tag{8-2}$$

We assumed that the increase of CO_2 concentration mainly came from CO electrochemical oxidation. As the CO_2 concentration before fuel cell discharging was low, the consumption of H_2 and the volume decrease of resulting exhaust gas only had limited influence on CO_2 concentration increase. Thus, the reported H_2 selectivity was slightly lower than the actual value.

124

8.2.3 Anode effluent cyclic treatment

Certified 40 % H_2 + CO was used as the original feed for the first cycle of H_2 conversion. Due to the side reactions and inevitable gas leakage, very small amount of CO_2 was detected after this feed passed through anode chamber at OCV condition. Nonetheless, only CO_2 produced electrochemically was considered. During the subsequent cyclic treatment, the cell operated under potentiostatic mode at 0.7 V. The gas composition of the previous anode effluent (C_{out-P1}) was determined and recorded using GC, then a stream of gas mixture containing H_2, CO and CO_2 with the same composition of C_{out-P1} was used as the anode feed for the next treatment cycle (C_{in-N1}, $C_{out-P1} = C_{in-N1}$). After cell treatment, anode effluent of this cell was recorded again as C_{out-P2}. This loop repeated 8 times in order to maximize H_2 conversion. The accumulative H_2 selectivity and conversion was calculated based on the original and the final gas compositions.

8.3 Results and Discussions

8.3.1 H_2 selective oxidation

The catalytic selective oxidation of CO from syngas was first reported by Cohn in 1965. Since then, significant progress has been made on catalyst development [5-7]. However, reports on H_2 selective oxidation (HSO) from the

same gas mixtures are much less common. CO molecule has "reactive orbitals" (5σ, $2\pi^*$) enabling it to adsorb on transition metal catalyst more strongly than a H_2 molecule [8]. Thus, HSO in syngas is not scientifically feasible at low temperature because catalyst surface is exclusively covered by CO on Ni as described in Chapter 6 (Fig. 6-5). At high temperature, on the other hand, satisfactory H_2 selectivity/conversion is still technically difficult to achieve using either chemical method or SOFC technology [9]. A distinguishable feature of SOFC electrocatalytic process relative to its conventional catalytic counterpart lies in its 4-step reaction. For conventional catalysis, the reaction process usually has 3 steps, i.e., the adsorption, the reactions among adsorbates and the desorption. In contrast, the process in electrocatalysis includes 4 steps. In addition to the adsorption/desorption steps, the adsorbate also needs to move, via surface diffusion [10], to fuel cells triple-phase boundaries(TPB) where the electrochemical reaction takes place.. The unique features of electrocatalysis promise to open new windows for HSO in syngas.

8.3.2 Ni-S catalyst characterizations

When SOFC electrolyte is YSZ, an oxygen ionic conductor, both of the readily chemisorbed CO (CO_{ad}) and H_2 (H_{ad}) can be oxidized by oxygen ions theoretically. The challenge of the present work is to design and develop the anode catalyst. Not only should it have high activity for H_2 oxidation, but also

should not allow CO molecules to be readily activated. It is also necessary to avoid both carbon deposition and syngas methanation in operating environment of SOFC [11]. In the present work, we used the anode supported button cell, Ni-S+YSZ/YSZ/LSM, (Fig. 8-1). The Ni-S catalyst was developed via the *in-situ* H_2S treatment at 850 ^oC using 500 ppm H_2S balanced with H_2 under a potentiostatic mode. The potential of the cell was 0.8 V and the treatment lasted 6 h. In the experiments following H_2S treatment, pH_2S/pH_2 was maintained at 200 ppm in order to sustain catalyst surface composition.
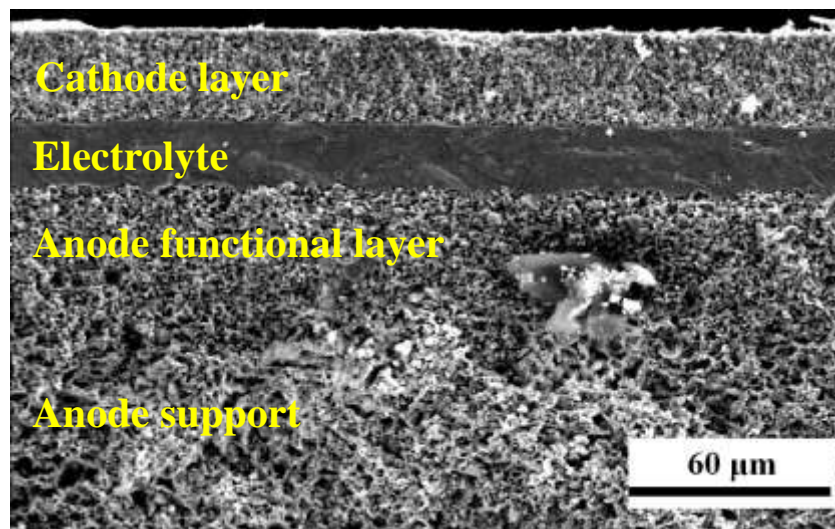
Figure 8-1 SEM image of cross sectional view of SOFC button cell after test.

The beneficial effect of well-controlled S poisoning on selectivity has been observed and studied widely [12]. A major concern on Ni-S anode catalyst was its surface composition. Through intensive investigations using both computational and experimental approaches, including in SOFC environment [13-15], it was

confirmed that S was only chemisorbed (S$_{ad}$) on Ni surface without formation of metal sulfide under the present experiment conditions. Another point which should be addressed is S adsorption stoichiometry of Ni-S/YSZ catalyst. Compared with S$_{ad}$ concentration measured on well-defined single crystal, it became much more difficult to determine S coverage (θ_s) at high temperature on polycrystalline Ni. Nonetheless, it was estimated that 8.37×10^{14} atoms/cm^2 of S$_{ad}$ was accumulated on Ni surface when saturation state was achieved in this experiment [16]. It was determined that θ_s of electrochemically adsorbed S on SOFC anode was measured electrochemically as 0.84 assuming $\theta_s = 1 - j_0^s / j_0$ [17], where j_0 and j_0^s are the measured exchange current densities before and after H$_2$S poisoning, respectively.

8.3.3 H$_2$ electrocatalytic selective oxidation in SOFC

The negative impacts of various factors, including side reactions and dilute gas transport behaviours in SOFC [18], on the conclusion of H$_2$ electrocatalytic oxidation have been dealt with in the last section of the chapter, and only major discoveries are to be discussed here. Due to larger surface diffusion resistance and charge transfer resistance [19], the peak power density in CO was roughly half of that in H$_2$. Nevertheless, the performance in 10% H$_2$ + CO (HC) was considerably higher than that in 10% H$_2$ + N$_2$ (HN), suggesting that CO was the major active

fuel in HC system (Fig. 8-2). H_2 selectivity results obtained from GC also confirmed this speculation, which will be discussed later. In contrast, in the fuel cell with Ni-S catalyst, the peak power density in CO became negligible, which was only 90 mW cm^{-2}, about 20 % of that in H_2 (Fig. 8-3). However, a surprising discovery was that the cell performances fed by HC and HN became almost identical, both of which achieved over 200 mW cm^{-2} peak power densities.
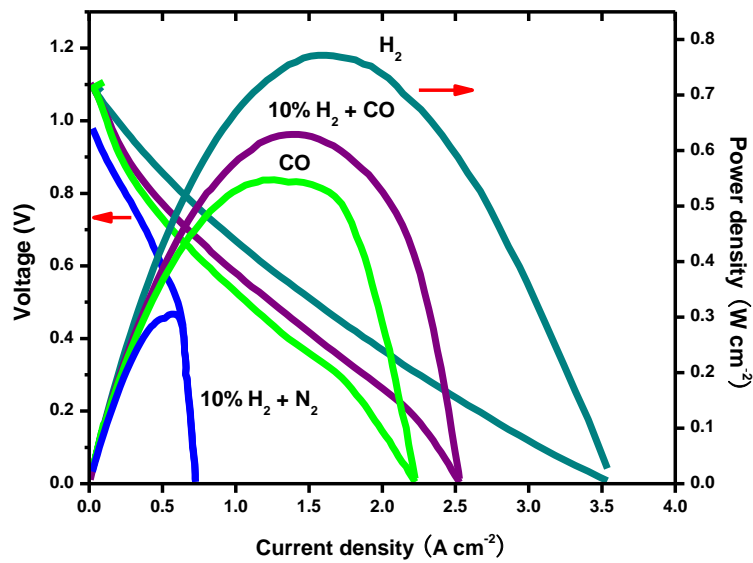
Figure 8-2 Performance plots of fuel cells with Ni/YSZ anode catalyst.
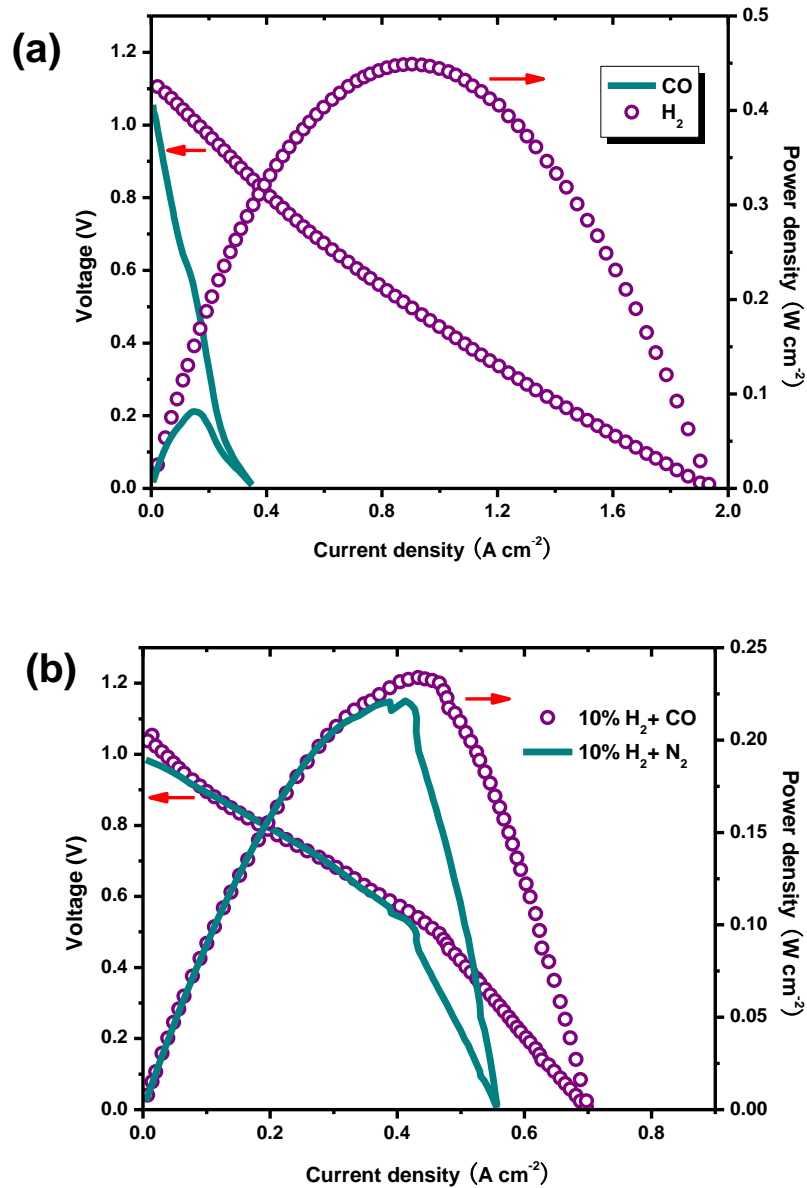
Figure 8-3 Polarization and power density plots of fuel cells with Ni-S/YSZ anode catalyst. (a): In H_2 and CO fuels. (b): In 10% H_2 + N_2 and 10% H_2 + CO fuels.

Considering the major component CO in the former feed was also a good fuel (Fig. 8-2) and the open circuit voltage (OCV) of the latter group was around 0.1 V

lower, we could rationally assume that H_2 was preferentially oxidized in syngas, which was further proved by selectivity data and potentiostatic test (Fig. 8-4). Electrochemical impedance spectra served as persuasive references for the evaluation of fuel cell catalyst activity [20]. Fig. 8-5 (a) and (b) clearly demonstrate that comparing with the spectra for the cell with Ni anode, the charge transfer resistance for the cell with the Ni-S anode in CO increased dramatically whereas only limited increase was found in H_2. This illustrates that CO was not effectively activated on Ni-S catalyst whereas H_2 still was.
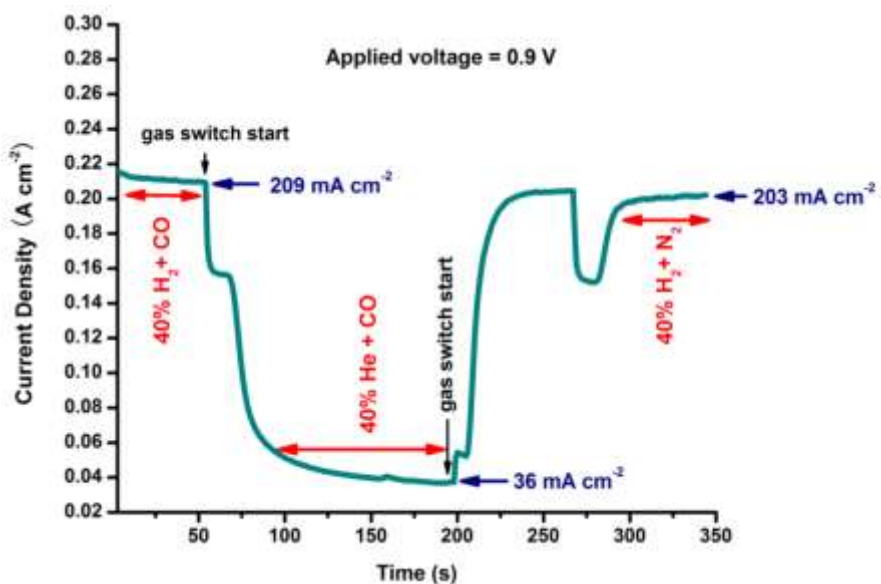
Figure 8-4 Current density vs. time for cell with Ni-S anode under potentialstatic condition at 0.9V at 850 $^{\circ}$C in different gas mixtures.

Although electrochemical test data in the previous paragraph provide an alternative way in HSO evaluation, gas composition analysis of anode effluent is a

131

more convincing and precise method in selectivity determination. The obtained selectivity and conversion data are shown in Fig. 8-5C. When H_2 concentration was 14.3 % in syngas, its selectivity could be up to 92 % with a reasonable conversion when the applied voltage was 0.8 V. As the applied potential dropped to below 0.6 V, on the other hand, the conversion of CO became electrochemically more favourable (Fig. 8-5c). From the first order derivative of CO_2 signal derived from mass spectroscopic data (Fig. 8-6), a steady increase in CO oxidation rate could be observed since the applied potential dropped to below 0.4 V. This trend can also be observed in the I-V curve of CO conversion, the slop of the curve became increasingly steep-less when the applied voltage decreased to below ~ 0.6 V (Fig. 8-3a). The oxygen spill-over mechanism was attributable in addressing the selectivity decrease, which will be discussed later [21] (Fig. 8-7).
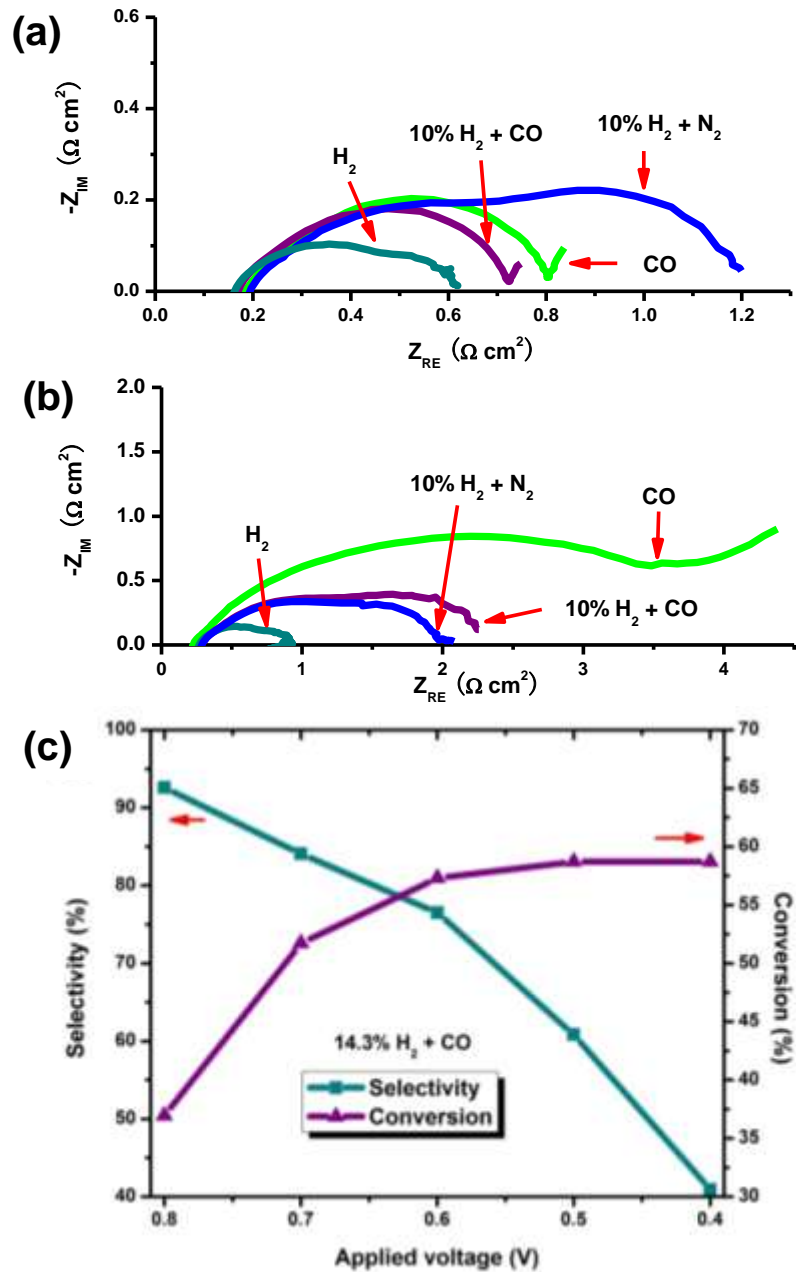
Figure 8-5 H$_2$ selectivity and SOFC electrochemical impedance spectra. Impedance spectra of fuel cells with (a) conventional Ni/YSZ and (b) Ni-S/YSZ anode catalyst fed by H$_2$, 10% H$_2$ + N$_2$, 10% H$_2$ + CO and CO. (c) Variation of selectivity and conversion as a function of SOFC applied voltage.

133
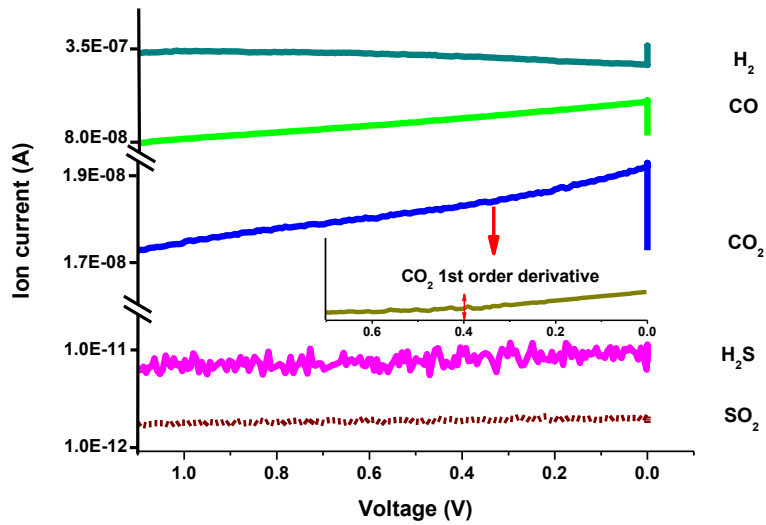
Figure 8-6 Variation of anode effluent composition with the applied potential. The mass spectroscopic data from the anode effluent is obtained during a potentiodynamic scan at 3 mV s^{-1} from OCV to 0 V at 850 $^{\circ}$C. The fuel is 60% H_2 + CO contained 120 ppm H_2S and its flow rate is 30mL min^{-1}.
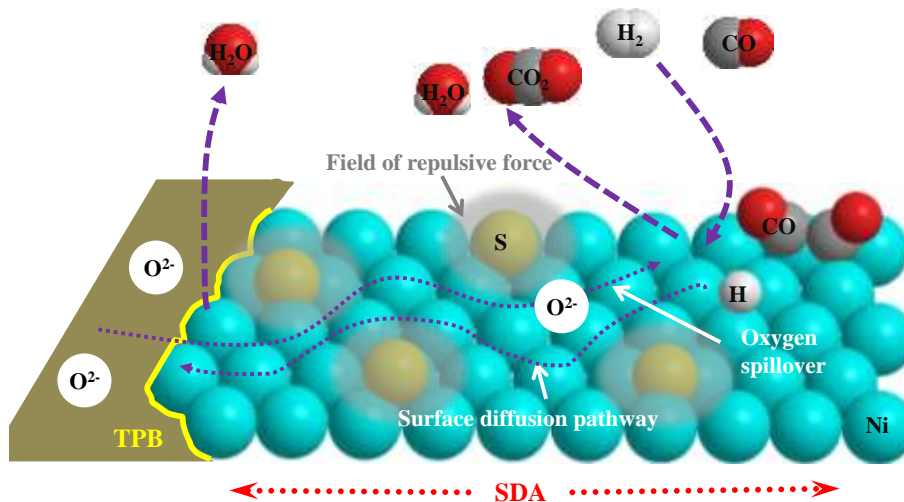
Figure 8-7 A Schematic of selective surface diffusion hypothesis and oxygen spill-over within SDA on Ni-S anode catalyst.

134
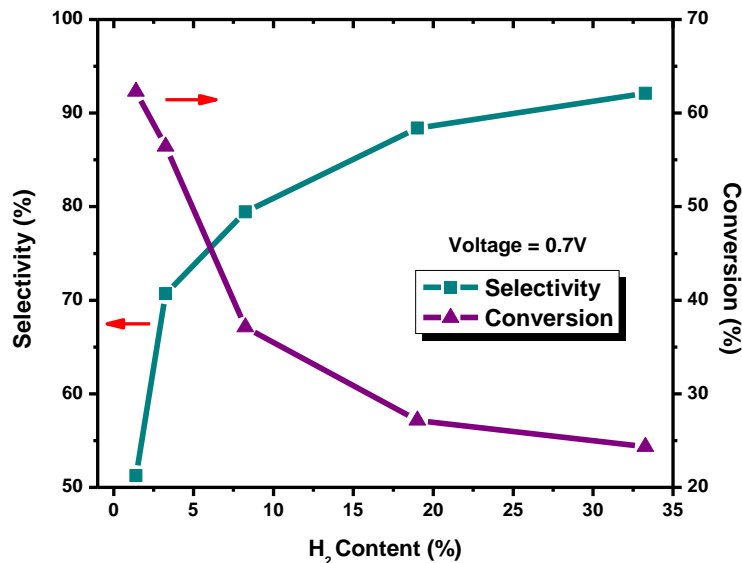
Figure 8-8 Selectivity and conversion of H_2 electrocatalytic selective oxidation as a function of fuel cell applied voltage between 0.8 V and 0.4 V.

When the cell was operated under potentiostatic mode at 0.7 V (Fig. 8-8), H_2 selectivity could exceed 80 % when its concentration was higher than 10 %. However, it dropped almost exponentially to around 50 % when the concentration was reduced to 1.4 % as a consequence of H_2 depletion. This value was still more than 20 times higher than that in a conventional Ni based SOFC and could rise up to around 60 % when the applied potential was increased to 0.9 V. Due to the intrinsic limitations of the experimental setup of button SOFC test, it was extremely difficult to achieve high fuel utilization. One possible way to increase H_2 conversion is to lower the applied potential which will lead to drastic H_2 selectivity decrease. Therefore, the anode effluent cyclic treatment was employed

in which the stream of SOFC anode effluent was recycled back to fuel cell repeatedly in order to achieve higher H_2 conversion and selectivity simultaneously (Fig. 8-9a). After 8 cycles of electrochemical reaction, in syngas that originally contained 40 % of H_2, more than 87 % selectivity and up to 97 % conversion of H_2 was achieved (Fig. 8-9b).
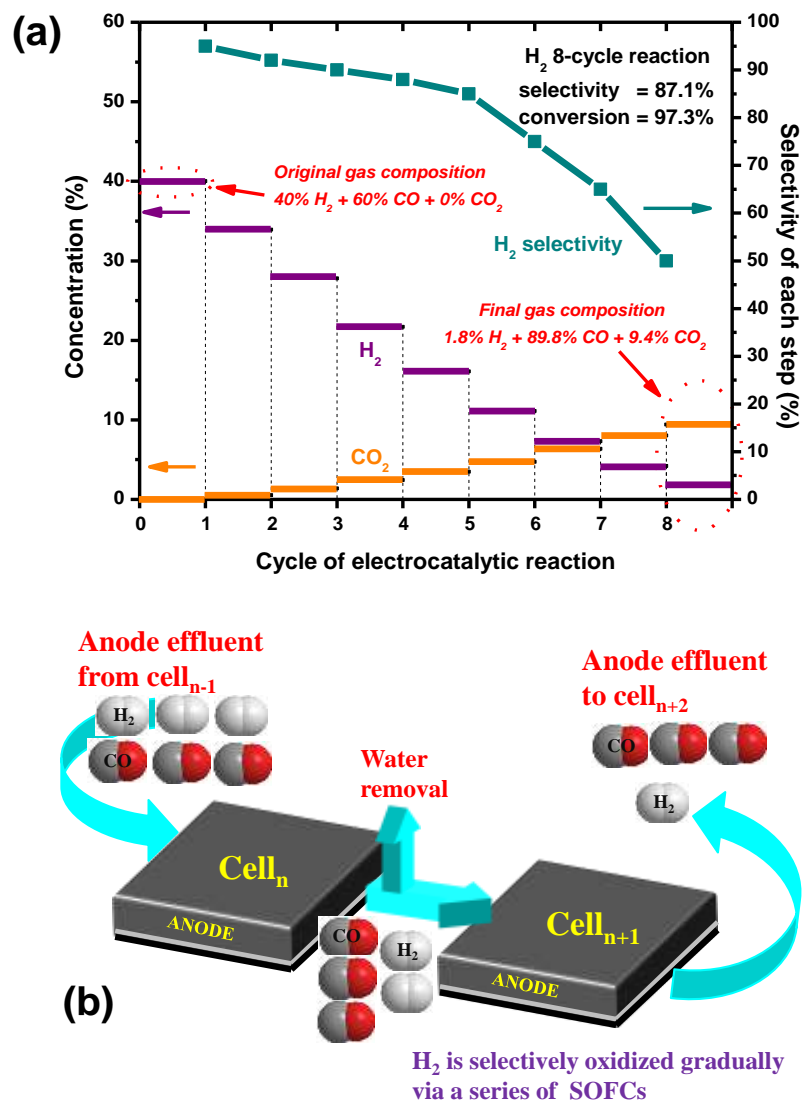
Figure 8-9 (a) Accumulative H_2 selectivity and conversion after each cycle of anode effluent to SOFC. (b) A Schematic of anode effluent cyclic treatment.

8.3.4 Mechanisms of electrocatalytic selective oxidation

In general, both chemical and electrochemical effects should be taken into account for the interpretation of HSO on Ni-S catalyst. From the perspective of chemical catalysis, the chemisorption structure of adsorbate can affect reaction rate significantly. According to infrared spectra [22], CO_{ad} on fresh Ni surface has three distinct structures named as bridged (CO_{ad-B}), linear (CO_{ad-L}) and subcarbonyl (CO_{ad-S}), respectively. With the co-adsorption of S, formation of CO_{ad-B} was completely inhibited whereas the bond between CO_{ad-L} and Ni atom was weakened, leading to the adsorption of extra CO molecules on the same Ni atom and generation of more CO_{ad-S} (Fig. 8-10). Considering there was no structure change for H_2 dissociative chemisorption on Ni-S, it is rational to conclude that the significant CO oxidation rate decrease on Ni-S could be ascribed to the elimination of CO_{ad-B} which was documented to be more active toward electrochemical oxidation [23]. The slow oxidation rate of existing weakened CO_{ad-L} or CO_{ad-S} facilitated H_2 selective oxidation in syngas.
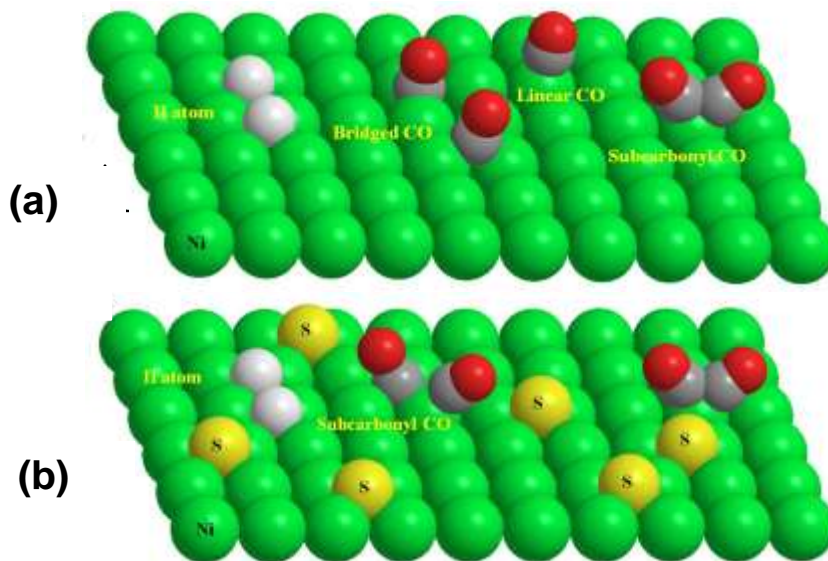
Figure 8-10 Schematics of H_2 and CO chemisorption structure on Ni. Balls in white, grey, red, green and yellow are H, C, O, Ni and S, respectively. (a), CO molecule adsorbs on fresh Ni in linear, bridged and subcarbonyl structure whereas H_2 molecule adsorbs on it dissociatively. (b), CO molecule adsorbs on Ni-S only in subcarbonyl structure whereas H_2 molecule still adsorbs on it dissociatively.

From the electrocatalytic point of view, adsorbate surface diffusivity is the controlling factor of fuel conversion rate [24]. Therefore, the localized surface diffusion area (SDA) adjacent to TPB extending to Ni with width of several hundreds of Angstrom plays an important role in HSO [25]. S_{ad} was reported to have a significant influence on the surface diffusion of H_2 and CO on Ni surface resulted from its strong electronic effect and geometric blocking effects [12, 26]. Since CO_{ad} has a much larger proportion relative to H_{ad} and is a polar molecule, its surface diffusion was likely to be more greatly suppressed by S_{ad}. This

hypothesis was also supported by the drastically increased Warburg impedance of CO spectra at the low frequency end on Ni-S catalyst in Fig. 8-5b. Hence, only H_{ad} can preferentially diffuse to TPB and be oxidized by oxygen ions whereas most of CO_{ad} can not. This hypothesis can be entitled as selective surface diffusion and the schematic of the process is illustrated in Fig. 8-7.

When SOFC was operating at low applied voltage, oxygen would be spilled out from the electrolyte instantly and moved to the SDA. As a result, both of CO_{ad} and H_{ad} could be readily oxidized without the necessities of diffusing to TPB, the selective surface diffusion hypothesis would not be valid under this circumstance and the high H_2 selectivity would be undermined accordingly as observed in Fig. 8-5C and 8-6.

8.3.5 Reactor stability

To examine Ni-S anode catalyst stability, the button cell was operated under potentiostatic mode at 0.7 V for 200 h, followed by up to 100 h of conversion/selectivity and other electrochemical determinations. There was no observable degradation during 300 h longevity test (Fig. 8-11). At the end, H_2 selectivity and conversion were analyzed using 14.3 % H_2 syngas at 0.7 V and compared with the data in Fig. 8-8B. Selectivity decreased from 86 % to 72 %, but recovered to more than 80 % when the cell was maintained at OCV and re-treated with H_2S for 15 min. The selectivity decrease is attributable to the large

amount of water vapour generated which caused the partial removal of chemisorbed S atoms from Ni-S [14].
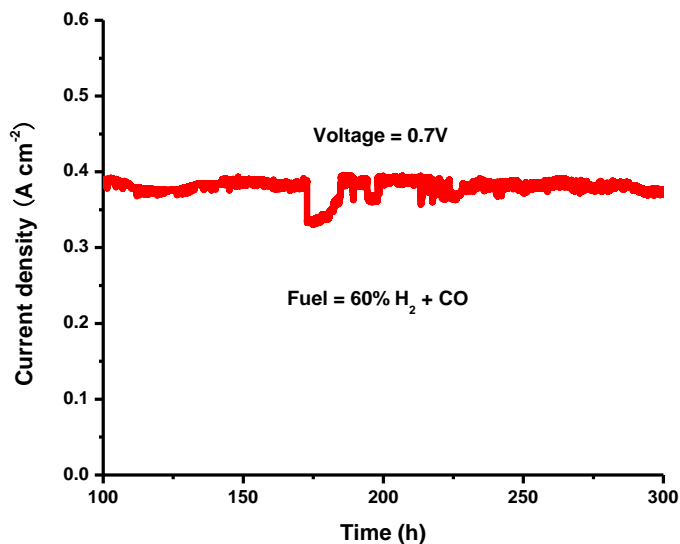
Figure 8-11 Stability test of Ni-S cell in syngas. The fuel cell is under potentiostatic mode as the applied potential is 0.7 V. The fuel is 60% H_2 + CO contained 120 ppm H_2S and its flow rate is 30mL min^{-1}.

8.3.6 Influences of side reactions

Due to the existance of various side reactions, anode feed composition at high tempearature might change accordingly and undermine the final conclusion. Thus, the software HSC Chemistry 5.0 was used to claculate the equilibrium gas composition. Table 8-1 shows the equilibrium composition of 10% H_2 + CO at different temperatures and it was observed that negligible compositional variation would occure. Among all side reactions, four of them are worth more attentions:

$$CO + 3H_2 \rightleftharpoons CH_4 + H_2O \qquad\qquad\qquad (8\text{-}3)$$

$$CO + H_2 \rightleftharpoons C + H_2O \qquad\qquad\qquad (8\text{-}4)$$

$$2CO \rightleftharpoons C + CO_2 \qquad\qquad\qquad (8\text{-}5)$$

$$CO + H_2O \rightleftharpoons CO_2 + H_2 \qquad\qquad\qquad (8\text{-}6)$$
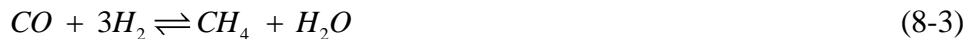
Reaction (8-3) is methanation process which is not thermodynamically favourable to occure under experimental condition (850 $^{\circ}$C), and no CH$_4$ was detected by GC in the anode effluent. Reactions (8-4) and (8-5) are the major sources of coke formation, they are strongly suppressed on Ni-S catalyst [27] and after longevity test, no carbon deposits were visible on the anode. Water gas shift reaction (WGS) in (8-6) is the most influencial side reaction on electrocatalytic H$_2$ selective oxidaiton in syngas: if the forward direction of WGS is thermodynamically favourable, then the actual H$_2$ selectivity should be higher than the measured one and the major conclusion of the present work will be strenghened; if the backward direction of WGS is thermodynamically favourable, then the H$_2$ preferencial conversion can be the result of this reaction. Suppose that the original gas feed is 10% H$_2$ + 90% CO. After electrochemical reaction under particular H$_2$ selectivity and conversion ocnditions as listed in table 8-2 and 8-3, a new gas composition, named as AER, was obtained. Through H$_2$ concentration comparison between AER and equilibrium composition of AER calculated using HSC Chemistry 5.0, it was found that H$_2$ concentration in the latter mixture was much higher than that in the former one. Therefore, it was confirmed that forward

WGS is thermodynamically favourable, and the actual H_2 selectivity is even higher than the reported ones of this work.

Table 8-1 Equilibrium syngas compositions at different temperatures. The original syngas composition was 10% H_2 + 90% CO.

Species	Original (%)	Equilibrium Composition (%)				
		700 ^{o}C	750 ^{o}C	800 ^{o}C	850 ^{o}C	900 ^{o}C
CO	90	86.1	89.8	89.9	90.0	90.0
H_2	10	5.95	7.76	8.74	9.28	9.58
CO_2	0	1.90	1.12	0.62	0.34	0.20
H_2O	0	0.09	0.08	0.06	0.04	0.03
CH_4	0	1.99	1.20	0.67	0.38	0.22

Table 8-2 Equilibrium gas compositions at different H_2 selectivities when H_2 conversion is fixed at 50 %. The original syngas feed composition was 10% H_2 + 90% CO. AER represents gas composition after electrochemical reaction under particular H_2 selectivity and conversion. The equilibrium gas composition of AER was shown in the column of equilibrium.

Species	Selectivity = 66.7%		Selectivity = 83.3%		Selectivity = 90.9%	
	AER	Equilibrium	AER	Equilibrium	AER	Equilibrium
CO	87.5	83.3	89	84.7	89.5	85.1
H_2	5	9.15	5	9.30	5	9.35
CO_2	2.5	6.7	1	5.37	0.5	4.92
H_2O	5	0.82	5	0.66	5	0.61
CH_4	0	0.02	0	0.02	0	0.02

Table 8-3 Equilibrium gas compositions at different H_2 conversions when H_2 selectivity is fixed at 83.3%. The original syngas feed composition was 10% H_2 + 90% CO. AER represents gas composition after electrochemical reaction under particular H_2 selectivity and conversion. The equilibrium gas composition of AER was shown in the column of equilibrium.

Species	Conversion = 10%		Conversion = 50%		Conversion = 90%	
	AER	Equilibrium	AER	Equilibrium	AER	Equilibrium
CO	89.8	88.7	89	84.7	88.16	80.3
H_2	9	9.63	5	9.30	1	9.67
CO_2	0.2	1.17	1	5.37	1.84	8.8
H_2O	1	0.12	5	0.66	9	1.18
CH_4	0	0.14	0	0.02	0	0.01

8.4 Conclusions

A novel electrocatalytic selective oxidation process using *in-situ* prepared Ni-S catalyst has been discovered in oxygen ion-conducting SOFC, which was applied in the H_2 selective oxidation in syngas with reasonable amounts of co-generated power. A proposed CO chemisorption structural change on Ni-S catalyst and the sequential selective surface diffusion mechanism were used to explain the observed phenomena. An engineering process entitled as anode effluent cyclic treatment was also developed. The discovery of the present work

confirmed that a high conversion and selectivity of H_2 in a single SOFC button cell reactor was technically feasible to be achieved.

References

[1] E. P. Murray, T. Tsai, S. A. Barnett, *Nature*, 1999, **400**, 649-651.

[2] X. Z. Fu, J. L. Luo, A. R. Sanger, N. Danilovic, K. T. Chuang, *Chem. Commun.*, 2010, **46**, 2052-2054.

[3] M. Ni, M. K. H. Leung, D. Y. C. Leung, *Int. J. Hydrogen Energy*, 2008, **33**, 2337-2354.

[4] Y. Jiang, A. V. Virkar, *J. Electrochem. Soc.*, 2003, **150**, A942-A951.

[5] J. G. E. Cohn, US Patent 3 216 783 (9 November 1965).

[6] S. Alayoglu, A. U. Nilekar, M. Mavrikakis, B. Eichhorn, *Nat. Mater.*, 2008, **7**, 333-338.

[7] A. S. K. Hashmi, G. J. Hutchings, *Angew. Chem. Int. Edit.*, 1999, **45**, 7896-7936.

[8] J. J. Baschuk, X. G. Li, *Int. J. Energy Res.*, 2011, **25**, 695-713.

[9] J. R. Stetter, K. F. Blurton, *Ind. Eng. Chem. Prod. R&D*, 1977, **16**, 22-25.

[10] S. B. Adler, *Chem. Rev.*, 2004, **104**, 4791-4843.

[11] C. H. Bartholomew, *Catal. Rev. Sci. Eng.*, 1982, **24**, 67-112.

[12] J. Oudar, *Cat. Rev.-Sci. Eng.*, 1980, **22**, 171-195.

[13] T. Rosenqvist, *J. Iron Steel Inst.*, 1954, **176**, 37-57.

[14] Z. Cheng, M. L. Liu, *Solid State Ionics*, 2007, **178**, 925-935.

[15] Z. Cheng, J. H. Wang, Y. M. Choi, L. Yang, M. C. Lin and M. L. Liu, *Energy Environ. Sci.*, 2011, **4**, 4380-4409.

[16] J. Benard, J. Oudar, N. Barbouth, E. Margot, Y. Berthier, *Surf. Sci.*, 1979, **88**, L35-L41.

[17] http://www.netl.doe.gov/publications/proceedings/05/SECA_PeerReview/pdf /Marina.PNNL%20Fri%20AM.pdf.

[18] Y. Jiang, A. V. Virkar, *J. Electrochem.Soc.*, 2003, **150**, A942-A951.

[19] Y. Matsuzaki, I. Yasuda, *J. Electrochem. Soc.*, 2000, **147**, 1630-1635.

[20] W. G. Wang, M. Mogensen, *Solid State Ionics*, 2005, **176**, 457-462.

[21] W. C. Conner, J. L. Falconer, *Chem. Rev.*, 1995, **95**, 759-788.

[22] C. H. Rochester, R. J. Terrell, *J. Chem. Soc. Faraday Trans. I*, 1977, **73**, 609-621.

[23] K. I. Tanaka, M. Shou, H. He, X. Y. Shi, *Catal. Lett.*, 2006, **110**, 185-190.

[24] R. E. Williford, L. A. Chick, G. D. Maupin, S. P. Simner, J. W. Stevenson, *J. Electrochem. Soc.*, 2003, **150**, A1067-A1072.

[25] R. E. Williford, L. A. Chick, *Surf. Sci.*, 2003, **547**, 421-437.

[26] X. D. Xiao, Y. L. Xie, C. Jakobsen, H. Galloway, M. Salmeron, Y. R. Shen, *Phy. Rev. Lett.*, 1995, **74**, 3860-3864.

[27] J.R. Rostrupnielsen, *J. Catal.*,1984, **85**, 31-43.

Chapter 9 Conclusions, Recommendations and

Future Work

9.1 Summary of Major Achievements

The major achievements of the work described in the previous chapters are summarized in Fig. 9-1.
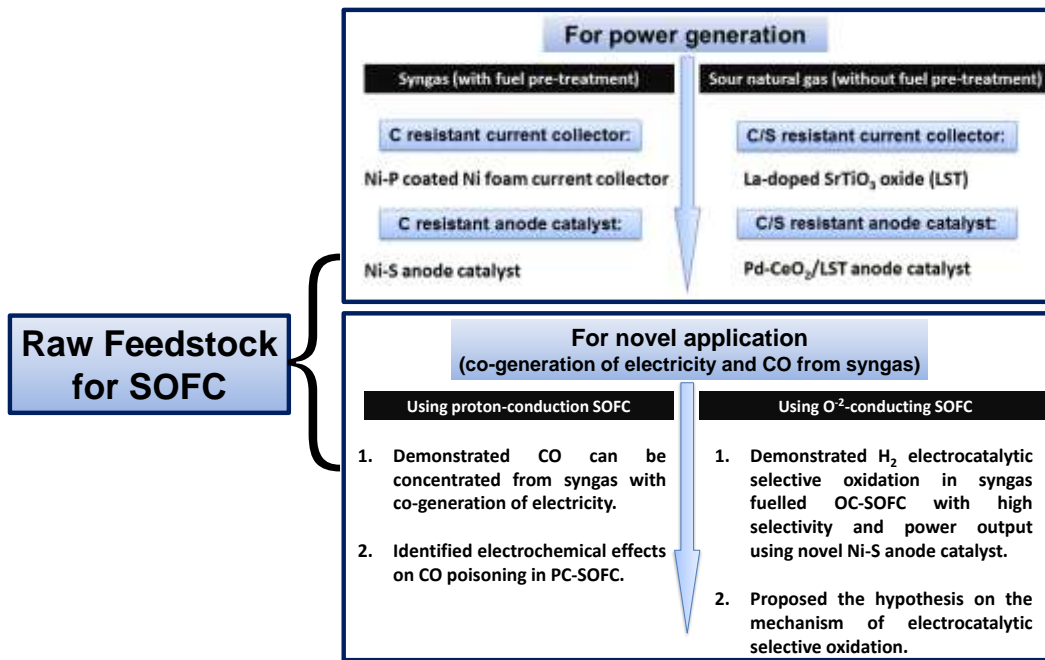

Figure 9-1 Summary of the major achievements in this thesis.

In the category of SOFC for power generation, both coke-resistant anode current collector and catalyst were developed to meet the requirements of SOFC with fuel pre-treatment (desulfurization and external steam reforming). For the

SOFC fed by the fuel without pre-treatment, the candidate materials resisting both coking and sulfur were examined. In the other category related to novel application of SOFC in the field of co-generation of electricity and CO from syngas, both PC-SOFC and OC-SOFC were used to investigate their effectiveness and efficiencies in coping with the proposed technical objectives.

9.2 Recommendation for Future Work

9.2.1 Coke and sulfur resistant current collector developments

The Ni-P coated Ni foam fabricated via electroless plating exhibited excellent coking resistance and electronic conductivity in syngas which is the most commonly used feedstock of SOFC and is obtained through hydrocarbon pre-treatment. After the coating of Ni-P and due to the precipitation of the ceramic phase Ni_3P after heat treatment, the toughness and ductility of the Ni foam decreased although the strength increased. To optimize the mechanical properties of the Ni-P coated Ni foam, it is recommended in the future work to study the effectiveness of Ni-P-M coating where M is the transition metal elements including Fe, Co and Cu. Since the coating composition of Ni-P after heat treatment was Ni + Ni_3P, it would be interesting to apply this material as the coking tolerant anode catalyst of SOFC.

The La-doped SrTiO$_3$ perovskite oxide (LST) described in the Chapter 4 showed outstanding stability in the sour fuel without pre-treatment (0.5%H$_2$S + CH$_4$) while maintaining satisfactory electronic conductivity, which made it a promising candidate as the anode current collector. It was reported in the literature that the reduction of LST at elevated temperature could generate extra oxygen vacancies which could increase the electronic conductivity. Hence, in the future, it is recommended to examine the performance of high temperature reduced LST as anode current collector. On the other hand, since the high oxygen ionic conductivity cannot promote the performance of current collector, various alternative A-site dopants of wider range can be selected to substitute Sr in SrTiO$_3$ for the purpose of electronic conductivity enhancement. At the meantime, the influence of A-site deficiency on the electronic properties of SrTiO$_3$ also needs to be measured.

9.2.2 Coke and sulfur resistant anode catalyst developments

The surface modified Ni anode (Ni-S) exhibited exceptional balance between high activity toward syngas electrochemical conversion and good coking resistance. The Ni-S catalyst in SOFC also demonstrated high selectivity towards H$_2$ preferential oxidation in syngas. Without the sophisticated high temperature *in-situ* apparatus used in H$_2$S environment, the surface characterization results of Ni-S catalyst determined at room temperature were relatively less accurate and

cannot dynamically track the properties change as the electrochemical reaction proceeded. The future work should involve *in-situ* techniques such as *in-situ* XPS and Raman spectroscopy to characterize Ni-S catalyst at operating temperature.

Pd-CeO$_2$/LST anode catalyst was developed for converting hydrocarbon fuels without pre-treatment in SOFC. The developed anode catalyst showed superior chemical stability and outstanding activity in 0.5% H$_2$S + CH$_4$. The infiltrated metallic Pd nanoparticles were able to sustain its high stability in sour natural gas, which was confirmed by both thermodynamic calculation and experimental characterizations. They provided the primary activity for fuel conversion. The function of CeO$_2$ phase in the catalyst was to improve the thermal stability of Pd particles via alleviating the agglomeration effect at high temperature while adding extra activity to the composite catalyst. The LST phase mainly served as an electronic conductor. It should be noted that the novel catalyst suffered performance degradation after prolonged operation at high temperature, which was ascribed to the low thermal stability of Pd particles. Thereby, it is recommended that the Pd-CeO$_2$ cluster should be synthesized into a core-shell structure with CeO$_2$ as the shell to inhibit the growth of Pd at high temperature. Another applicable way to tackle this issue is to increase the loading of Pd with a compromise of the catalyst cost effectiveness.

9.2.3 Novel application of coke and sulfur resistant SOFC

The developed high performance PC-SOFC was proved to be able to concentrate CO from syngas. However, a systematic study revealed that the existence of high concentration CO could deteriorate the Ni catalyst significantly and a 3-stage CO poisoning model was established. Thus, in the future work of co-generation of electricity and CO using PC-SOFC, it is recommended to develop alternative high performance anode catalysts which can tolerate CO-induced deactivation. Meanwhile, it is also advised to investigate the H_2S poisoning effect in Ni based SOFC from the perspective of electrochemical impact which was confirmed to be influential in CO poisoning in PC-SOFC.

In this study, an OC-SOFC reactor was also investigated to address the requirements for electricity and CO co-generation. The electrocatalytic selective oxidation of H_2 from syngas using SOFC was firstly proposed and then proved to be effective. The developed Ni-S catalyst demonstrated high selectivity toward H_2 oxidation in SOFC and a reasonable power output was obtained. In addition to the recommended future work mentioned in 8.1, another interesting study could be focused on the alternative application of H_2 electrocatalytic selective oxidation. One typical example can be the ethylene production via selective oxidation of ethane in OC-SOFC with co-generation of electricity. The readily formed H_2 through high temperature ethane dehydrogenation in the SOFC anode chamber can be preferentially oxidized, which moves the reaction equilibrium towards the

products forming direction. This enables a higher conversion of ethane compared to the conventional route. Meanwhile, power can be co-generated with the value-added products. Since the formation of Ni-S catalyst requires a complicated H_2S treatment, it is also recommended to search and employ new metallic or ceramic catalysts with comparable characteristics.